

https://dspace.org/

Chemical vapor growth of nitrogen doped carbon nanotube and graphene materials for application in organic photovoltaic devices.

Bepete, George

2014-03-05
http://hdl.handle.net10539/14028

Downloaded from a DSpace repository. https://dspace.org/

Chemical Vapor Growth of Nitrogen Doped Carbon Nanotube and Graphene Materials for Application in Organic Photovoltaic Devices

Thesis submitted to the Faculty of Science, University of the Witwatersrand, Johannesburg, in fulfillment of the requirements for the Degree of Doctor of Philosophy

By

George Bepete

Declaration

I declare that this thesis is my own, unaided work.
It is being submitted to the
Faculty of Science
of the
University of the Witwatersrand
in fulfillment of the requirements for the degree of
Doctor of Philosophy
(2013)



10 October 2013

Candidate
(George Bepete)

Date

Supervisors

Prof. Neil J. Coville

Dr Z. Chiguvare

Abstract

Application of carbon nanomaterials like fullerene, carbon nanotubes, and graphene in solar cells using solution processable methods presents a great potential to reduce the cost of producing electricity from solar energy. However, carbon nanotubes and graphene materials are predominantly metallic and this limits their function in organic photovoltaic devices (OPVs) where semiconducting behavior is required. Doping of carbon nanomaterials is a well known method for making them semiconducting. Doping of carbon nanomaterials with nitrogen and boron can tune their properties to suit the requirements for use in photovoltaic applications as n-type and p-type semiconducting materials, respectively. Indeed, the use of nitrogen doped and boron doped carbon nanotubes in organic solar cells together with fullerene acceptors can improve the current density of the OPV devices.

Nitrogen doping of carbon nanotubes can be achieved by using nitrogen-containing precursor materials during chemical vapor deposition. However the doping of carbon nanotubes with nitrogen does not automatically make them n-type materials; they remain metallic unless a large amount of quaternary type nitrogen is incorporated in the carbon nanotubes. In this work we have developed a method to control the type of nitrogen that is incorporated in CNTs by using an appropriate synthesis temperature and use of oxygen-containing carbon precursors during the chemical deposition of carbon nanotubes. Quaternary N was incorporated in a CVD process when high temperatures and a high concentration of O in the precursor materials were used. We also showed that the type and amount of N can be changed from pyrrolic and pyridinic-N-oxide to pyridinic N and quaternary N by annealing N doped carbon nanotubes at temperatures above 400°C. At temperatures above 800°C most of the nitrogen is converted to quaternary nitrogen.

N-CNT thin films were used in OPVs so as to modify the ITO electrode and transform it into a 3D electrode. The resulting effect was an improved short circuit current density in the devices containing an N-CNT thin film that was placed on top

of the ITO electrode. A reduction in efficiency losses in OPVs at increasing light intensity was observed in the N-CNT ITO modified electrode OPVs. This is a remarkable finding when considering that one of the main problems hindering commercialization of OPVs is the loss of efficiency at high light intensities. We related these effects to the efficient charge collection by the modified ITO electrode. Incorporation of N-CNTs in the bulk heterojunction layer of the OPV device resulted in poor performance when compared to an OPV device made without N-CNTs. This effect is caused by shorting of the OPVs. We used a method of incorporating N-CNTs whilst minimizing shorting and this showed potential for better performance.

A study on the attempted doping of graphene with B to make it a p-type material showed that in the presence of a nitrogen carrier gas, BN instead of B was incorporated in graphene. This remarkable finding enabled us to grow a p-type graphene with a possible a band gap opening. This was corroborated by XPS and Raman spectroscopy studies of the material. This BN doped graphene material showed potential as a possible replacement of PEDOT:PSS as a hole transport material in OPVs. The BN doped graphene material can match the performance of PEDOT:PSS when the level of BN doping in graphene is increased.

Dedication

This thesis is dedicated to my parents Martha and George Bepete, for dealing with me being worlds away!

To my mother, you gave me the confidence to believe I could achieve anything. This gift has been foundational to all that I am and all that I will ever accomplish.

To my father, in my early life, our conversations were full of mathematical problems and puzzles. I think this is the period when the creativity in me was born. Thank you for trying to understand what I really do in the Lab, Nanotechnology and Photovoltaics.

I pray that I will forever be grateful and worthy.

Acknowledgements

I would like to thank and acknowledge the following persons and institutions for their support and assistance.

- **South Africa**

Prof Neil J. Coville and Dr Zivayi Chiguvare. Thank you for all the time you listened to my ideas, the encouragement, help in interpreting results, for letting me pursue whatever I wanted to experiment on and willingly allowing me to work with other people from two different continents, Europe and North America.

CATOMMAT group. The group provided an atmosphere, to learn, grow, play, to help, get help and form new friends. Particularly, I am very grateful and would like to extend a big thank you to Messai Mamo, Zikhona N. Tetana, Manoko Maubane, Themba Tshabalala, Thobeka Kente, Tumelo Nathaniel Phaahlamohlaka, David Ofori Kumi, William Mbongiseni Dhlamini, Boitumelo Matsoso, Neo Phao, Laila Khan, Isaac Beas, Basil Chassoulas, Mahalieo Kao, Nosipho Moloto and Ahmed Shaikjee.

Microscopy and Microanalysis Unit

School of Physics

School of Chemistry and Molecular Sciences Institute

Funding from the **DST/NRF CoE-SM** is acknowledged

IBSA

- **USA**

IAMDN, Rutgers University. Dr Johanna Bernstein, Prof Eric Garfunkel and Prof Manish Chowalla for allowing me to join the **IGERT Nanotechnology for clean Energy**. I had a wonderful experience during my time at Rutgers and fellow workers in Prof Chhowala's labs were very helpful particularly, Damien Voiry, Rajesh Kappera, Jaesung Kim, Hisato Yamaguchi, Maryam Salehi and Diego Alves.

- **Germany**

IFW Dresden Institute for Solid State Research. Dr Mark Ruemmeli and Susi Lindner for helping with ideas and XPS measurements.

Publications

Related to PhD study

1. **Bepete G**, Tetana ZN, Lindner S, Rummeli M, Chiguvare Z and Coville NJ. The use of aliphatic alcohol chain length to control the nitrogen type and content in nitrogen doped carbon nanotubes. *CARBON* 2013; 52(2): 316 –325.

2. Tetana ZN, Mhlanga SD, **Bepete G**, Krause RWM and Coville NJ. The Synthesis of Nitrogen-Doped Multiwalled Carbon Nanotubes Using an Fe-Co/$CaCO_3$ Catalyst. *S. Afr. J. Chem.* 2012; 65: 39–49.

3. **Bepete G**, Voiry D, Chhowalla M, Chiguvare Z and Coville NJ. Incorporation of small BN domains in graphene during CVD using methane, boric acid and nitrogen gas. **Nanoscale** 2013, 5, 6552 – 6557.

4. Ravat V, Nonqwe I, **Bepete G**, Meijboom R and Coville NJ. Pd on boron doped hollow carbon spheres - PdO particle size and support effects. *Journal of Catalysis* 2013; 305: 36 – 45.

5. de Freitas JN, Maubane MS, **Bepete G**, van Otterlo WA, Coville NJ and Nogueira AF. Synthesis and characterization of single wall carbon nanotube-grafted poly (3-hexylthiophene) and their nanocomposites with gold nanoparticles. **Synthetic Metals** 2013; *176:* 55-64.

6. **Bepete G**, Chiguvare Z and Coville NJ. Structural evolution of N forms in nitrogen doped carbon nanotubes on annealing. **Manuscript to be submited.**

7. **Bepete G**, Chiguvare Z and Coville NJ. Enhanced current collection using an N-CNT modified ITO electrode in a P3HT:PCBM solar cell. **Manuscript to be submitted.**

8. **Bepete G**, Chiguvare Z and Coville NJ. LPCVD growth of multilayer graphene on copper using low methane flow rates: Growth from below. **Manuscript to be submited.**

Awards

- **2010 - Best Postgraduate Student Presentation,** University of the Witwatersrand, School of Chemistry, Sponsored by WITS Chemical Society.
- **2011 - Best Presentation, Annual Student Presentations** sponsored by the DST/NRF Center of Excellence in Strong Materials.

- **2011 - Research Fellowship**, Institute of Advanced Materials Devices & Nanotechnology **IAMDN** at Rutgers University, USA (2011-2012). IGERT Nanotechnology for Clean Energy, Program.
- **2013 - Best Poster Presentation, Annual Student Presentations** sponsored by the DST/NRF Center of Excellence in Strong Materials.
- **2013 – Was selected by African Materials Research Society (AMRS) to represent Young African Scientists at the World Materials Summit, Strasbourg France.**

Presentations at conferences

- South African Institute of Physics (SAIP) Annual Conference - Pretoria 2010

Tuning carbon nanotubes for organic photovoltaics. (Oral)

- South African Chemical Institute (SACI) Conference – Johannesburg 2011

CVD growth of Nitrogen doped carbon nanotubes using O containing precursors. (Poster)

- South Africa Nanotechnology Initiative (SANI) – Bloemfontein 2012

A simple method to synthesize continuous large area boron nitride doped graphene. (oral)

- India Brazil South Africa (IBSA) Solar Conference – Johannesburg 2012

Graphene Patchwork on inverted organic photovoltaic devices (Oral)

- NanoSpain2013 – Bilbao, Spain 2013

The use of aliphatic alcohol chain length to control the nitrogen type and content in nitrogen doped carbon nanotubes. (Poster)

- Graphene2013 – Bilbao Spain 2013

Incorporation of small BN domains in graphene during CVD using methane, boric acid and nitrogen gas. (Poster)

Table of Contents

Declaration		ii
Abstract		iii
Dedication		v
Acknowledgements		vi
Publications		vii
Awards		viii
Presentations at conferences		viii
Table of Contents		ix
List of figures		xii
List of tables		xvi
Abbreviations		xvii
Chapter 1		1
Synopsis		1
1.1	Aim and objectives	1
1.2	Thesis Outline	2
1.3	Main Ideas	4
Chapter 2		5
Introduction		5
2.1	Background	5
2.2	Solar energy	5
2.2.1	Solar photovoltaics	6
2.2.2	Silicon based solar photovoltaics	6
2.3	Organic photovoltaics	7
2.3.1	Historical development	7
2.3.2	Operating principles of OPVs	8
2.4	The P3HT:PCBM bulk heterojunction solar cell	10
2.4.1	Improving performance of the P3HT:PCBM bulk-heterojunction OPV	11
2.5	Degradation of organic solar cells	12
2.5.1	Improving stability of organic solar cells	13
2.6	Material Challenges	13
2.6.1	Carbon nanotubes	13
2.6.2	Graphene	14
2.7	Doped carbon nanomaterials	14
2.7.1	Nitrogen doped carbon nanotubes	14
2.7.2	Large area BN doped graphene	16
References		17

Chapter 3 22
The use of aliphatic alcohol chain length to control the nitrogen type and content in nitrogen doped carbon nanotubes 22
3.1. Introduction 22
3.2. Experimental 26
3.3. Results and discussion 27
3.3.1. Variation of CVD temperature 27
3.1.1. Variation of precursor C:N:O ratio. 38
3.4. Conclusion 43
References 44

Chapter 4 46
Structural evolution of nitrogen bonding in nitrogen doped carbon nanotubes on annealing 46
4.1 Introduction 46
4.2 Experimental 48
4.3 Results and discussion 48
4.4 Conclusion 57
References 58

Chapter 5 62
LPCVD growth of multilayer graphene on copper using low methane flow rates: Growth from below 62
5.1 Introduction 62
5.2 Experimental 64
5.2.1 Synthesis and transfer 64
5.2.2 Characterization 65
5.3 Results and discussion 65
5.3.1 High flow rate and short exposure time 66
5.3.2 Medium flow rate and medium exposure time 66
5.3.3 Low flow rate and long exposure times 67
5.4 Conclusion 70
References 70

Chapter 6 73
Incorporation of small BN domains in graphene during CVD using methane, boric acid and nitrogen gas 73
6.1 Introduction 73
6.2 Experimental Section 74
6.2.1 Materials 74
6.2.2 Characterization 76
6.3 Results and discussion 76
6.4 Conclusions 84
References 84

Chapter 7 89
Enhanced current collection using an N-CNT modified ITO electrode in a P3HT:PCBM solar cell 89
7.1 Introduction 89
7.2 Experimental 90
7.2.1 Film Preparation 90
7.2.2 Device fabrication 91
7.3 Results and discussion 92
References 98

Chapter 8 100
N-CNT incorporation in bulk heterojunction P3HT:PCBM Organic Photovoltaics - placement effects 100
8.1 Introduction 100
8.2 Experimental 102
8.3 Results and discussion 103
8.4 Conclusion 106
References 106

Chapter 9 108
BN doped graphene as a hole transport layer in P3HT:PCBM bulk-heterojunction organic photovoltaic devices 108
9.1 Introduction 108
9.2 Experimental 109
9.2.1 Graphene synthesis 109
9.2.2 Device fabrication 110
9.3 Results and discussion 110
9.4 Conclusion 115
References 115

Chapter 10 118
Conclusions and Recommendations 118
10.1 Conclusions 118
10.1.1 Synthesis of carbon nanomaterials 118
10.1.2 Organic photovoltaic devices 119
10.2 Recommendations 120
10.2.1 Nitrogen doped carbon nanotubes 120
10.2.2 N-CNT modified electrode 120
10.2.3 BN doped graphene 120

List of figures

Figure 2.1 Schematic diagram of an OPV device comprising of a P3HT:PCBM bulk heterojunction between an Al cathode and PEDOT:PSS modified ITO anode on a glass substrate. **7**

Figure 2.2 schematic diagrams showing the part of (a) a heterojunction bilayer and (b) a bulk heterojunction of an organic photovoltaic device. **8**

Figure 2.3(a) Schematic diagram of an OPV device; (b) electronic energy levels of P3HT and PCBM; (c) typical J - V curve of the OPV device indicating the meaning of Jsc, Voc, FF, and PCE. Figure reproduced from reference [14] **9**

Figure 2.4 schematic diagrams showing an idealized interpenetrating nanostructured electrode for use in organic solar cell. The interpenetrating nanostructured electrode allows use of thicker films whilst area for charge collection is maximized **11**

Figure 2.5 Cross sectional view of an organic solar cell showing several processes that contribute to the degradation of the solar cell with time. Figure reproduced from reference [34] **12**

Figure 3.1 Type of nitrogen species (and corresponding N1s XPS binding energies) that can be incorporated in nitrogen-containing carbon materials. Figure reproduced from reference [14]. **23**

Figure 3.2 N and O composition in precursor mixtures made from 20 % acetonitrile in 80 % of methanol, ethanol, butanol, pentanol, heptanol, and octanol. **25**

Figure 3.3 TEM images of N-CNTs produced from a 20% acetonitrile in ethanol solution at different CVD temperatures: (a) 700 ^{o}C, (b) 850 ^{o}C, (c) 900 ^{o}C and (d) 1000 ^{o}C. **27**

Figure 3.4 Total yield of N-CNTs (as a percentage of catalyst material used) as a function of CVD temperature. **28**

Figure 3.5 Thermogravimetric analysis (TGA) of N-CNTs produced at different CVD temperatures. Insert TGA of the unpurified and purified N-CNT produced at 700 ^{o}C. **29**

Figure 3.6 Thermo gravimetric analysis (DTA) derivative curves for the impure N-CNTs produced at different CVD temperatures. **31**

Figure 3.7 XPS N1s spectra of N-CNTs produced at different CVD temperatures: (a) 700 ^{o}C, (b) 800 ^{o}C, (c) 850 ^{o}C, (d) 900 ^{o}C, (e) 1000 ^{o}C, and (f) nitrogen content in N-CNTs as a function of CVD temperature. **34**

Figure 3.8 Raman spectra of N-CNTs produced from an ethanol/acetonitrile precursor mixture at different CVD temperatures. **35**

Figure 3.9 Raman spectral intensity ratios of the different N-CNT samples produced at different CVD temperatures. **36**

Figure 3.10 TEM images of N-CNTs produced from 20% acetonitrile in (a) methanol and (b) octanol in CVD at 850 ^{o}C. **37**

Figure 3.11 The total yield of N-CNT (as a percentage of catalyst material used) as a function of carbon source (alcohol) used in the precursor Mixture. **38**

Figure 3.12 The N composition in N-CNTs made from the different alcohol precursor mixtures obtained from XPS analysis. **39**

Figure 3.13 XPS N1s spectra of N-CNTs produced in CVD at 850 ^{o}C showing different types of nitrogen incorporated in N-CNTS when (a) methanol, (b) ethanol, (c) butanol, (d) pentanol, (e) heptanol, and (f) octanol were used in the precursor. **40**

Figure 3.14 Raman spectra of N-CNTs produced from methanol/acetonitrile at different CVD temperatures. **42**

Figure 4.1 TEM image of N-CNTs produced from a 20% acetonitrile in ethanol solution at 700°C, (b) SEM image of N-CNT film made by the vacuum filtration method, and (c) AFM image of N-CNT film made by vacuum filtration and transferred onto a silicon substrate. **49**

Figure 4.2 XPS N1s spectra of N-CNT films annealed under vacuum and a H_2 gas flow at: (a) 100°C, (b) 200°C, (c) 400°C, (d) 600°C, (e) 800°C. **52**

Figure 4.3 XPS N1s spectra of N-CNT films annealed at 100°C, 200°C and 600°C. **53**

Figure 4.4 Typical condensation reactions involving (a) pyrrolic N forming pyridinic N, (b) pyrrolic N forming quaternary N and (c) pyridinic N forming quaternary N when annealing N-CNTs at temperatures above 400°C under inert conditions. **54**

Figure 4.5 Raman spectra of N-CNTs produced from methanol/acetonitrile at different CVD temperatures. **56**

Figure 4.6 Raman spectral intensity ratios of the different N-CNT films annealed at different temperatures under an N_2/H_2 gas flow. **57**

Figure 5.1 Optical micrographs of graphene grown under different flow-time systems showing different colors suggesting different layers of the produced graphene. **65**

Figure 5.2 Raman spectra of graphene films grown under the high flow rates and short growth times measured with a 514.5 nm excitation. **66**

Figure 5.3 Raman spectra of graphene films grown under the medium flow rate and medium growth times measured with a 514.5 nm excitation. **67**

Figure 5.4 Raman spectra of graphene films grown under the low flow rates and long growth times measured with a 514.5 nm excitation. **68**

Figure 5.5 Raman spectra of graphene films grown under different regimes of flow rates and growth times measured with a 514.5 nm excitation. **69**

Figure 6.1 Cylindrical quartz tube reactor showing the inserted copper envelope containing boric acid (boron source) placed 4 cm before the flat copper foil catalyst used for graphene growth. **75**

Figure 6.2 Graphene and BN doped graphene films grown on Cu using boric acid and nitrogen gas. (a) Optical images of pristine graphene transferred onto SiO_2/Si substrate. (b) Optical image of BN doped graphene transferred onto a SiO2/Si substrate. (c) Low-magnification TEM image of BN doped graphene on a plain Cu TEM grid showing a continuous graphene film. (d) High-magnification TEM image of BN doped graphene on a plain Cu grid showing small particles of Cu and Fe remaining after the etching process. (e) AFM image of BN doped graphene showing wrinkled graphene, and (f) AFM section analysis of BN graphene showing an average film thickness of 1.25 nm. **77**

Figure 6.3 Raman spectra of pristine graphene and BN doped graphene synthesized using the CVD method on copper. **78**

Figure 6.4 XPS spectra showing the (a) N1s, (b) B1s, and (c) C1s core levels obtained from BN doped graphene. **81**

Figure 6.5 C1s core level spectra of pristine graphene and BN doped graphene. **82**

Figure 6.6 Atomic model of the possible BN species incorporated in BN doped graphene (a) BN with N bonded to 2 carbon atoms, (b) h-BN with the N bonded to one or two carbon atoms and (c) h-BN domains in graphene matrix. **83**

Figure 7.1 The schematics of the OPV device containing an interpenetrating nanostructured electrode made with an N-CNT layer on an ITO electrode. **92**

Figure 7.2 Transparent N-CNT films; (a) transparent film on a PET substrate and SEM images made from filtering (b) 5 mL, 10 mL and 15 mL of dispersion. **93**

Figure 7.3 Transmittance at 550 nm of different films made from filtering different volumes of dispersion on the mixed ester cellulose membrane. **94**

Figure 7.4 Comparison of the J–V curves for OPVs with ITO only, 5mL N-CNT on ITO, 10 mL N-CNT on ITO and 15 mL N-CNT on ITO illuminated under a 100 mW/cm^2 light. **95**

Figure 7.5 Comparisons between PV performances for the four different devices (a) Voc (b) Jsc, (c) FF, and (d) PCE. **96**

Figure 8.1 OPV showing different layers in which CNT layers could be incorporated. **101**

Figure 8.2 Current density - voltage characteristics of photovoltaic devices with different hole transport layer. **103**

Figure 8.3 Schematic diagram of the bulk heterojunction active layer of the OPV device containing N-CNTs arrows signifying increasing concentration. **105**

Figure 9.1 (a) Current density - voltage characteristics of photovoltaic devices with different hole transport layer (b) Energy level diagrams of the bottom electrode ITO, interlayer material (BN doped graphene), P3HT (donor), and PCBM (acceptor), and the top electrode Al. **111**

Figure 9.2 (a) Schematic of the inverted photovoltaic device structure consisting of the following: ITO/ P3HT:PCBM/ BN doped graphene/ Al. (b) Energy level diagram of the bottom electrode ITO, PCBM (acceptor) and P3HT (donor), BN doped graphene (HTL) and the top electrode Al. **113**

Figure 9.3 (a) Current density - voltage characteristics of photovoltaic devices of the normal and inverted devices measured after fabrication at day 1, and (b)

Current voltage characteristics of photovoltaic devices of the normal and inverted devices measured after 14 days in air. **114**

List of tables

Table 3.1 Nitrogen content and type of the N-species contained in the N-CNTs grown at different CVD temperatures. **32**

Table 3.2 Nitrogen content and type of the N-species contained in the N-CNTs grown at 850°C using different alcohol precursors. **41**

Table 4.1 - Nitrogen Content and type of the N structures in the N-CNTs after annealing at different temperatures **55**

Table 6.1 Raman peak positions of pristine graphene and BN doped graphene synthesized with the CVD method on copper. **78**

Table 7.1 Summary of the device characteristics under 100 mW/cm^2 illumination for various PV devices fabricated in this work. **97**

Table 8.1 Summary of the photovoltaic parameters of different OPV devices incorporating N-CNT materials in different parts of the active layers. **104**

Table 9.1 Summary of Typical Photovoltaic Parameters of the different OPVs containing different HTL materials. **112**

Table 9.2 Summary of Typical Photovoltaic Parameters of the normal and inverted OPV containing a BN doped graphene HTL measured on different days. **115**

Abbreviations

The following is a list of abbreviations used in the text in alphabetical order:

Atmospheric pressure chemical vapor deposition – APCVD
Atomic force microscopy - AFM
Boron - B
Carbon - C
Carbon nanotubes - CNTs
Chemical vapor deposition - CVD
Differential thermogravimetric analysis – DTA
Donor-acceptor - D-A
Hexagonal boron nitride - *h*-BN
Hole transport layer - HTL
Hydrochloric acid – HCl
Incident photon-to-current efficiency - IPCE
Indium doped tin oxide - ITO
Full width at half maximum – FWHM
Graphene oxide - GO
Low pressure chemical vapor deposition - LPCVD
Multi-walled carbon nanotubes – MWCNTs
Nitrogen - N
Nitrogen doped carbon nanotubes - N-CNTs
Open circuit voltage - V_{OC}
Oxygen – O
6,6-phenyl-C61 butyric acid methyl ester - PCBM
Poly(3,4-ethylenedioxythiophene):polysytrenesulphonate - PEDOT:PSS
Poly (3-hexylthiophene) - P3HT
Poly(methyl methacrylate) – PMMA
Short circuit current density - J_{SC}
Sodium dodecyl sulphonate – SDS
Standard cubic centimeters per minute - SCCM
Thermo-gravimetric Analysis - TGA
Transmission electron microscopy - TEM
X-ray photoelectron spectroscopy - XPS

Chapter 1

Synopsis

1.1 Aim and objectives

The main factors that lead to poor performance of the P3HT:PCBM bulk heterojunction (BHJ) organic photovoltaic devices (OPVs) are: (1) low light harvesting because the thin films used allow most incident light to pass through, (2) the hopping type electron transport to electrodes is slow and results in a significant recombination process before collection and (3) poor stability of the devices. The aim of this work was to study and attempt to improve the performance of the P3HT:PCBM bulk heterojunction OPV by incorporating doped carbon nanomaterials in different parts of the device. In particular, the focus of the study was to investigate the following issues:

i. ***The use of N-CNT films deposited on the ITO electrode as a nanostructured interpenetrating electrodes to increase the thickness of the active layer in order to increase light absorption and thus increase exciton generation of the P3HT:PCBM BHJ device.***

ii. ***Incorporation of N-CNTs in the P3HT:PCBM bulk heterojunction active layer to selectively transport electrons to the metal electrode.***

iii. ***The use of BN doped graphene as a hole transport layer and encapsulating layer to reduce the rate of degradation of the active materials in an inverted solar cell.***

The drawback of using N-CNTs is that they are predominantly metallic making them both electron conductors and hole conductors thus making them centers for charge recombination before they reach the electrodes for collection. Doping of carbon nanotubes (CNTs) with large amounts of quaternary N is a well known method of

making CNTs n-type semiconductors. Control over the N type and content and morphology of N-CNTs during CVD still remains a major challenge. This is primarily due to the fact that different types of N are incorporated simultaneously during N-CNT synthesis. Changing the reaction environments and reaction conditions can influence the N type, but this also affects the morphology of the final product. As such it is necessary to gain a better understanding of the parameters that affect incorporation of different types of N in the N-CNTs during synthesis and after synthesis. In particular, a focus of the study was to consider the following issues:

i. ***Effect of reaction temperature during growth of N-CNTs using an ethanol/acetonitrile precursor mixture.***

ii. ***Effect of oxidizing environment during growth of N-CNTs.***

iii. ***Effect of heat treatment on the type of N and content in already formed N-CNTs.***

The use of graphene as a hole transport electrode is attractive because graphene is flexible, impermeable, transparent and conductive. Graphene oxide is a p-type material and is very suitable for this application but the problem is that it is difficult to deposit uniform continuous single layer graphene from GO on a substrate. As such, high quality single layer p-type graphene materials need to be synthesized. In this study the growth of high quality graphene and methods of doping graphene during CVD growth have been investigated. In particular the focus was on:

i. ***A study of the formation of single layer graphene on copper in a LPCVD method.***

ii. ***A study of the optimum condition to make single layer graphene and introduce both B and N to form BN doped graphene.***

1.2 Thesis Outline

This thesis has been written as a compilation of papers some of which have been published, are in press, are currently under review or are yet to be submitted.

Chapter 1 - Gives the aims and objectives of this study and the outline of the thesis.

Chapter 2 - Gives a justification for the study, highlighting the problems giving rise to poor performance of P3HT:PCBM bulk heterojunction solar cell and attempts to resolve these issues using carbon nanomaterials..

Chapter 3 – This chapter focuses on the use of temperature and oxygen in order to control the content type of nitrogen that can be incorporated in N-CNTs during growth. *This chapter was published as; Bepete G, Tetana ZN, Lindner S, Rummeli M, Chiguvare Z, Coville NJ. The use of aliphatic alcohol chain length to control the nitrogen type and content in nitrogen doped carbon nanotubes.* ***Carbon, 2013, 52, 316-325.***

Chapter 4 – This chapter focuses on the use of heat treatment on already grown N-CNTs in order to effect changes in the type of N in N-CNTs. *This chapter is to be submitted as; Bepete G, Voiry D, Chhowalla M, Chiguvare Z, Coville NJ. Structural Evolution of N structures in N-CNTs on annealing.*

Chapter 5 – In this work we investigated the effect of time and methane concentration on the formation of graphene layers on copper. We propose a mechanism which explains how multilayer graphene can form using low flow methane systems.

Chapter 6 – This chapter focuses on the doping of graphene with BN in order to induce the semiconducting behavior and hence band gap opening. *This chapter has been published as; Bepete G, Voiry D, Chhowalla M, Chiguvare Z, Coville NJ. Incorporation of small BN domains in graphene during CVD using methane, boric acid and nitrogen gas.* ***Nanoscale, 2013, 5, 6552 – 6557.***

Chapter 7 – This chapter focuses on the use of N-CNT thin films on ITO as a 3D electrode in a P3HT:PCBM bulk heterojunction solar cell. *To be submitted.*

Chapter 8 – This chapter focuses on the use of N-CNTs as a selective electron transport medium in the P3HT:PCBM bulk heterojunction active layer.

Chapter 9 – This chapter focuses on the use of BN doped graphene as a hole transport layer in the P3HT:PCBM bulk heterojunction solar cell.

Chapter 10 - This chapter provides a summary and conclusion of the current study highlighting advances made and challenges still faced.

1.3 Main Ideas

Below are some of the ideas developed during the length of this PhD research project.

i. ***We proposed that the synthesis temperature and oxygen presence during the growth of N-CNTs affect the amount and type of N incorporated in the N-CNTs.***

ii. ***Heat treatment of N-CNTs can be used to tune the type of nitrogen (N) in N-CNTs synthesized at low CVD temperatures,(from predominantly pyrollic N and pyridinic-N-oxide to pyridinic N and quaternary N).***

iii. ***Low concentration/flow rates of methane in low pressure chemical vapor deposition (LPCVD) of graphene on copper can yield multilayer graphene if long growth times are used. This occurs because at low concentration graphene coverage on the Cu surface is slow and more active carbon species can diffuse underneath the already formed graphene, resulting in nucleation and growth of new graphene domains underneath the already formed top domains.***

iv. ***Small BN domains can be incorporated in graphene during CVD using methane, nitrogen, hydrogen and boric acid on copper. The BN domains in graphene induce semiconducting behavior in the graphene.***

v. ***The use of a N-CNT film to modify the ITO electrode in an OPV results in an enhanced Jsc and also reduces efficiency losses that occur in OPVs with increasing light intensities.***

Chapter 2

Introduction

2.1 Background

The use of fossil fuels is increasingly becoming unsustainable, mainly because of their substantial contribution to greenhouse gases which cause global warming and also because the known reserves of fossil fuels are continuously diminishing. The world today uses 16.0 TW of power; of that amount, 87% is based on burning fossil fuels [1]. Due to the continued population increase and improvement in the quality of life in developing countries, the energy demand is growing by 1.69 %. This translates to a total world power requirement of 30 TW by 2050 [2]. Renewable energy resources like solar, wind, hydro and biomass offers a sustainable but expensive alternative to fossil fuels. Power generation using hydro, wind and biomass is particularly suitable for small scale stand alone power generation systems. The world's energy requirements are high and continue to rise on a daily basis. As such, any technology for renewable energy harvesting, conversion or storage in a sustainable future must be able to scale to the TW level to make a relevant impact at the global scale [3]. For this reason, solar energy conversion is viable because the resource is clean and infinite.

2.2 Solar energy

Solar energy has several environmental advantages over other energy sources which include that it is; free, infinite, does not emit CO_2 and other greenhouse gases and does not generate liquid or solid waste products. As such, it can be considered as the basis for a sustainable energy development program. The only limitation in exploiting the energy from the sun is in our ability to convert this abundant resource into affordable electricity. Energy from the sun can be converted into useful energy using solar thermal conversion, solar photovoltaics and solar fuels technologies. Solar

thermal conversion technology uses absorber materials to collect energy to heat water or to turn turbines to produce electricity [4,5]. Photo-catalysis can be used to split water to produce hydrogen fuel [6] or in the reduction of carbon dioxide into methanol [7], which can be burned as a fuel or as a precursor in organic synthesis to produce long chain hydrocarbons to be used as fuels. Solar photovoltaic cells use semiconducting materials that convert sunlight directly into electricity.

2.2.1 Solar photovoltaics

The photovoltaic conversion process has the potential to produce electricity at the GW-scale [8]. Adoption of this technology is only hindered by the cost related to the processing of the inorganic materials used in producing the solar cells and installation of the PV systems. The current cost of solar produced electricity is between $226 and $2031 compared to an average of $82 for coal fired electricity. The use of thin film materials in solar cells continues to be of interest as a potential source of renewable energy [9]. In particular, the use of thin films reduces material requirements thus reducing the cost of materials and the weight of the final PV systems. The cost of installation could be greatly reduced if flexible, paint based thin film photovoltaic solar cells can substitute the current more established bulk silicon based solar cells.

2.2.2 Silicon based solar photovoltaics

Despite intense research in the use of different new materials for photovoltaic conversion applications, over 90 % of photovoltaic (PV) modules produced worldwide are based on silicon material because of its durability, abundance and non-toxicity [10]. The lab based performance of for the silicon based solar cells stands at 25 % whilst the market product based efficiency stands between 15 – 22.4 % [11]. The major contributing factors to the cost of preparing a silicon based solar cell include, the required high purity silicon, high processing temperatures, large amounts of silicon required to produce the cells [12]. On the other hand, other solar photovoltaic technologies like organic photovoltaic cells, dye sensitized photovoltaic cells and quantum dot photovoltaic cells require less material to produces solar cells.

2.3 Organic photovoltaics

Organic photovoltaics (OPVs) are based on π-conjugated semiconducting organic molecules or polymers [13]. A combination of electron-donor and electron-acceptor materials with suitable HOMO and LUMO levels are used as the active material [14]. The best incident photon-to-current efficiency (IPCE) for organic solar cells has been improved rapidly over the years and it currently stands at around 8% using low band gap donor polymers with a [6,6]-phenyl-C61 butyric acid methyl ester (PCBM) acceptor material [15]. OPVs are commonly composed of an active layer comprising of a conjugated polymer such as poly(3-hexylthiophene) (P3HT) donor and a fullerene derivative PCBM acceptor sandwiched between a poly(3,4-ethylenedioxythiophene):polysytrenesulphonate (PEDOT:PSS) modified ITO positive electrode and a low work function metal negative electrode such as aluminium (Al), as shown in Figure 2.1. Commercialization of PCBM-P3HT OPVs is hindered by the elevated cost of PCBM-P3HT and the limited conversion IPCE. Yet they have a large application potential in power generation.

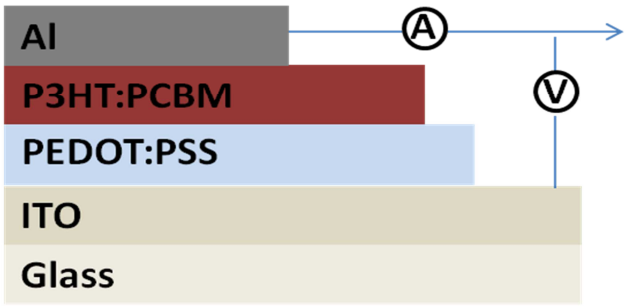

Figure 2.1 Schematic diagram of an OPV device comprising of a P3HT:PCBM bulk heterojunction between an Al cathode and PEDOT:PSS modified ITO anode on a glass substrate.

2.3.1 Historical development

Small organic molecules sandwiched between two metal electrodes of different work function were initially investigated for use in organic photovoltaics as an alternative to inorganic materials [16]. Small power conversion efficiencies of the order of 0.1 % were reported for these kinds of devices. The bilayer heterojucntion concept in which

a bilayer of n-type organic molecule and a p-type organic molecule were sandwiched between a transparent conducting metal oxide and a semitransparent metal managed to increase the power conversion efficiency to 1% [17]. The observation of a photoinduced electron transfer from optically excited conjugated polymers to C_{60} and improvement in photoconductivity upon addition of C_{60} to the conjugated polymers led to the development of the polymer-fullerene bilayer heterojunction and bulk heterojunction devices incorporating C_{60} and C_{60}-derivatives [13]. This has improved power conversion efficiency to around 8 % to date [18]. A better understanding of the fundamental processes of photovoltaic energy generation, in particular the complex relationship between donor-acceptor (D-A) and the reasons why recombination occurs in OPVs has been elucidated recently [19]. This has helped to create an understanding of the physical and chemical properties of the required materials needed to be incorporated in OPVs in order to enhance device performance.

2.3.2 Operating principles of OPVs

2.3.2.1 OPV device architecture

The bulk heterojucntion organic solar cell is the most favored because it is more efficient compared to the bilayer heterojunction solar cell. Figure (2.2a and b) shows the schematic representation of a heterojunction bilayer and a bulk heterojunction.

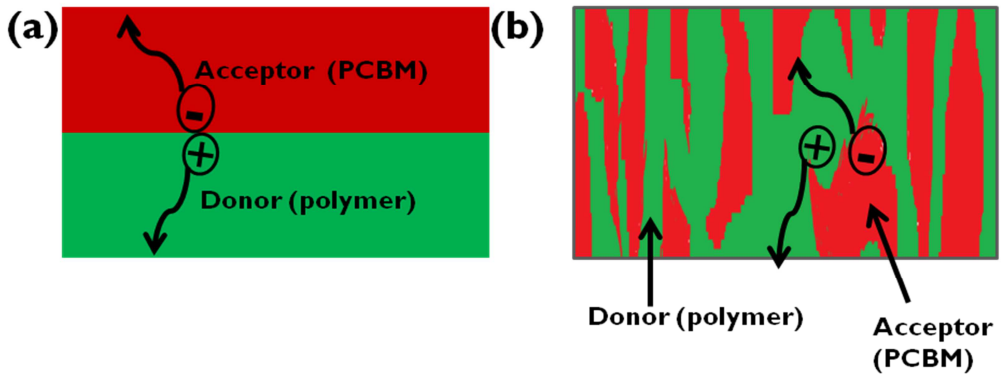

Figure 2.2 Schematic diagram showing the part of (a) a heterojunction bilayer and (b) a bulk heterojunction of an organic photovoltaic device.

OPVs are made on a supporting glass coated with a thin film of transparent and conducting oxide e.g indium doped tin oxide (ITO) which serves as an electrode. A hole transport layer e.g poly (3,4-ethylenedioxythiophene)-polystyrene sulfonate (PEDOT-PSS) is coated onto the ITO coated glass. The photoactive layer, a blend of the D-A material is coated on the PEDOT-PSS. Finally a second electrode usually aluminium metal is deposited by vacuum evaporation.

2.3.2.2 General mechanism of power generation

Figure (2.3a and b) displays a D-A bulk heterojunction OPV and the corresponding electronic energy levels of the D-A, exemplified by the poly(3-hexylthiophene) (P3HT) and [6,6]-phenyl-C61-butyric acid methyl ester (PCBM) bulk-heterojunction active layer. The light energy conversion process to electric current in organic photovoltaics follows five consecutive fundamental processes: (1) absorption of photons with wavelength in the absorption band of the donor (acceptor) to produce excitons (bound electron-hole pairs); (2) exciton diffusion within the donor (acceptor) phase towards an interface with acceptor (donor) before decaying; (3) dissociation of excitons (charge separation) producing charge carriers and electrons of the excitons transfer from the LUMO of the donor to the LUMO of the acceptor; (4) charge transport to electrodes through diffusion and or drift; (5) charge collection at electrodes. The thicknesses of each respective film in the organic solar cells are usually less than 200 nm. Figure 2.3c shows a typical current density (J)-voltage (V) curve of an organic solar cell device based on P3HT:PCBM under the

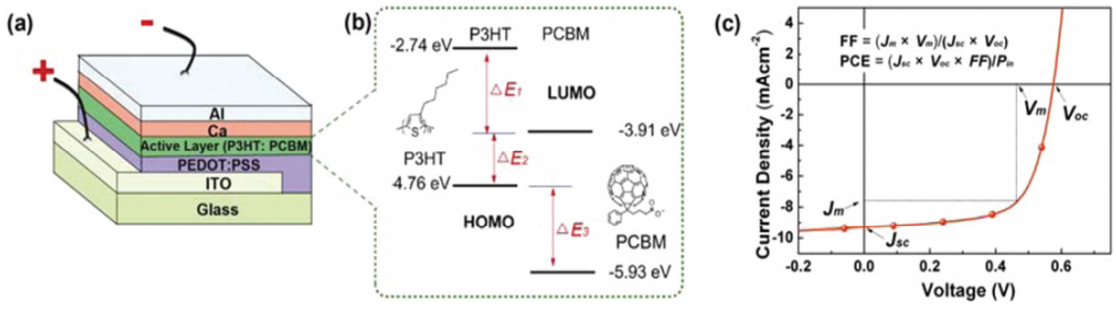

Figure 2.3(a) Schematic diagram of an OPV device; (b) electronic energy levels of P3HT and PCBM; (c) typical J - V curve of the OPV device indicating the meaning of Jsc, Voc, FF, and PCE . Figure reproduced from reference [14]

illumination of an AM1.5, 100 mW/cm^2 light. Figure 2.3c shows the short circuit current density (J_{sc}), open circuit voltage (V_{oc}), and fill factor (FF) of the devices. The FF is defined as $J_{max}V_{max}/J_{sc}V_{oc}$ and is shown in Figure 2.3c. The photovoltaic power conversion efficiency (PCE) of the organic solar cell is proportional to J_{sc}, V_{oc}, and FF. The J_{sc} depends on the efficiencies of the light absorption of the active layer, exciton diffusion to and dissociation at the D/A interface, charge transportation in the active layer, and charge collection on the electrodes. V_{oc} is mainly proportional to the energy level difference between the LUMO of the acceptor and the HOMO of the donor (ΔE2) as shown in Figure 2.3b) [20]. FF is related to the series and parallel resistances of the devices; lower series resistance and higher parallel resistance result in higher FF values.

2.4 The P3HT:PCBM bulk heterojunction solar cell

The P3HT:PCBM bulk-heterojunction solar cell is prepared by a blend solution of the donor (P3HT) and acceptor (PCBM) materials. The structures of both P3HT and PCBM are shown in Figure 2.3b. The high efficiencies in these devices are proposed to be due to a combination of favorable electronic properties of the pair (such as sub-picosecond charge transfer) and good miscibility [21]. The optimum blending ratio for the P3HT:PCBM bulk heterojunction device is ca. 50 % [22]. The use of a high polymer ratio of 50 % in the P3HT:PCBM compared to other systems like the (poly[2-methoxy-5-(3′,7′-dimethyloctyloxy)-1,4-phenylenevinylene]) (MDMO-PPV) PCBM blend where 80 % PCBM is required is an advantage because it offers more light absorption and better hole transport [23]. Thermal annealing at 110 ^oC of the P3HT:PCBM is an effective way of improving the performance of native P3HT:PCBM films [24]. Annealing induces P3HT crystallinity and phase segregation which improves transport properties of the P3HT and PCBM cluster formation respectively [25,26]. Larger PCBM clusters in the P3HT are beneficial for photovoltaic performance. The thickness of the active layer strongly affects the performance of the devices, with the optimum films having a thickness less than 100 nm [27].

2.4.1 Improving performance of the P3HT:PCBM bulk-heterojunction OPV

The performance of the P3HT:PCBM bulk-heterojunction solar cell can be improved by: (1) increasing the amount of excitons generated in the active layer per area and (2) improving the transport of electrons flowing to the metal electrode. Most of the light incident on the P3HT is not absorbed because optimum films are less than 100 nm thick [27]. The use of thicker films results in poor performance because recombination occurs before charges are collected at the electrodes [28]. In order to avoid recombination, but at the same time increasing the thickness of the P3HT:PCBM bulk-heterojunction active layer, interpenetrating nanostructured electrodes (as shown in Figure 2.4) are required in order to reduce the distance charges need to travel to electrodes for collection and to increase surface area for charge collection. Indeed, aligned ZnO nanowires [29,30] and nano-imprinted metals[31] have been used as nanostructured electrodes in dye sensitized solar cells and organic solar cells respectively.

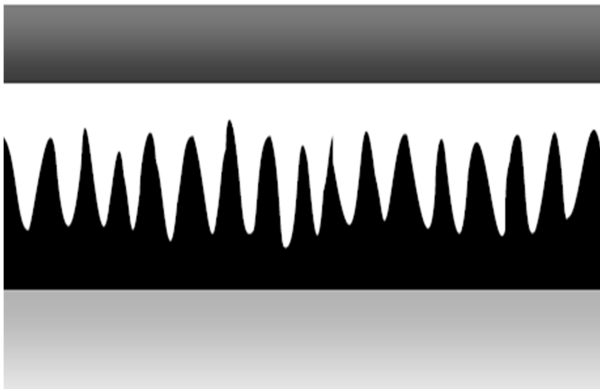

Figure 2.4 Schematic diagram showing an idealized interpenetrating nanostructured electrode for use in organic solar cell. The interpenetrating nanostructured electrode allows use of thicker films whilst area for charge collection is maximized

The transport of electrons in the P3HT:PCBM bulk-heterojunction active layer to the electrode can be increased by incorporating nanostructures which selectively transport electrons with high mobilities. Carbon nanotubes are ballistic conductors

[32]. This property could be useful if CNTs can be used as the acceptors and charge transport medium in organic solar cells to improve charge transport. Indeed, carbon nanotubes have been incorporated in the P3HT:PCBM bulk heterojunction active layer to enhance charge transport to electrodes [33].

2.5 Degradation of organic solar cells

There are several processes which contribute to the degradation of OPV performance (Figure 2.5) [34]. Organic materials are by nature more susceptible to chemical degradation by e.g. oxygen and water than are inorganic materials. The following process contribute in the degradation of OPVs: (1) Dissolution of the conducting ITO layer by chemical attack from the acidic PEDOT:PSS, (2) attack of the organic polymer by water which diffuses into the active layer from the water based PEDOT:PSS, (3) PCBM catalyzed atmospheric oxygen attack of the double bonds in the conjugated organic polymer in the active layer and (4) diffusion of the aluminium metal from the metal electrode into the P3HT:PCBM bulk-heterojunction active layer. Figure 3 shows several processes involved in the degradation of OPVs.

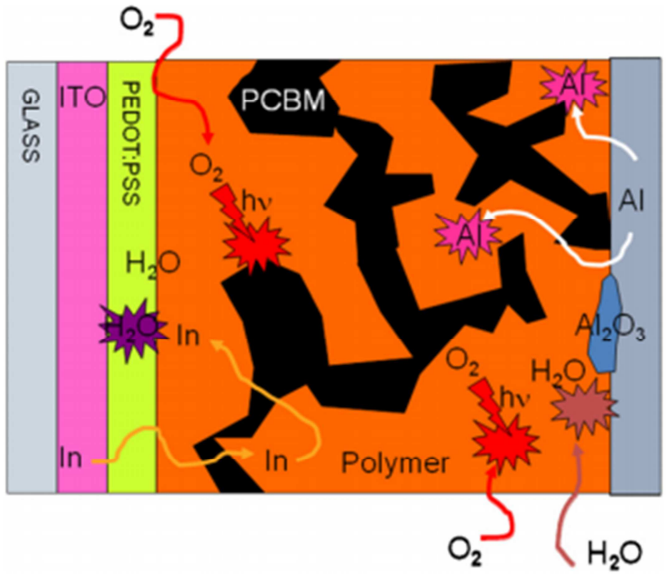

Figure 2.5 Cross sectional view of an organic solar cell showing several processes that contribute to the degradation of the solar cell with time. Figure reproduced from reference [34]

2.5.1 Improving stability of organic solar cells

Inverted organic solar cells in which electrons are collected on the ITO and holes on the aluminium metal can reduce the rate at which OPVs degrade [35,36]. This is because: (1) the ITO is isolated from the acidic PEDOT:PSS hole transport layer which corrodes the ITO and allows indium metal to diffuse through to the P3HT:PCBM bulk-heterojunction active layer, (2) the hole transport layer is now coated onto the P3HT:PCBM bulk heterojunction layer where it also acts as a barrier thus protecting the P3HT:PCBM layer by reducing the amount of water and oxygen reaching it. The hole transport layer coating reduces the amount of aluminium metal which diffuses into the P3HT:PCBM active layer. Indeed, inverted OPVs have shown better stability when compared to the normal OPVs [35,36]. Some of the hole transport layers used in inverted OPVs can also diffuse into the active layer as well allow water and oxygen to diffuse through because they are not completely impermeable to water and oxygen. A graphene based hole transport layer can be utilized to stop both the diffusion of the hole transport layer (HTL) material into the P3HT:PCBM bulk heterojunction active layer and act as a barrier to prevent water, oxygen and the metal electrode from diffusing into the P3HT:PCBM bulk heterojunction active layer [37,38].

2.6 Material Challenges

2.6.1 Carbon nanotubes

The drawback of using multiwalled carbon nanotubes in bulk-heterojunction solar cells is that they are predominantly metallic meaning they are both electron conductors and hole conductors. This makes them centers for charge recombination before the electrons and holes reach the electrodes for collection [39]. Doping of carbon nanotubes is a well known method for making CNTs semiconducting. Indeed, nitrogen doped and boron doped carbon nanotubes have been used in organic solar cells together with fullerene acceptors to improve the current density of the OPV device [40]. This means that they selectively transport electrons and holes to electrodes. The doping of nitrogen does not automatically make them n-type

materials, but a significant amount of one type of nitrogen, the quaternary nitrogen, needs to be incorporated in the carbon nanotube structure to achieve this result [41,42].

2.6.2 Graphene

The use of graphene as a hole transport electrode is attractive because it is flexible, impermeable, transparent and conductive. A problem is that graphene is metallic so it is not very suitable to collect holes. On the other hand graphene oxide is a p-type material and is very suitable for use as a hole collecting electrode. However, it is difficult to deposit a uniform continuous single layer graphene from a GO solution on a substrate. As such, high quality single layer p-type graphene material is still required for this purpose.

2.7 Doped carbon nanomaterials

2.7.1 Nitrogen doped carbon nanotubes

Robust methods to tune the unique electronic properties of carbon nanotubes by doping with N are in great demand due to the potential of these one dimensional materials to impact a range of applications. It is important to tune the CNT material for the development of high performance nitrogen doped carbon nanotube based systems. Our understanding of the factors influencing the amount and type of N incorporated in carbon nanotubes is still emerging. The type of N incorporated in the nitrogen doped carbon nanotube material (N-CNT) influences the electronic properties and also the effectiveness of the material as a catalytic support material or as catalyst. The doping of carbon nanotubes with boron and nitrogen was predicted in a calculation as early as 1993 [43]. The calculations showed that N will induce n-type behavior whilst B will induce p-type behavior in the doped carbon nanotubes. The possibility of doping CNTs to produce either n-type or p-type with N and B respectively revealed that the doped CNTs could have rich properties and opened a way for possible applications.

The first heteroatom doping in carbon nanotubes materials were reported with the simultaneous incorporation of B and N in a carbon nanotube material as early as 1994 [44] only three years after the initial report on carbon nanotubes by Iijima in 1991 [45]. This brought about an intense interest in the production of doped CNTs. The first report on nitrogen doping in carbon nanotubes was reported in 1997 [46]. The study was not aimed at producing N-CNTs, but aligned CNTs but because a solid N-containing carbon precursor material was used, N doping was achieved. Heteroatom doping became simplified after chemical vapor deposition growth of carbon nanotubes using gaseous and liquid hydrocarbons was reported in 1993 [47,48] and early 1994 [49]. This meant that a wide range of dopant containing precursor materials could be used thus simplifying the process of making doped CNT materials.

Studies on doping initially centered mostly on incorporating the highest amount of nitrogen into a CNT. Nitrogen forms incorporated in CNTs posses different chemistries and their presence depends on the growth conditions used during the synthesis of the CNT material [50] Recent research has shown that in addition to the concentration of N atoms in the graphitic carbon material, the boding character of N atoms plays a crucial role in determining their fundamental properties [51]. Nitrogen can be incorporated in the graphitic structure of carbonaceous materials in a variety of forms namely; pyridinic nitrogen, quaternary nitrogen, pyridinic-N-oxide and pyrrolic nitrogen.

2.7.1.1 N characterization techniques

Several techniques including, CHN analysis, XPS and EELS been used to quantify the amount and identify the type of nitrogen incorporated in carbon nanotubes. CHN analysis measures the amount of gaseous products after oxidation. This means that gaseous N forms physisorbed in the CNT walls are also included in the measurement. This method gives the concentration of N but without elaborating the type of N which is available in a sample. XPS and EELS give more information on the type of N observed in a sample. XPS is a powerful surface technique that can be used to accurately detect the presence and relative quantities of elements in a sample. Further

analysis can provide information about the state and environment of atoms in the sample, which can be used to infer information about the surface structure of the material. This is particularly useful for doped carbon nanomaterials, in which the dopant appears in different concentrations and different atomic environments.

Assigning each nitrogen type correctly in an N-CNT matrix to a respective binding energy still remains complex, but using the knowledge that, more positively charged atoms will require more energy to release an electron it is possible to arrange the atoms from which the electrons are originating from in an order of increasing binding energy. In terms of binding energy the nitrogen forms in an N-CNT structure can be arranged in the order of increasing binding energy: pyridinic-N < pyrrolic N < quaternary N < pyridinic N oxide. Various reports agree on assigning pyridinic N, pyrrolic N and quaternary N at binding energies of 398.5, 400.5 and 401.5 eV respectively [52].

Nitrogen can be incorporated in carbon nanotubes from as low as 0.1 % to as high as 20.0 % [53]. This is within the XPS detection limits of approximately 0.01% for monolayer and 0.1% for bulk materials.

2.7.2 Large area BN doped graphene

Several theoretical studies have shown that simultaneous incorporation of B and N in to graphene is thermodynamically possible yielding small planar hexagonal boron nitride (*h*-BN) domains in graphene and most importantly that this process achieves a band gap modulation in graphene [54]. The band gap opening in graphene, due to doping with small BN domains, has been attributed to the breaking of localized symmetry [55]. The tunable electronic properties of a graphene material containing BN makes this material likely to be useful in electronic devices, composites, energy conversion and storage. Indeed, a CVD method has recently been used to grow BN doped graphene on a copper foil using Ar/H_2, methane and ammonia borane gases [56]. This method produced graphene domains alloyed with discrete large BN domains.

References

1 BP, Statistical Review of World Energy, Bp plc technical report, 2011.

2 Armaroli N and Balzani V. The future of energy supply: challenges and opportunities. *Angew. Chemie Int. Ed.* 2007; *46*(1-2): 52-66.

3 Vesborg PCK, and Jaramillo TF. "Addressing the terawatt challenge: scalability in the supply of chemical elements for renewable energy."*RSC. Advances* 2012; 2(21): 7933-7947.

4 Meinel AB and Meinel MP. Physics looks at solar energy. *Phys. Today* 1972; 25: 44.

5 Cuomo JJ, Ziegler JF and Woodall JM. A new concept for solar energy thermal conversion. *Appl. Phys. Lett.* 1975; 26(10): 557-559.

6 Ni M, Leung MK, Leung DY and Sumathy K. A review and recent developments in photocatalytic water-splitting using TiO2 for hydrogen production. *Renew. & Sust. Energ. Rev.* 2007; 11(3): 401-425.

7 Inoue T, Fujishima A, Konishi S and Honda K. Photoelectrocatalytic reduction of carbon dioxide in aqueous suspensions of semiconductor powders. *Nature* 1979; 277: 637-638.

8 REN 21, Renewables 2010 Global Status Report, 19 (2010). See www.ren21.net.

9 Aberle AG. Thin-film solar cells. *Thin Solid Films* 2009; *517*(17): 4706-4710.

10 Green MA. The future of crystalline silicon solar cells. *Prog Photovoltaics* 2009; 8(1): 127-139.

11 Halim MA. Harnessing Sun's Energy with Quantum Dots Based Next Generation Solar Cell. *Nanomaterials* 2012, 3(1), 22-47.

12 Horiuchi N. and Wenham S. Towards highly efficient solar cells. *Nat. Photon.* 2012; 6: 136–137.

13 Yu G, Gao J, Hummelen JC, Wudl F and Heeger AJ. Polymer photovoltaic cells: enhanced efficiencies via a network of internal donor-acceptor heterojunctions. *S*cience 1995; *270*(5243): 1789-1790.

14 Li Y. Molecular design of photovoltaic materials for polymer solar cells: Toward suitable electronic energy levels and broad absorption. *Acc. Chem. Res.* 2012; 45(5): 723-733.

15 He Z, Zhong C, Huang X, Wong W, Wu H, Chen L, Su S. Cao Y. Simultaneous Enhancement of Open-Circuit Voltage, Short-Circuit Current Density, and Fill Factor in Polymer Solar Cells. *Adv. Mater* 2011; 23: 4636–4643.

16 Kallmann H and Pope M. Photovoltaic effect in organic crystals. *J. Chem. Phys.* 1959; 30(2): 585-586.

17 Tang CW. Two-layer organic photovoltaic cell. *App. Phys. Lett. 1986; 48:* 183.

18 Service R. Outlook brightens for plastic solar cells. Science 2011; 332: 293 -293.

19 Nicholson PG, and Castro FA. Organic photovoltaics: principles and techniques for nanometre scale characterization. *Nanotechnology* 2010; 21(49); 492001.

20 Scharber M, Muhlbacher D, Koppe M, Denk P, Waldauf C, Heeger AJ and Brabec C. Design Rules for Donors in Bulk-Heterojunction Solar Cells;Towards 10% Energy- Conversion Efficiency. *Adv. Mater.* 2006; 18: 789–794.

21 Günes S, Neugebauer H and Sariciftci NS. Conjugated polymer-based organic solar cells. *Chemical reviews* 2007; *107*(4): 1324-1338.

22 Ma W, Yang C, Gong X, Lee K and Heeger AJ. Thermally stable, efficient polymer solar cells with nanoscale control of the interpenetrating network morphology. *Adv. Func. Mater.* 2005; 15(10): 1617-1622.

23 Hoppe H and Sariciftci NS. Organic solar cells: An overview. *J. Mater. Res.* 2004; 19(07): 1924-1945.

24 Thompson BC and Fréchet JM. Polymer–fullerene composite solar cells. *Angew. Chemie Int. Ed.* 2008; 47(1): 58-77.

25 Fichou D 1995 *Handbook of Oligo-and Polythiophenes* (Weinheim: Wiley–VCH).

26 Campoy-Quiles M, Ferenczi T, Agostinelli T, Etchegoin PG, Kim Y, Anthopoulos TD, *et al.* Morphology evolution via self-organization and lateral and vertical diffusion in polymer: fullerene solar cell blends. *Nat. Mater.* 2008; 7(2): 158-164.

27 Li G, Shrotriya V, Yao Y and Yang Y. Investigation of annealing effects and film thickness dependence of polymer solar cells based on poly (3-hexylthiophene). *J. App. Phys.* 2005; 98(4): 043704-043704.

28 van Bavel S, Sourty E, de With G, Frolic K and Loos J. Relation between photoactive layer thickness, 3D morphology, and device performance in

P3HT/PCBM bulk-heterojunction solar cells. *Macromolecules* 2009; *42*(19): 7396-7403.

29 Galoppini E, Rochford J, Chen H, Saraf G, Lu Y, Hagfeldt A and Boschloo G. Fast electron transport in metal organic vapor deposition grown dye-sensitized ZnO nanorod solar cells. *J. Phys. Chem. B* 2006, 110(33), 16159-16161.

30 Gonzalez-Valls I and Lira-Cantu M. Vertically-aligned nanostructures of ZnO for excitonic solar cells: a review. *Energy Environ. Sci.* 2009; 2(1): 19-34.

31Hu L, Wu H and Cui Y. Metal nanogrids, nanowires, and nanofibers for transparent electrodes. *MRS Bull.* 2011; 36: 760-765.

32 Berger C, Yi Y, Wang ZL, and De Heer WA. Multiwalled carbon nanotubes are ballistic conductors at room temperature. *App. Phys. A* 2002; 74(3): 363-365.

33 Cataldo S, Salice P, Menna, E and Pignataro B. Carbon nanotubes and organic solar cells. *Energy & Environ Sci.* 2012; 5(3): 5919-5940.

34 Jørgensen M, Norrman K and Krebs FC. Stability/degradation of polymer solar cells. *Sol. Energ. Mat. Sol. C.* 2008; 92(7): 686-714.

35 Hau SK, Yip HL, Baek NS, Zou J, O'Malley K and Jen AKY. Air-stable inverted flexible polymer solar cells using zinc oxide nanoparticles as an electron selective layer. *App. Phys. Lett.* 2008; 92: 253301.

36 Zimmermann B, Würfel U and Niggemann M. Longterm stability of efficient inverted P3HT: PCBM solar cells. *Sol. Energ. Mat. Sol. C*. 2009; 93(4): 491-496.

37 Li SS, Tu KH, Lin CC, Chen CW and Chhowalla M. Solution-processable graphene oxide as an efficient hole transport layer in polymer solar cells. *ACS Nano* 2010; 4(6): 3169-3174.

38 Yusoff M, Kim HP and Jang J. Inverted organic solar cells with TiO_x cathode and graphene oxide anode buffer layers. *Sol. Energ. Mat. Sol. C.* 2013; 109: 63-69.

39 Ago H, Petritsch K, Shaffer MS, Windle AH and Friend RH. Composites of carbon nanotubes and conjugated polymers for photovoltaic devices. *Adv. Mater.*1999; 11(15): 1281-1285.

40 Lee JM, Park JS, Lee SH, Kim H, Yoo S and Kim SO. Selective Electron-or Hole-Transport Enhancement in Bulk-Heterojunction Organic Solar Cells with N-or B-Doped Carbon Nanotubes. *Adv. Mater.* 2011; 23(5): 629-633.

41 Krstic V, Rikken GL, Bernier P, Roth S, Glerup M. Nitrogen doping of metallic single-walled carbon nanotubes: n-type conduction and dipole scattering. Eur. Phys. Lett. 2007; 77(3):107–10.

42 Robertson J. and Davis CA. Nitrogen doping of tetrahedral amorphous carbon. *Diamond Relat. Mater*. 1995; 4(4):441.

43 Yi JY and Bernholc J. Atomic structure and doping of microtubules. *Phys. Rev. B* 1993; 47(3): 1708.

44 Lambert JM, Bernier P and Lefin P. Doping graphitic and carbon nanotube structures with boron and nitrogen. *Science* 1994; 266: 1683.

45 Iijima S. Helical microtubules of graphitic carbon. N*ature* 1991; 354(6348): 56-58.

46 Terrones M, Grobert N, Olivares J, Zhang JP, Terrones H, Kordatos K, et al. Controlled production of aligned-nanotube bundles. *Nature* 1997; 388(6637): 52-55.

47 Jose-Yacaman M, Miki-Yoshida M, Rendon L and Santiesteban JG. Catalytic growth of carbon microtubules with fullerene structure. *App. Phys. Lett.* 1993; 62(2): 202-204.

48 Endo M, Takeuchi K, Igarashi S, Kobori K, Shiraishi M and Kroto HW. The production and structure of pyrolytic carbon nanotubes (PCNTs). *J. Phys. Chem.* Solids 1993; 54(12): 1841-1848.

49 Ivanov V, Nagy JB, Lambin P, Lucas A, Zhang XB, Zhang XF and Van Landuyt J. The study of carbon nanotubules produced by catalytic method. *Chem. Phys. Lett.* 1994; 223(4): 329-335.

50 Bepete G, Tetana ZN, Lindner S, Rummeli MH, Chiguvare Z and Coville NJ. The use of aliphatic alcohol chain length to control the nitrogen type and content in nitrogen doped carbon nanotubes. *Carbon* 2013; 52: 316 –325.

51 Sharifi T, Hu G, Jia X and Wågberg T. Formation of Active Sites for Oxygen Reduction Reactions by Transformation of Nitrogen Functionalities in Nitrogen-Doped Carbon Nanotubes. *ACS nano 2012; 6*(10): 8904-8912.

52 Liu G, Li X, Lee JW and Popov BN. A review of the development of nitrogen-modified carbon-based catalysts for oxygen reduction at USC. Catal Sci Technol 2011;1(2):207–17.

53 Glerup M, Castignolles M, Holzinger M, Hug G, Loiseau A and Bernier P. Synthesis of highly nitrogen-doped multi-walled carbon nanotubes. Chem Comm 2003; 20: 2542–2543.

54 Shinde PP and Kumar V. Direct band gap opening in graphene by BN doping: Ab initio calculations. *Phys. Rev. B* 2012; 84(12): 125401.

55 Fan X, Shen Z, Liu AQ and Kuo JL. Band gap opening of graphene by doping small boron nitride domains. Nanoscale 2012; 4(6) 2157-2165.

56 Ci L, Song L, Jin C, Jariwala D, Wu D, Li Y, et al. Atomic layers of hybridized boron nitride and graphene domains. *Nat. Mater.* 2010; 9(5): 430-435.

Chapter 3

The use of aliphatic alcohol chain length to control the nitrogen type and content in nitrogen doped carbon nanotubes

3.1. Introduction

A range of precursor materials, catalysts and different procedures have been used to achieve varying levels of nitrogen doping in CNTs since Terrones *et al*. reported on the synthesis of nitrogen doped carbon nanotubes, N-CNTs, in 1997 [1]. The most common method to make N-CNTs involves the use of an organometallic catalyst dissolved in nitrogen-containing organic solvents that are injected into a CVD reactor [2]. The level of nitrogen doping and the type of nitrogen incorporated are all important in modulating the properties of N-CNTs [3]. Control of the nitrogen doping level in N-CNTs has been obtained by using different concentrations of diluted nitrogen-containing organic sources typically mixed with common carbon sources such as xylene [4], toluene [5-6], and benzene [7]. Gaseous precursors, like acetylene [8] have also been used in combination with N-containing reactants, to synthesize N-CNTs. Methods in which a carrier gas is bubbled through a nitrogen-containing source and then carried through to the CVD reactor can be used to modify the nitrogen content. The level of nitrogen doping is, in general, influenced by the flow rate of the carrier gas bubbled through the nitrogen-containing source relative to that of the carbon containing source which can be a gas or a liquid. Several nitrogen sources, like pyridine [9], acetonitrile [10], amines [11], and ammonia [12] have been used in CVD to grow N-CNTs using both injection and bubbling methods. Studies have shown that different nitrogen-containing sources affect the morphology,

structure, the type of nitrogen species incorporated and the nitrogen doping levels in the N-CNTs [13]. The nitrogen can exist in a variety of oxidation states in the N-CNT, the most important being the pyridinic type N and the quaternary N. Figure 3.1 shows the type of N species which can be incorporated in N-CNTs [14]. The pyridinic type N is bonded to two carbon atoms and has a localized electron lone pair. N-CNTs with a high pyridinic type N content exhibit catalytic activity in oxygen reduction reactions [15]. Quaternary N is the graphite like nitrogen incorporated into the extended graphene structure with one delocalized electron. The delocalized electron dopes the graphene layer thereby making the material n-type [16, 17]. Optimization of each type of N is important if the respective properties brought about by each type of N species are to be utilized in applications.

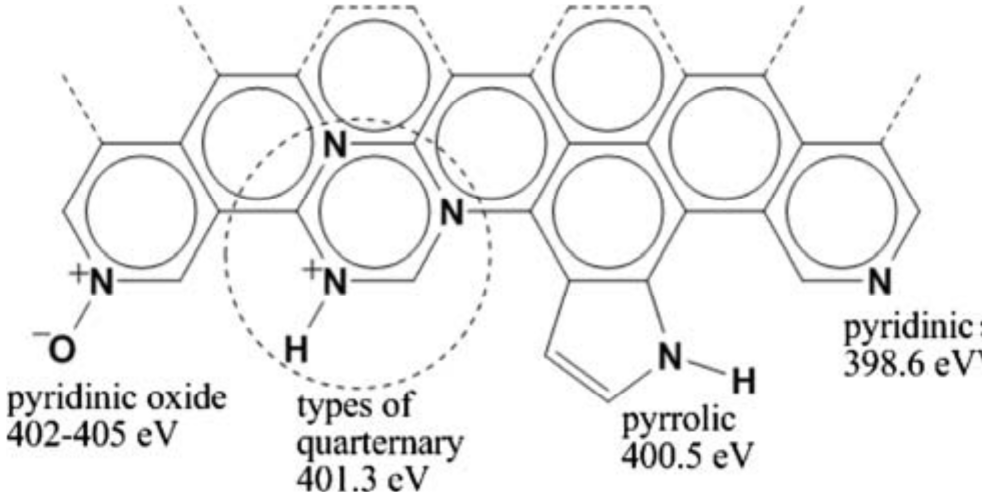

Figure 3.1 Type of nitrogen species (and corresponding N1s XPS binding energies) that can be incorporated in nitrogen-containing carbon materials. Figure reproduced from reference [14].

To date, however, studies that have been undertaken to control the type of nitrogen found in N-CNTs have focused on the effect of the synthesis temperature [18] and the nitrogen-containing carbon sources [19]. To the best of our knowledge no studies have been reported that indicate how the type of N content can be controlled by systematically varying the carbon source. One method to achieve this would be to use oxidizing agents. Thus the use of oxygen-containing reactants such as alcohols,

ketones, carboxylic acids *etc*. together with a nitrogen-containing source could be employed to achieve this objective. Indeed, two earlier studies have reported on the use of acetonitrile/ethanol mixtures to make N-CNTs. In one method, ferrocene was used as catalyst together with different mixtures of ethanol/acetonitrile solutions [13]. Nitrogen incorporation was found to generally increase with acetonitrile concentration but the type of nitrogen incorporated did not show any variation with the acetonitrile/ethanol ratio. In another study a Fe/MgO catalyst was used to make N-CNTs using varying concentrations of ethanol/acetonitrile [10]. The different precursor (ethanol/acetonitrile) mixtures yielded carbon nanotubes with very different morphologies and structures; from single walled and multi-walled, to bamboo-like structures and deformed carbon nanotubes all mixed together. In both studies different nitrogen species were incorporated into the CNTs. However, the type of nitrogen incorporated into the structures did not show any variation relative to the total nitrogen incorporated into the N-CNT material. Further, when the ethanol/acetonitrile ratio of reactants changed, the varying N/O ratios made it difficult to interpret the effect of oxygen content on the N content/type incorporated in the CNT. The effect of oxygen on N composition and bonding character in the N-CNT material was not studied in both studies. In a study related to this work, pure pyridine was used as a carbon and nitrogen source, and the N composition and bonding character in the N-CNT material showed a dependence on growth temperature [18].

The use of aliphatic alcohols of different chain length in the absence of a nitrogen containing reactant has been investigated in the synthesis of MWCNTs and it was shown that the chain length of the aliphatic alcohol influenced the crystallinity of the produced CNTs [20]. The addition of different types and amounts of alcohols to a carbon source showed that the quantity of O and C atoms in a precursor played an important role in modifying both the CNT growth and the CNT morphologies [21]. To determine if the type of nitrogen in an N-CNT could be influenced by oxygen atoms, we have synthesized a range of N-CNT materials using an ethanol/acetonitrile reactant mixture pyrolysed at different CVD synthesis temperatures.

Alcohol/acetonitrile mixtures with aliphatic alcohols with different chain length (ROH; R = CH_3, C_2H_5, C_4H_9, C_5H_{11}, C_7H_{15} and C_8H_{17}) were also studied; they all have similar structures/functional groups and also provide mixtures with controlled different C/O mass ratios whilst the nitrogen content as a function of total mass (C, O, and N) remains constant (Figure 3.2). The C/N ratio in the precursor mixture of each different alcohol increased with increase in alcohol chain length, for example from 7.1 for a methanol/acetonitrile mixture to 12.6 for an octanol/acetonitrile mixture.

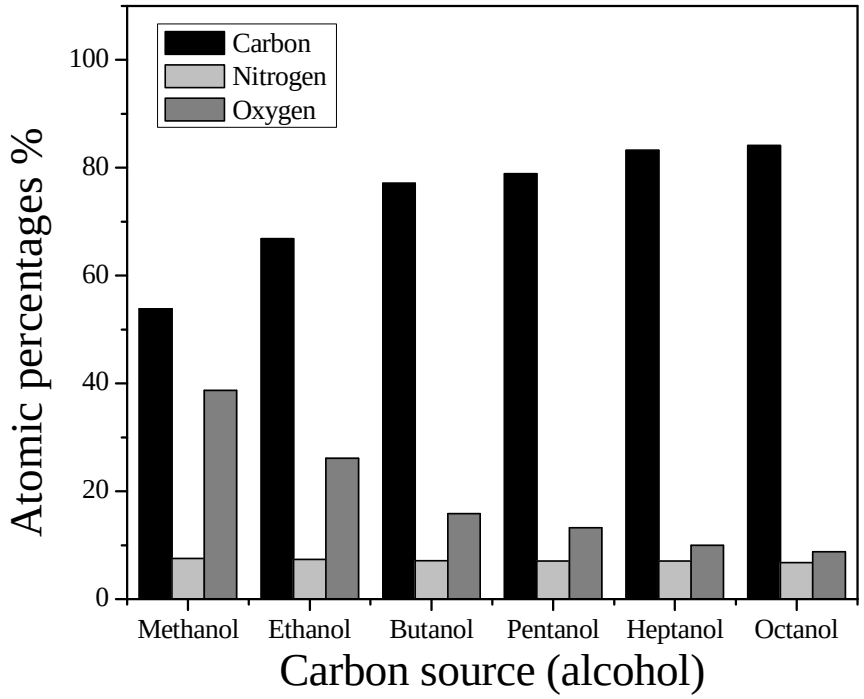

Figure 3.2 N and O composition in precursor mixtures made from 20 % acetonitrile in 80 % of methanol, ethanol, butanol, pentanol, heptanol, and octanol.

3.2. Experimental

N-CNTs were synthesized by the catalytic chemical vapor deposition (CCVD) method. The catalyst used in this study was Fe/Al/MgO [22], with a molar ratio of 1:1:12. A quartz boat containing 300 mg catalyst powder was inserted into the centre of a quartz tube reactor. The reactor was heated to the required temperature (T = 700

^{o}C, 800 ^{o}C, 850 ^{o}C, 900 ^{o}C, 1000 ^{o}C) in 5% H_2/Ar at flow rate of 240 mL/min. At the required temperature the carbon and nitrogen sources (80% ethanol and 20% acetonitrile by mass) mixtures were introduced into the reactor by means of a 20 ml syringe driven by a syringe pump at 1.2 mL/min for 20 minutes. Following the same procedure at 850 ^{o}C, different precursor mixtures containing 80% of an alcohol and 20% acetonitrile by mass were used. Aliphatic alcohols (methanol, ethanol, butanol, pentanol, heptanol and octanol) were used in this study (see Figure 3.2). After the reaction, the reactor was cooled to ambient temperature under a flow of 5% H_2 in argon. The yield of carbon nanotubes obtained was established by weighing the catalyst before N-CNT growth and weighing the catalyst and product after the N-CNT synthesis, using the formula:

$$\text{N-CNT yield (wt.\%)} = [(M_F - M_I)/M_I] \times 100$$

where M_F is the total weight of catalyst and product after synthesis, and M_I is the weight of the catalyst.

Purification (removal of catalyst) was achieved by sonicating the product in 6 M HCl at room temperature in an ultrasonic bath for 30 minutes. The sample was then filtered and washed thoroughly with distilled water and acetone. Finally the purified samples were dried in an oven at 120 ^{o}C for twelve hours. Morphological characterization of the N-CNTs was carried out using Transmission Electron Microscopy (Tecnai G^2 Spirit TEM at 120 kV). The thermal stability of the as synthesized N-CNTs and the extent of purification were determined by TGA using a Perkin Elmer Pyris Thermo-gravimetric Analyser 1 instrument under an air flow at 20 mL/min. The elemental composition of N-CNTs was determined by X-ray photoelectron spectroscopy (XPS) after purification using a PHI5600 spectrometer equipped with a monochromatic AlKα source (1486.6 eV). Raman spectra were recorded at ambient temperature on a Jobin-Yvon T6400 micro-Raman spectrometer using a tunable spectra Physics dye laser with a 636.4 nm excitation source.

3.3. Results and discussion

3.3.1. Variation of CVD temperature

The pyrolysis of ethanol/acetonitrile mixtures over a Fe/Al/MgO catalyst (T = 700 – 1000 ^{o}C) produced carbon nanotubes with a bamboo like morphology as noted from TEM images (Figure 3.3). The temperature and the ethanol precursor mixtures used

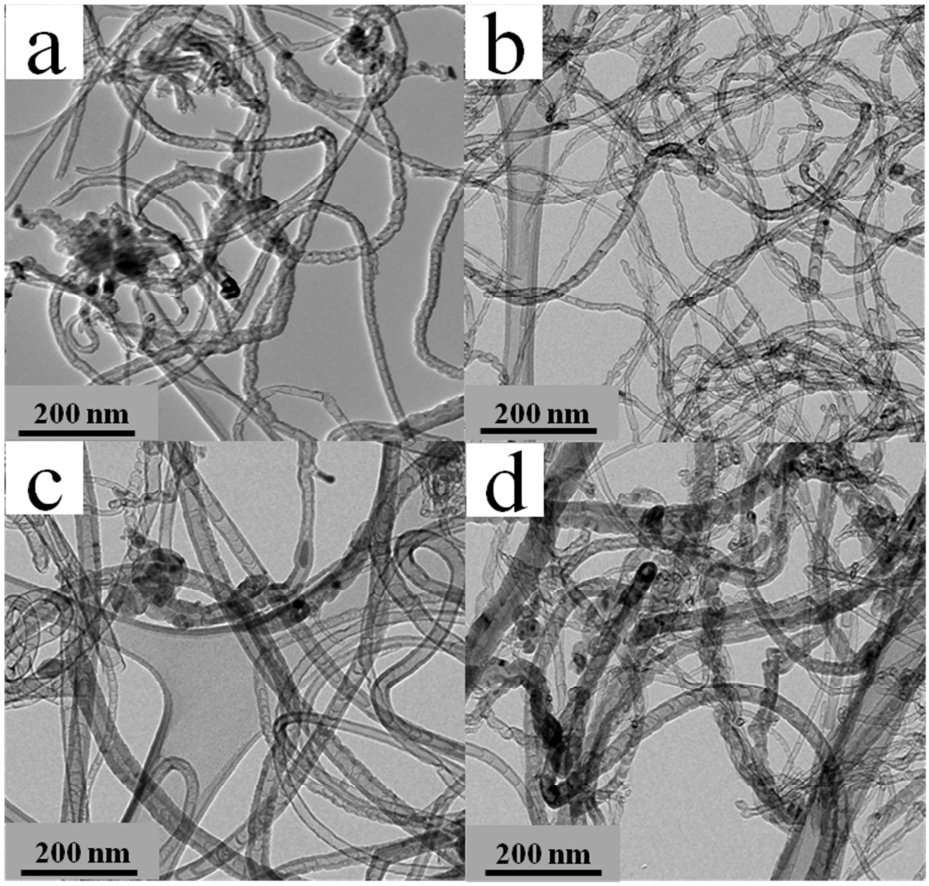

Figure 3.3 TEM images of N-CNTs produced from a 20% acetonitrile in ethanol solution at different CVD temperatures: (a) 700 ^{o}C, (b) 850 ^{o}C, (c) 900 ^{o}C and (d) 1000 ^{o}C.

played a significant role in generating the morphology of the produced N-CNTs. The N-CNTs formed at temperatures between 700 and 850 ^{o}C have a good tubular form with bamboo compartments with close spacing (Figure 3.3a and b). Above 850 ^{o}C the N-CNTs had larger diameters and the bamboo compartments were longer (Figure 3.3c). Most N-CNTs synthesized at 900 ^{o}C have a wide range of diameters (20 nm – 40 nm). At the higher temperatures metallic catalyst particles coalesce to form bigger

particles which in turn generated larger diameters of the synthesized carbon nanotubes (> 20 nm) [23]. At 1000 ^{o}C some irregularly shaped carbon material deposits were formed (Figure 3.3d).

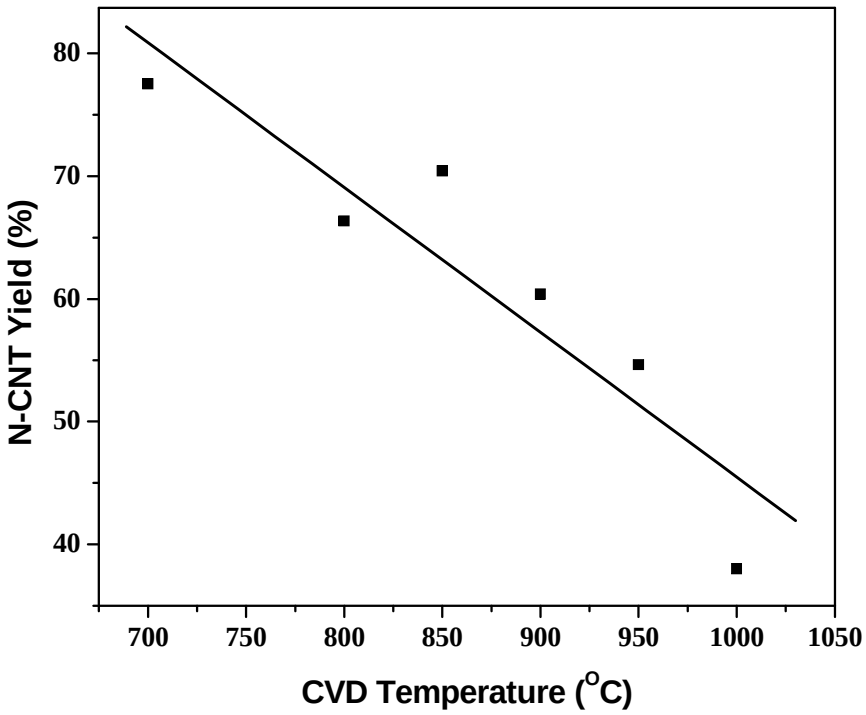

Figure 3.4 Total yield of N-CNTs (as a percentage of catalyst material used) as a function of CVD temperature.

The yield of N-CNTs decreased, almost linearly, as the temperature in the reactions increased (Figure 3.4). This trend is different from that reported previously where yields of N-CNTs and undoped MWNTs generally increase with increase in temperature [18]. The effect is due to the ethanol, an oxygen containing precursor which oxidises carbon at high temperatures. Also, at high temperatures the etching effect of the OH radicals will disrupt the initiation stage of N-CNT growth.

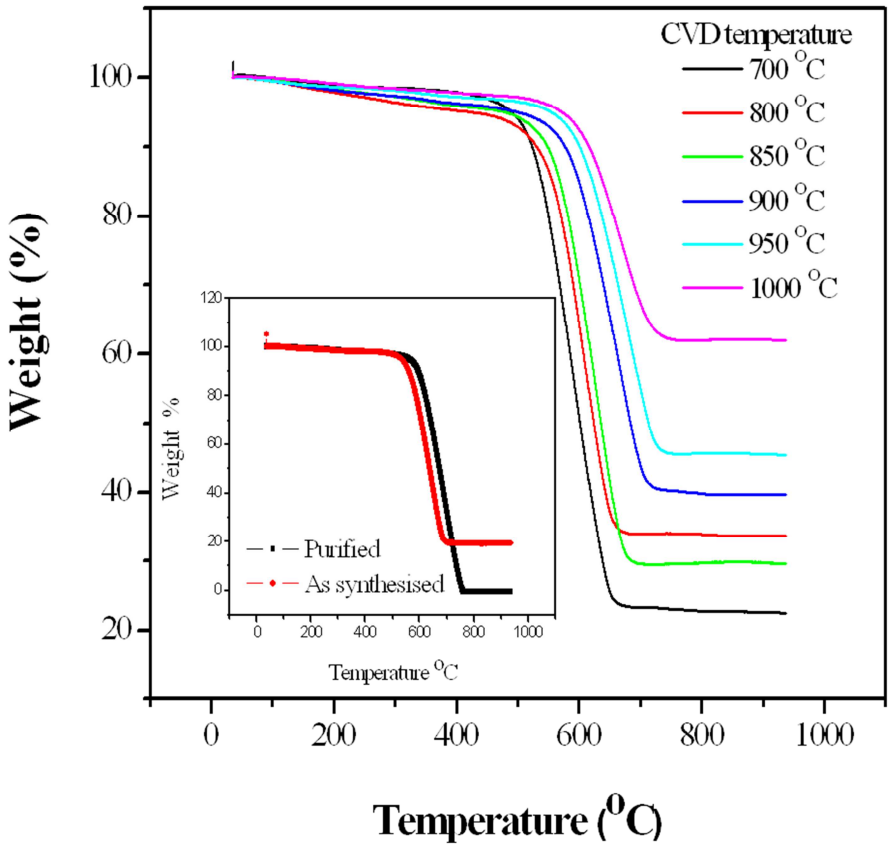

Figure 3.5 Thermogravimetric analysis (TGA) of N-CNTs produced at different CVD temperatures. Insert TGA of the unpurified and purified N-CNT produced at 700 °C.

Figure 3.5 shows the results of the thermogravimetric analysis (TGA), of the unpurified N-CNT samples synthesized at different temperatures using an ethanol/acetonitrile mixture. The residual mass generally increases with reaction temperature, consistent with the data in Figure 3.4 in which the carbon yield generally decreased with reaction temperature. The temperature of decomposition of the N-CNTs also generally increased with increase in synthesis temperature. The lowest decomposition temperature as measured from differential thermogravimetric analysis (DTA) curves (Figure 3.6), was recorded at 580 °C for N-CNTs synthesized at a CVD temperature of 700 °C, with the highest decomposition temperature at 690 °C for N-CNTs synthesized at 950 °C. This result shows that N-CNTs grown at high temperature are more thermally stable. This suggests a decrease in the amount of nitrogen incorporated as well as decrease in the number of defects introduced at high

temperatures. This is also consistent with TEM data; the bamboo compartment size increased with temperature indicating lower nitrogen content at higher temperatures [5]. It is to be noted that the N-CNT material synthesized at 1000 ^{o}C decomposed at a slightly lower temperature of 670°C compared to that of the 950 ^{o}C N-CNT sample (Figure 3.6). This could be due to the presence of more O in the material as a result of functionalization of the N-CNT sidewalls [21]. At higher temperatures (1000 ^{o}C) this effect results in a less stable N-CNT material. Figure 3.5 shows that the final weight remaining after TGA increased from about 20% for the material synthesized at 700 ^{o}C to about 60% for the material synthesized at 1000 ^{o}C. This variation is in agreement with the yields calculated and shown in Figure 3.4. The N-CNT/catalyst ratio decreased with increase in synthesis temperature, *i.e.* more catalyst residue remaining after TGA for the material synthesized at the higher temperatures. The insert in Figure 3.5 shows the TGA profile of an N-CNT sample grown at 700 ^{o}C, before and after purification with HCl to remove of catalyst. The catalyst material was almost completely removed and the material indeed, showed a slight enhancement in thermal stability after purification showing that purification using HCl does not induce defects in the N-CNTs by functionalization.

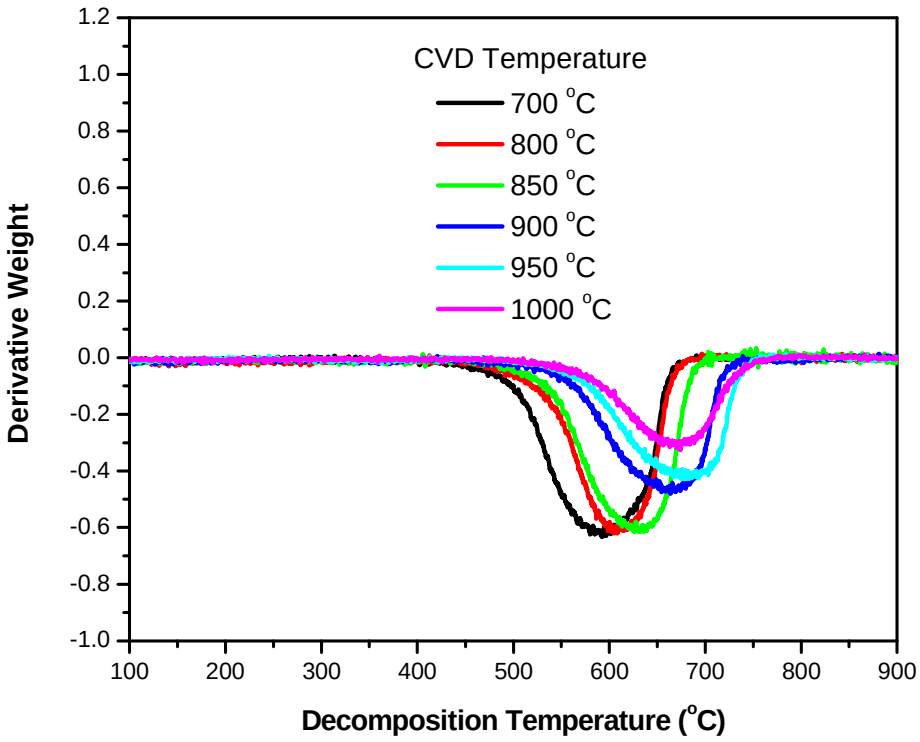

Figure 3.6 Thermogravimetric analysis (DTA) derivative curves for the impure N-CNTs produced at different CVD temperatures.

XPS data were recorded on the various purified products made from ethanol/acetonitrile and the data are shown in Figure 3.7a-e. The asymmetric shapes of the XPS N1s spectra of the synthesized N-CNTs show that several nitrogen species were incorporated in the N-CNTs (Figure 3.7a-d). Atomic nitrogen (N_T) concentration is total N found from the N1s spectrum less molecular N. Four different types of nitrogen species pyridinic N (N_{Pyr}), pyridinic-N-oxide (N_{PO}), quaternary N (N_Q), and molecular N (N_{Mo}) were observed. The atomic nitrogen concentration of each N-type (N_{Pyr}, N_{PO}, N_Q, and N_{Mo}) were obtained by calculating the area under each respective peak in the curves (Figure 3.7) A steady decrease in the level of nitrogen doping with increase in CVD synthesis temperature was noted (Table 3.1); a result confirmed by TEM and TGA data. The XPS result showed an atomic nitrogen concentration of 0.85 % in the N-CNTs synthesized at 700 ^oC (least stable), and a

nitrogen content of 0.1% in N-CNTs synthesized at 1000 ^{o}C. The elemental ratio of the precursor mixture was C: N: O of 61:31:8. The amount of N incorporated in the N-CNT materials in our study is much lower compared to other studies. We relate this to the use of a diluted N-containing carbon source and the presence of O which we suspect inhibits N incorporation in the N-CNT material. The changes in total nitrogen content as well as the amounts of each type of nitrogen found in the N-CNTs are shown in Figure 3.7f and in Table 3.1. Also of note is the decrease in the quaternary N species with temperature. Of significance is the disappearance of the pyridinic N peak at ca. 398 eV at CVD synthesis temperatures above 800 ^{o}C (Figures 3.7c-d). In the N-CNT sample synthesised at 700 ^{o}C we obtained a peak at ca. 402 eV (Figure 3.7a) which we attributed to pyridinic-N-oxide, an oxidised form of the pyridinic N with a $–N^{+}$-O^{-} structure [24].

Table 3.1 Nitrogen content and type of the N-species contained in the N-CNTs grown at different CVD temperatures.

CVD Temperature ^{o}C	N_{Pyr} (%)	N_{PO} (%)	N_Q (%)	N_T (%)	N_{Pyr}/N_T (%)	N_{PO}/N_T (%)	N_Q/N_T (%)	N_{Mo} (%)
700	0.26	0.3	0.30	0.85	30	35	35	0.65
800	0.36	-	0.45	0.81	44	-	56	0.39
850	-	-	0.36	0.36	-	-	100	0.14
900	-	-	0.49	0.49	-	-	100	0.01
1000	-	-	0.10	0.1	-	-	100	-

Pyridinic-N-oxide is only incorporated at low temperatures because it is not stable at high temperatures [25]. Also, the XPS data shows that the molecular nitrogen incoporation at (ca. 404.4 eV) [26] decreases with increase in temperature until it is not present in the material synthesized at 1000 ^{o}C (Figure 3.7e). Pyridinic N is not stable in N-CNTs at high temperatures [7]. Interestingly the most stable species is the quaternary N species as shown by the N_Q/N_T ratio which gradually increases to 100 % of the total N content at high CVD temperatures. The FWHM of the quaternary N is in the range of 1.8 eV for material synthesized at temperatures between 700 ^{o}C and

850 ^{o}C but changes significantly to greater than 2 eV for materials synthesized at 900 and 1000 ^{o}C. At tempeatures above 900 ^{o}C and in the presence of O, surface modification of the carbon nanotubes walls occurs to give pyridine pyrole (–O-C=N) (400.3 eV) and oxidized nitrogen N-O-C (404.5 eV) [27]. This is in agreement with other studies where alcohols were used in the precursor to form functionalized carbon nanotubes [21]. The N1s peaks of such species cannot be fitted independently, thus results in the broadening of the quaternary N peak at 401.2 eV. Pyrrolic N (400.5 eV), was not observed in any of the material synthesized from ethanol/acetonitrile [28]. We suspect that pyrrolic N is not stable in the presence of high oxygen environments and easily oxidizes.

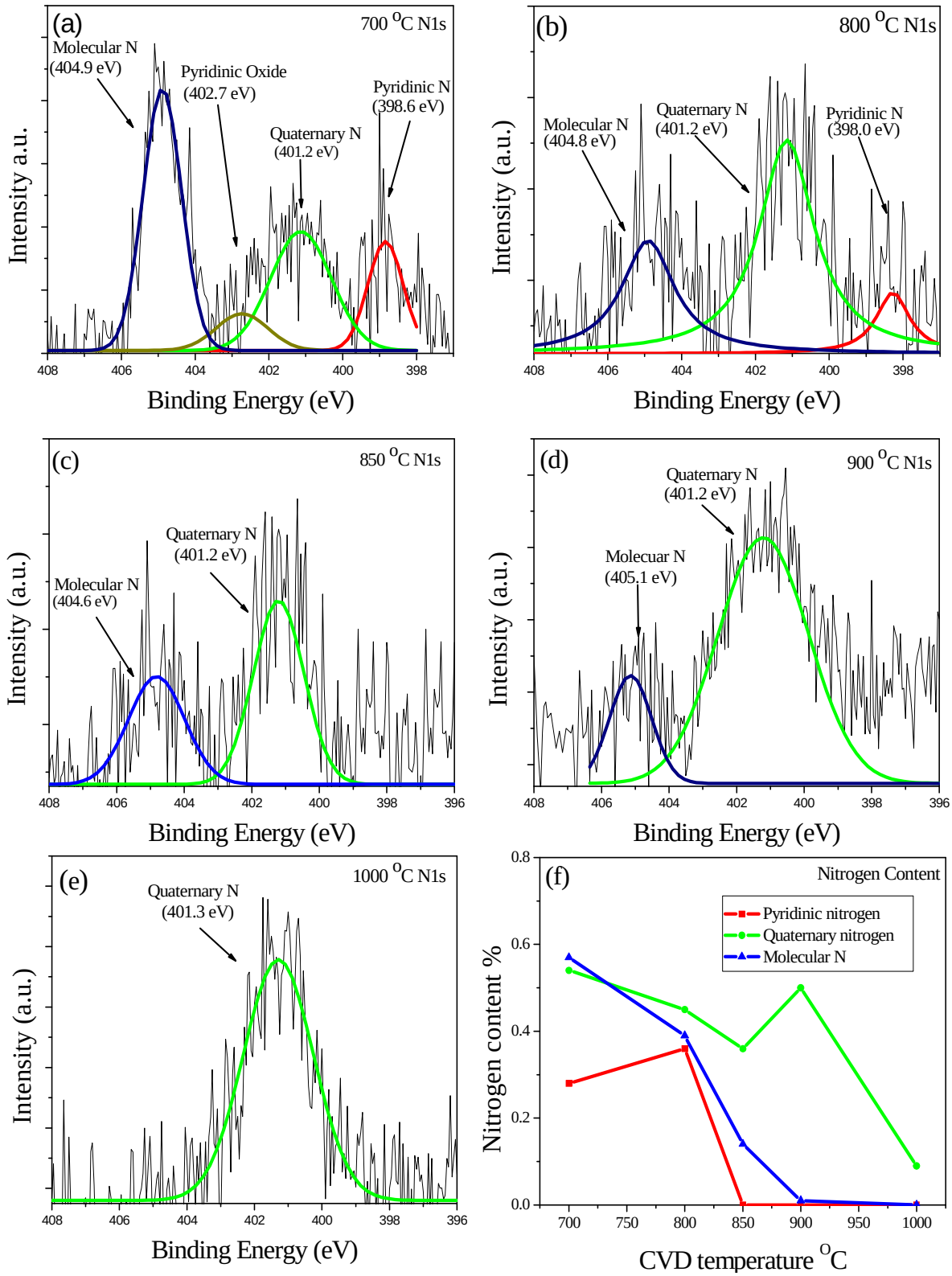

Figure 3.7 XPS N1s spectra of N-CNTs produced at different CVD temperatures: (a) 700 °C, (b) 800 °C, (c) 850 °C, (d) 900 °C, (e) 1000 °C, and (f) nitrogen content in N-CNTs as a function of CVD temperature.

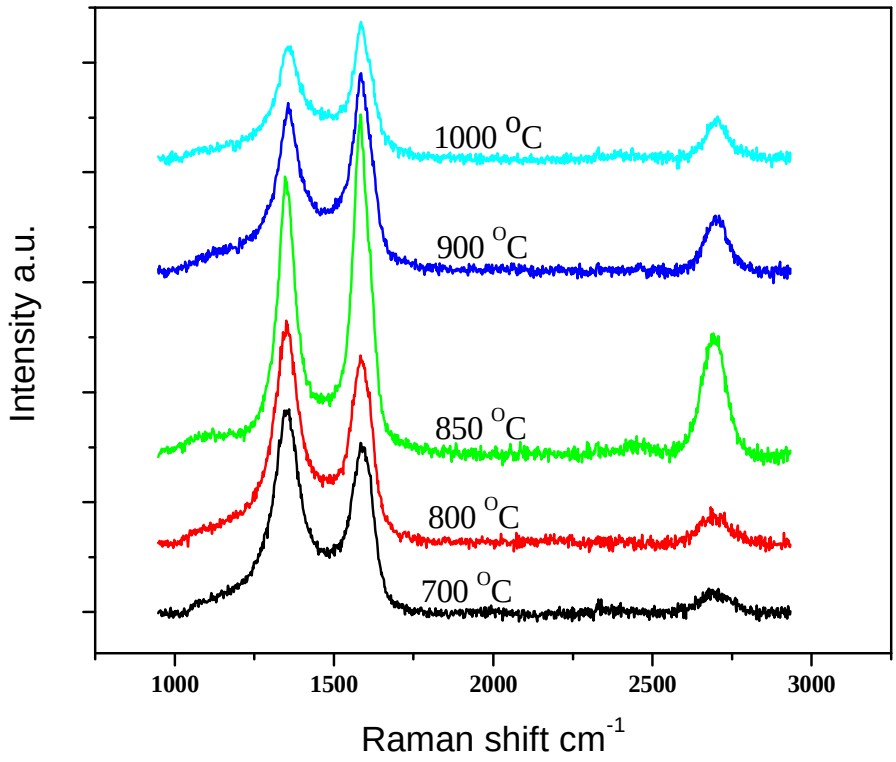

Figure 3.8 Raman spectra of N-CNTs produced from an ethanol/acetonitrile precursor mixture at different CVD temperatures.

The Raman spectroscopy first order peaks at 1350 – 1356 cm^{-1} and at 1583-1592 cm^{-1}, which correspond to the D and the G band respectively, were observed for all the samples studied (Figure 3.8). A comparison of the D-band and the G-band shows that the ratio depends on the CVD synthesis temperature (Figure 3.9). There is a general decrease in the band intensity ratio (I_D/I_G) with increase in CVD temperature, suggesting that the relative degree of order in the N-CNTs improves with an increase in CVD temperature [4, 26]. N-CNTs become more graphitic at high synthesis temperatures since there are fewer defects induced by nitrogen incorporation as was confirmed by XPS data. The (I_D/I_G) intensity ratio of 1.2 at 800 ^oC drops to 0.8 at 850 ^oC. At 850 ^oC, the pyridinic N ceases to be incorporated into the N-CNT material and the decrease in (I_D/I_G) intensity ratio correlates with this absence of pyridinic type N.

This result is consistent with the results of others who have also suggested that the pyridinic type N causes formation of bamboo structures, the main cause of disorder in N-CNTs [29].

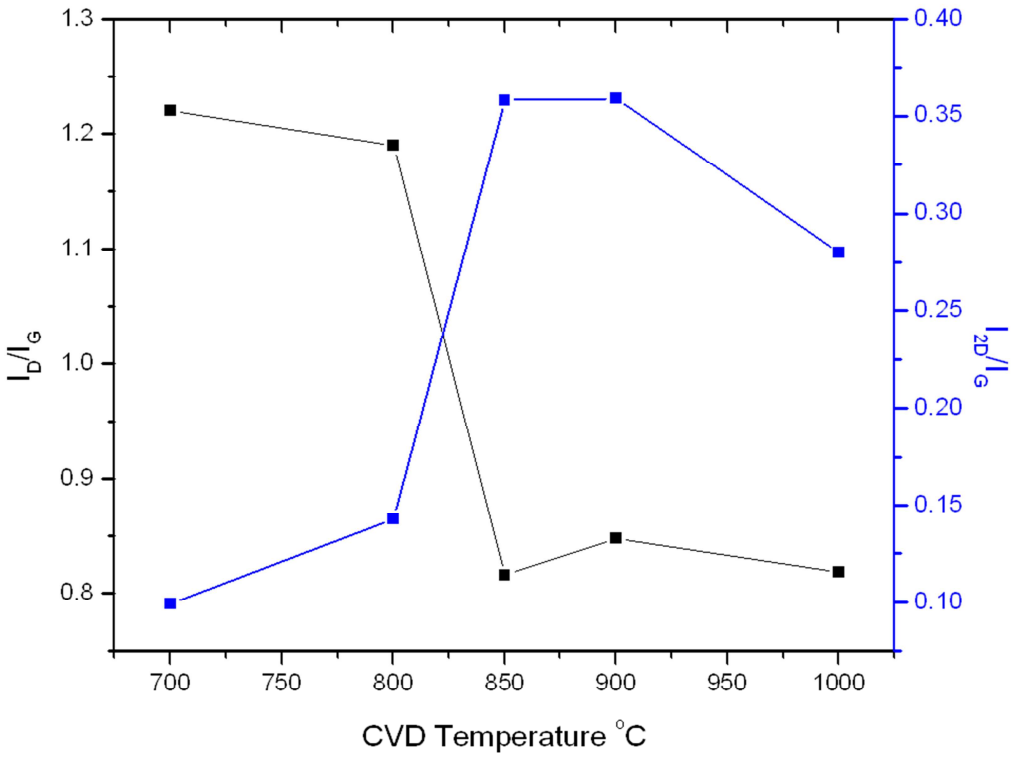

Figure 3.9 Raman spectral intensity ratios of the different N-CNT samples produced at different CVD temperatures.

A peak at approximately 2700 cm^{-1} in the Raman spectrum, a second order Raman band, showed a dependence on growth temperature and nitrogen incorporation. A comparison of the band intensity ratio (I_{2D}/I_G) showed a general increase with increase in CVD temperature (Figure 3.9). The (I_{2D}/I_G) intensity ratio of 0.1 at 800 ^oC rose to 0.36 at 850 ^oC. Changes could relate to the absence of pyridinic type N in the N-CNT material. Both the intensity ratios, (I_D/I_G) and (I_{2D}/I_G), show a large change between N-CNT materials synthesized below 850 ^oC and N-CNTs synthesized above that temperature (Figure 3.9).

3.1.1. Variation of precursor C:N:O ratio.

Short chain alcohols i.e. (methanol and ethanol) yielded N-CNTs with thin walls and smaller diameters while the long chain alcohols (heptanol and octanol) yielded N-CNTs with thick walls (Figure 3.10). When the precursor is a long chain alcohol it contains more carbon which yields thicker walls [20].

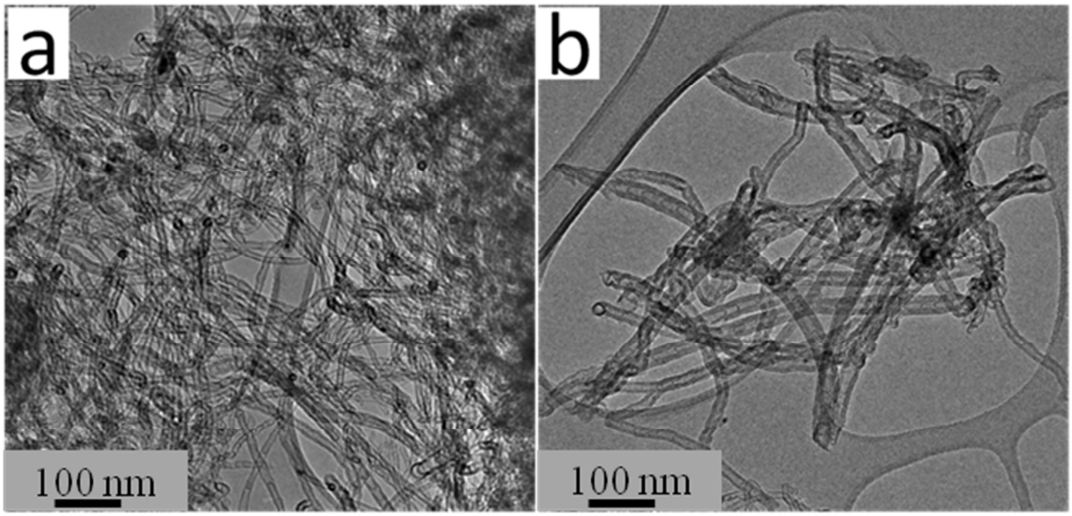

Figure 3.10 TEM images of N-CNTs produced from 20% acetonitrile in (a) methanol and (b) octanol in CVD at 850 °C.

The reaction yields were between 83% and 450% with higher yields found for precursor mixtures containing long chain alcohols (Figure 3.11). This trend is in agreement with that reported previously by others where yields of CNTs produced from aliphatic alcohols were found to be higher when long chain alcohols were used [20].

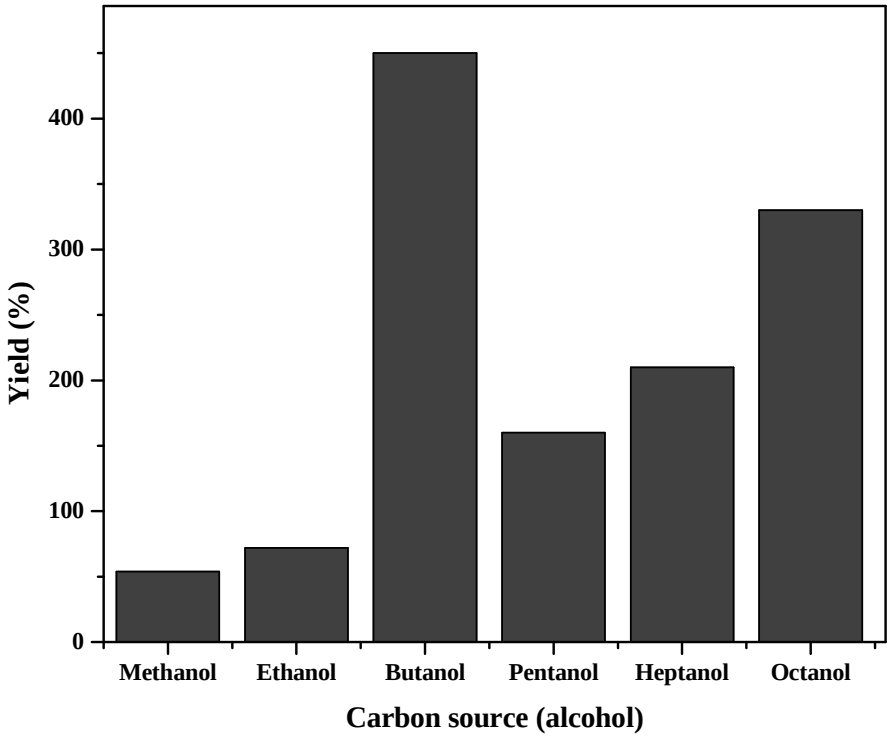

Figure 3.11 The total yield of N-CNT (as a percentage of catalyst material used) as a function of carbon source (alcohol) used in the precursor mixture.

The use of alcohols with different C/O ratios (but with constant acetonitrile and hence N content) could give rise to (i) an increase in N content, if the oxygen content decreased and was responsible for nitrogen loss and (ii) a decrease in N content as the C/N ratio increased if this (and not the O content) controlled the nitrogen content in the N-CNTs. XPS measurements showed that N-CNTs produced from the acetonitrile/alcohol mixtures produced N-CNTs with different amounts of nitrogen viz methanol (0.37 % N), ethanol (0.36 % N), butanol (0.59 % N), pentanol (0.59 % N), heptanol (0.7 % N) and octanol (1.27 % N), respectively (see Figure 3.12). Thus, the oxygen content plays a significant role in determining the nitrogen incorporation in N-CNTs.

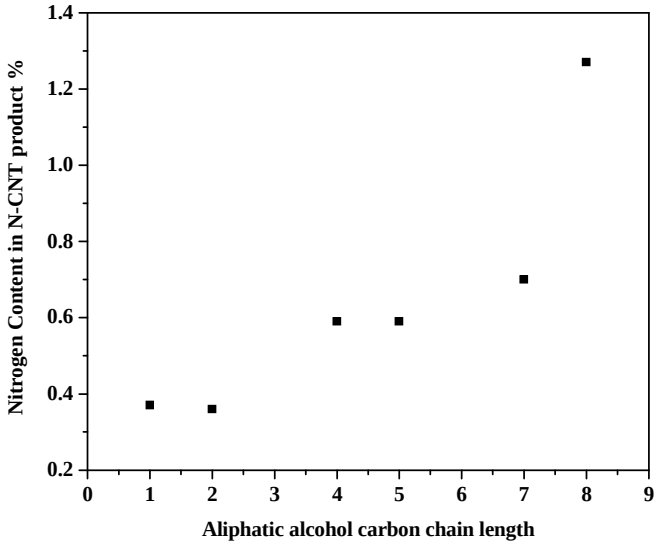

Figure 3.12 The N composition in N-CNTs made from the different alcohol precursor mixtures obtained from XPS analysis.

The asymmetrical shape of the N1s peaks for the XPS data for the purified materials produced from different alcohols showed that different nitrogen species were incorporated in the carbon nanotubes (Figure 3.13a-f). At a high oxygen content in the alcohol (*e.g*. methanol and ethanol), pyridinic nitrogen was not incorporated into the N-CNTs (Figure 3.13a and b). At low O content (*e.g*. heptanol and octanol) pyrollic N ca. 400.8 eV was obtained [24] (Figure 3.13e and f). This is in agreement with our earlier suggestion that pyrollic N is not stable and is easily oxidized at high temperatures and in the presence of high oxygen containing reactants. Molecular nitrogen at ca. 404.4 eV and quaternary N at ca. 401.5 eV were found in all the N-CNT materials as shown in Figure 3.13a – f. The former did not show any general trend while the latter showed a decrease with increase in alcohol chain length in the precursor material (decrease in C/O ratio). The FWHM of the quaternary N is in the range of 1.8 eV for material synthesized from precursors containing ethanol-octanol but changes to greater than 2 eV for material synthesized using the precursor material

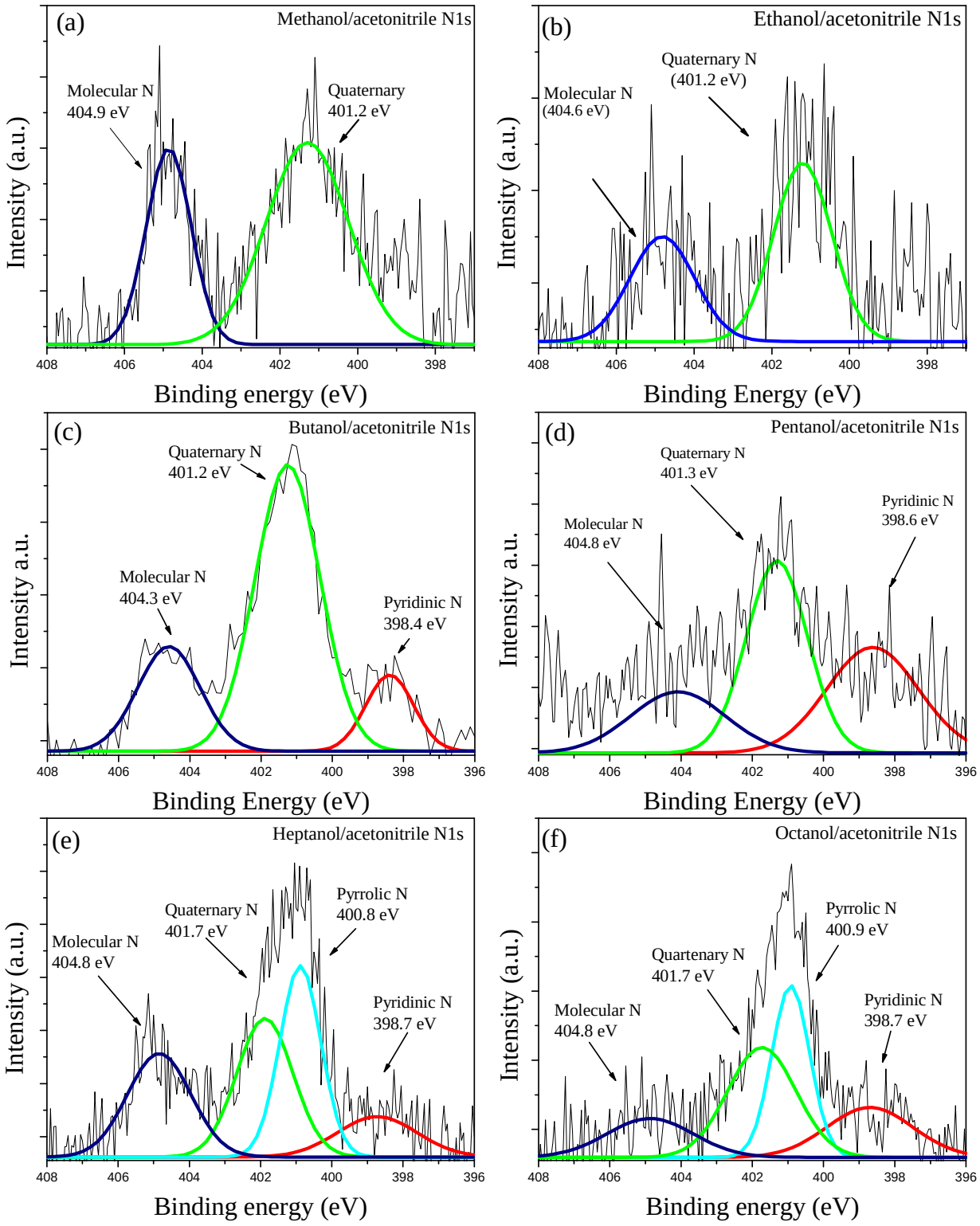

Figure 3.13 XPS N1s spectra of N-CNTs produced in CVD at 850 ^{o}C showing different types of nitrogen incorporated in N-CNTS when (a) methanol, (b) ethanol, (c) butanol, (d) pentanol, (e) heptanol, and (f) octanol were used in the precursor.

containing methanol. The amount of O in this precursor mix is maximum thus the environment is more oxidizing compared to other precursor mixtures. This gives rise to surface modification of CNT walls to give oxidized nitrogen species which broadens the quaternary N peak as explained earlier in the text. The changes in total nitrogen content as well as the amounts of each type of nitrogen found in the N-CNTs are shown in Table 3.2.

Table 3.2 Nitrogen content and type of the N-species contained in the N-CNTs grown at 850 °C using different alcohol precursors.

Alcohol	N_{Pyr} (%)	N_{pyro} (%)	N_Q (%)	N_T (%)	N_{Pyr}/N_T (%)	N_{Pyro}/N_T (%)	N_Q/N_T (%)	N_{Mo} (%)
Methanol	-	-	0.37	0.37	-	-	100	0.13
Ethanol	-	-	0.36	0.36	-	-	100	0.14
Butanol	0.22	-	0.37	0.59	37.3	-	62.7	0.31
Pentanol	0.40	-	0.19	0.59	67.8	-	32.2	0.41
Heptanol	0.20	0.30	0.23	0.70	28.6	42.9	32.9	0.57
Octanol	0.20	0.56	0.51	1.27	15.7	44.1	40.2	0.13

Figure 3.14 shows the Raman spectra for N-CNTs produced from different alcohols. Amongst the alcohols studied, ethanol produced N-CNTs with a more graphitic nature as shown by the I_D/I_G of 0.8 compared to all the others. The N-CNTs produced from ethanol also showed the maximum I_{2D}/I_G ratio of 0.36. The variation of the C/O ratio used in this study made it difficult to correlate the N content in N-CNT materials to the I_D/I_G of the Raman spectra because the variation of C/O ratio also affected crystallinity of produced material [20, 21].

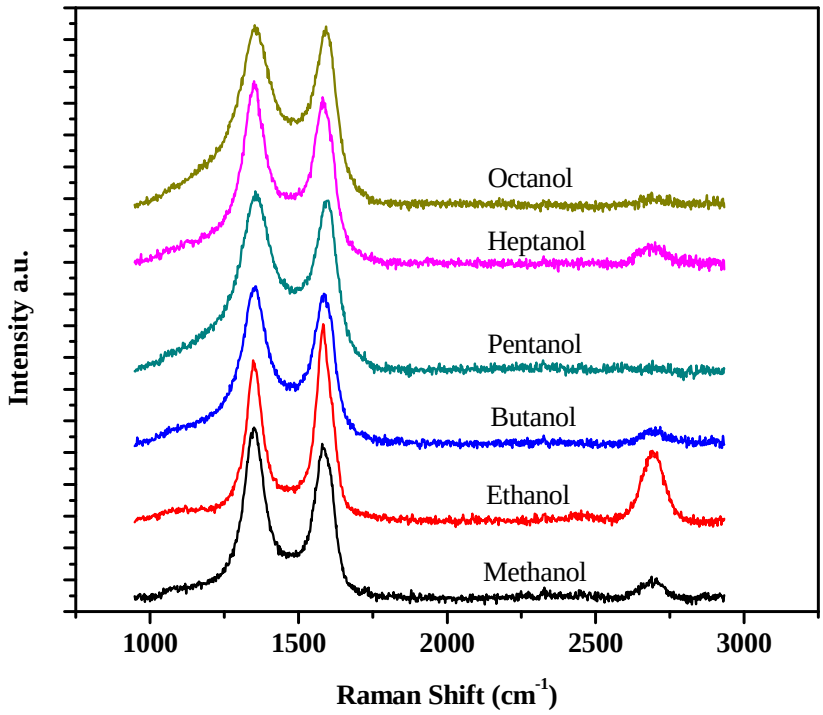

Figure 3.14 Raman spectra of N-CNTs produced from methanol/acetonitrile at different CVD temperatures.

3.4. Conclusion

Nitrogen doped carbon nanotubes, made from different acetonitrile/alcohol mixtures, gave materials with different nitrogen content. At low CVD synthesis temperatures and also at a low precursor oxygen content, a high nitrogen content incorporation is favored. However, as the CVD synthesis temperature is increased and the precursor oxygen content increased (from octanol to methanol), not only does the nitrogen content decrease but the forms of nitrogen incorporated into the N-CNTs also change. Incorporation of pyridinic nitrogen and molecular nitrogen is favored at low temperatures and at low oxygen environments, but these completely disappear at high CVD synthesis temperatures and at a high oxygen content; only quaternary nitrogen is stable under all the reaction conditions.

References

[1] Terrones M, Grobert N, Olivares J, Zhang JP, Terrones H, Kordatos K, et al. Controlled Production of Aligned-Nanotube Bundles. Nature 1997; 388(6637): 52–55.

[2] Nxumalo EN, Coville NJ. Nitrogen Doped Carbon Nanotubes from Organometallic Compounds: A Review. Materials 2010**;** 3(3): 2141-2171.

[3] Ayala P, Arenal R, Ruemmeli M, Rubio A, Pichler T. The Doping of Carbon Nanotubes with Nitrogen and their Potential Applications. Carbon 2010; 48(3): 575-586.

[4] Moldonado S, Morin S, Stevenson KJ. Structure, Composition, and Chemical Reactivity of Carbon Nanotubes by Selective Nitrogen Doping. Carbon 2006; 44(8): 1429–1437.

[5] Nxumalo EN, Nyamori VO, Coville NJ. CVD Synthesis of Nitrogen Doped Carbon Nanotubes using Ferrocene/Aniline Mixtures. J. Organomet. Chem 2008; 693(17): 2942–2948.

[6] Koo´s AA, Dowling M, Jurkschat K, Crossley A, Grobert N. Effect of the Experimental Parameters on the Structure of Nitrogen-doped Carbon Nanotubes Produced by Aerosol Chemical Vapour Deposition. Carbon 2009; 47(14): 30–37.

[7] Yadav RM, Dobal PS, Shripathi T, Katiyar RS, Srivastava ON. Effect of Growth Temperature on Bamboo-Shaped Carbon–Nitrogen (C–N) Nanotubes Synthesized using Ferrocene Acetonitrile Precursor. Nanoscale Res. Lett. 2009; 4(3): 197–203.

[8] Lee CJ, Lyu SC, Kim HW, Lee JH, Cho IC. Synthesis of Bamboo-Shaped Carbon–Nitrogen Nanotubes Using C_2H_2–NH_3–$Fe(CO)_5$ System. Chem. Phys. Lett. 2002; 359(1-2): 115–120.

[9] Eryang X, Jinquan W, Kunlin W, Zhen L, Xuchun G, Yi J, et al. Doped Carbon Nanotube Array with a Gradient of Nitrogen Concentration. Carbon 2010; 48(11): 3097 – 3102.

[10] Ayala P, Grüneis A, Kramberger C, Rümmeli MH, Solórzano IG, Freire FL Jr, et al. Effects of the Reaction Atmosphere Composition on the Synthesis of Single and Multiwalled Nitrogen-Doped Nanotubes. Chem. Phys. 2007; 127(18): 184709.

[11] Czerw R, Terrones M, Charlier JC, Blase X, Foley B, Kamalakaran R, et al. Identification of Electron Donor States in N-Doped Carbon Nanotubes. Nano Lett. 2001; 1(9): 457–460.

[12] Ewels CP, Glerup M. Nitrogen Doping in Carbon Nanotubes. J. Nanosci. Nanotech. 2005; 5(9): 1345-1363.

[13] Ibrahim EMM, Khavrus VO, Leonhardt A, Hampel S, Oswald S, Rümmeli MH, Büchner B. Synthesis, Characterization, and Electrical Properties of Nitrogen-doped Single-walled Carbon Nanotubes with Different Nitrogen Content. Diamond Relat. Mater. 2010; 19(10): 1199–1206.

[14] Biddinger EJ, Deak DV, Ozkan US. Nitrogen-Containing Carbon Nanostructures as Oxygen-Reduction Catalysts. Top. Catal. 2009; 52(11): 1566–1574.

[15] Rao CV, Cabrera CR, Ishikawa Y. In Search of the Active Site in Nitrogen-Doped Carbon Nanotube Electrodes for the Oxygen Reduction Reaction. J. Phys. Chem. Lett. 2010; 1(18): 2622−2627.

[16] Krstic V, Rikken GL, Bernier P, Roth S, Glerup M. Nitrogen Doping of Metallic Single-walled Carbon Nanotubes: n-type Conduction and dipole scattering. Eur. Phys. Lett. 2007; 77(3): 107–110.

[17] Robertson J, Davis CA. Nitrogen Doping of Tetrahedral Amorphous Carbon. Diamond Relat. Mater. 1995; 4(4): 441.

[18] Zhang Y, Lujun P, Wen B, Song X, Liu C, Li T. Influence of Growth Temperature on the Structure, Composition and Bonding Character of Nitrogen-doped Multiwalled Carbon Nanotubes. J. Mater. Res. 2011; 2(3): 443-448.

[19] van dommele S, Romero-Izquirdo A, Bryndson R, de Jong KP, Bitter JH. Tuning nitrogen functionalities in catalytically grown nitrogen-containing carbon nanotubes. Carbon. 2008; 46(1): 138-148.

[20] Bystrzejewski M, Huczko A, Byszewski P, Domańska M, Rümmeli MH, Gemming T, et al. Systematic Studies on Carbon Nanotubes Synthesis from Aliphatic Alcohols by the CVD Floating Catalyst Method. Fullerenes, Nanotubes and Carbon Nanostructures 2009; 17(3): 298-307.

[21] Segura-Cardenas E, Reyes-Reyes M, López-Sandoval R. Effects of Varying the Content of Alcohol in the Reaction Mixture on the Graphitization of MWCNTs and Their Surface Functionalization. J. Phys. Chem. C 2012; 116 (17): 9783–9792

[22] Bachmatiuk A, Schaffel F, Placha D, Martynkova GS, Ioannides N, Gemming T, et al. Tuning Carbon Nanotubes Through Poor Metal Addition to Iron Catalysts in CVD. Fullerenes, Nanotubes and Carbon Nanostructures 2010; 18(1): 37–44.

[23] Teo KBK, Singh C, Chhowalla M, Milne WI. Catalystic Synthesis of Carbon Nanotubes and Nanofibers. In: Nalwa HS. editor. Encyclopedia of nanoscience and nanotechnology. American Scientific Publishers, 2003. p. 1–22.

[24] Liu G, Li X, Lee JW, Popov BN. A Review of the Development of Nitrogen-modified Carbon-based Catalysts for Oxygen Reduction at USC. Catal. Sci. Technol. 2011; 1(2): 207–217.

[25] Liu G, Li X, Ganesan P, Popov BN. Studies of Oxygen Reduction Reaction Active Sites and Stability of Nitrogen-modified Carbon Composite Catalysts for PEM Fuel Cells. Electrochim. Acta 2010; 55(8): 2853–2858.

[26] Liu H, Zhang Y, Li R, Sun X, Desilets S, Abou-Rachid H, et al. Structural and morphological control of aligned nitrogen doped carbon nanotubes. Carbon 2010; 48(5): 1498–1507.

[27] Shen W, Li Z, Liu Y. Surface Chemical Functional Groups Modification of Porous Carbon. Recent Patents on Chemical Engineering, 1 (2008) 27. Recent Patents on Chemical Engineering 2008; 1: 27-40.

[28] Pels JR, Kapteijn F, Moulijn JA, Zhu Q, Thomas KM. Evolution of nitrogen functionalities in carbonaceous materials during pyrolysis. Carbon 1995; 33(11): 1641–1653.

[29] Tao XY, Zhang XB, Sun FY, Cheng JP, Liu F, Luo ZQ. Large-scale CVD synthesis of nitrogen-doped multi-walled carbon nanotubes with controllable nitrogen content on a $Co_xMg_{1-x}MoO_4$ catalyst. Diamond Relat. Mater. 2007; 16(3): 425–30.

Chapter 4

Structural evolution of nitrogen bonding in nitrogen doped carbon nanotubes on annealing

4.1 Introduction

The doping of carbon nanotubes (CNTs) with nitrogen (N) to enhance their properties in different functional systems has been studied by several workers [1,2,3]. Nitrogen can be incorporated in the carbon matrix of the nitrogen doped carbon nanotube (N-CNT) in a variety of forms, namely; pyrrolic N, pyridinic N, pyridinic-N-oxide and quaternary N. Molecular nitrogen and oxides of nitrogen are also found physically adsorbed on the N-CNT walls [4]. The type of N incorporated in the N-CNT material influences the electronic properties [5,6] and the behavior of the material as a catalyst [7]. For example; in oxygen reduction electro-catalysis reactions, quaternary N speeds up the O reduction reaction whilst pyridinic N lowers the potential required to start the oxygen reduction reaction [8,9]. In organic photovoltaic solar cells the N-CNTs selectively transport electrons to the metal cathode [10]; this is likely due to the presence of quaternary N as dopant. Quaternary N has a delocalized electron which dopes the extended graphene layer of the N-CNT thereby making the material n-type [11,12]. Control of the N type incorporated in the N-CNT material is thus important if N-CNTs are to be tailor made for specific applications. The current knowledge of how the bonding configuration or location of the nitrogen dopant in N-CNTs can be influenced is lacking.

Several methods of incorporating N in CNTs including i*n-situ* N doping [13,14,15] and *ex-situ* N doping [16,17,18] have been widely investigated. However, all these methods lack the ability to control the type of the N structures which can be incorporated into the N-CNT material. In an earlier study we showed that to some extent using *in-situ* N doping the amount and type of N, incorporated in N-CNT

material can be influenced during growth not only by the N content in the precursor material but also by growth conditions such as reaction temperature and oxidizing environment [19]. A problem with such control of N species is that changes in the reaction environment also bring about changes in morphology and changes in the crystalinity of the formed materials [20]. Changes in morphology and crystalinity also affect the properties of carbon nanotubes. *Ex-situ* doping could be used in this case, but its lack of control over the type of nitrogen incorporated in the CNT materials still remains a drawback [17,18]. Thermal treatment of N-CNTs to change the N forms, could provide an attractive procedure to tune the N forms in N-CNTs whilst not changing other characteristics of the N-CNTs. Indeed, studies have been conducted to change the amount of N in N-CNT material by heat treatment under inert conditions [21,22]. In these studies, quaternary and pyridinic N rich materials were used. However, while the N content was reduced no significant conversion from one N type into another in the N-CNT material was reported. More recently it was shown that the pyridinic N structures in carbon nanotubes could be converted to quaternary N structures by thermal treatment under inert conditions [23]. These two different results, [21,22,23] can only be explained if different nitrogen structures react differently to thermal treatment. Pyridinic nitrogen and quaternary nitrogen appear to be stable in N-CNTs and notable changes to these structures can only be induced at high temperatures. By contrast pyrrolic N appears to be unstable at high temperatures and will thus react to form more stable N structures. Thus N-CNT materials containing pyrrolic N will be an ideal material to obtain an insight into how N structures form in N-CNTs.

N-CNTs containing high concentration of pyrrolic N have been prepared reproducibly by using a mixture of a carbon source and nitrogen-containing precursor material in the CVD synthesis of N-CNTS at low CVD temperatures [19]. CNTs grown at low CVD temperatures at atmospheric pressure give well formed tubular morphologies with small and uniform diameters, and smooth walls [24]. It is possible to modify the N forms in such high quality N-CNTs after synthesis by annealing at temperatures

below 1000 ^{o}C. The N-CNTs should retain their good quality and this could provide a useful procedure to prepare different N-CNT materials in applications requiring different forms (and amounts) of N.

4.2 Experimental

N-CNTs were synthesized using a chemical vapor deposition method from a precursor mixture containing acetonitrile and heptanol over a Fe/Al/MgO catalyst at 700 °C [19]. We used the produced material to prepare N-CNT films using a vacuum filtration method [25].To form an N-CNT film, 2 mg of the purified, CVD grown N-CNTs were dispersed by ultrasonication in 1 L of 10% sodium dodecyl sulphonate (SDS) (Sigma) surfactant suspension in water. 20 ml of the suspension was vacuum filtered onto 220 nm pore size, mixed cellulose ester membrane (Millipore), and followed by washing with copious quantities of deionized water to remove the surfactant. To transfer the N-CNT film to the SiO_2/Si substrates, a wet membrane was placed N-CNT film side down onto the a SiO_2/Si substrate. The assembly was subsequently covered with clean porous paper and loaded with a 2 kg mass to dry flat overnight, leaving the nanotube film (with its filtration membrane still attached) adhered to the SiO_2/Si substrate. The mixed cellulose ester membrane was dissolved in successive acetone baths followed by a final methanol bath. The N-CNT films on SiO_2/Si were left to dry in air. The N-CNT films were heated to (100-800 °C) for two hours under a 7% H_2 in N_2 gas mixture (N_2/H_2) atmosphere. The N-CNT materials were characterized by transmission electron microscopy (TEM), scanning electron microscopy (SEM) and atomic force microscopy (AFM). X-ray photoemission spectroscopy and Raman spectroscopy was used to study the changes in the structure of the material due to the heat treatment.

4.3 Results and discussion

The morphological properties of the synthesized N-CNT material and the fabricated N-CNT thin films were investigated by Transmission Electron Microscopy (TEM), Scanning Electron Microscopy (SEM), and Atomic Force Microscopy (AFM). Figure 1a shows the TEM image of the N-CNT sample synthesized using the CVD method

at 700 °C from a heptanol/acetonitrile precursor mixture under an N_2/H_2 gas atmosphere. The TEM image (Figure 4.1a) shows that all the nanotubes exhibit the bamboo structure morphology associated with nitrogen incorporation in carbon nanotubes [26]. The diameter of the N-CNTs ranges from 15-40 nm. Figure 4.1b shows a SEM image of an N-CNT film transferred on to a silicon oxide substrate showing only N-CNTs. This was also confirmed by AFM imaging of the same film (Figure 4.1c). The procedure used in this study allowed us to obtain N-CNTs with uniform and small diameters, good tubular morphology and smooth walls.

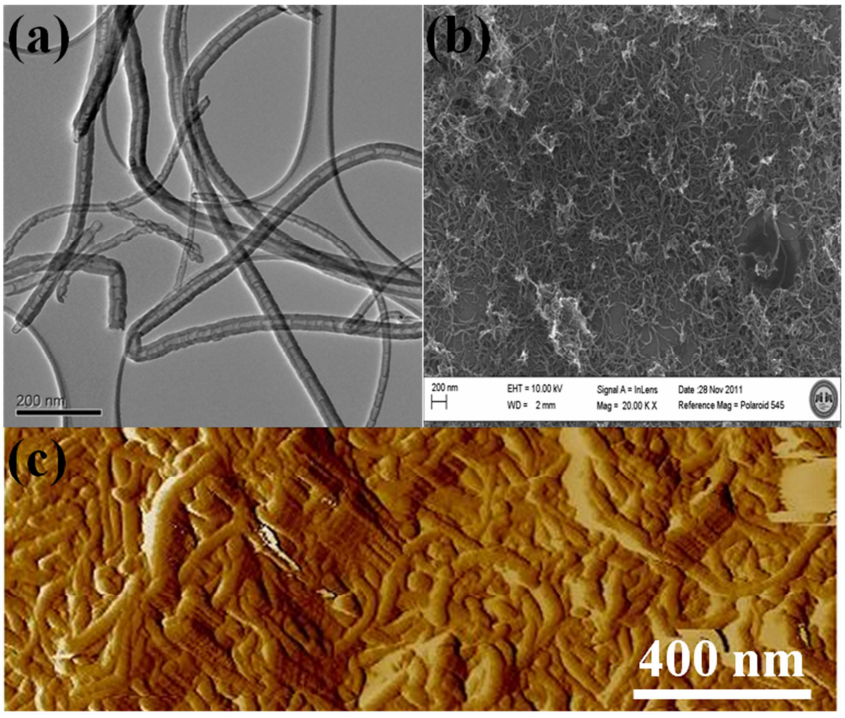

Figure 4.1 TEM image of N-CNTs produced from a 20% acetonitrile in ethanol solution at 700 °C, (b) SEM image of N-CNT film made by the vacuum filtration method, and (c) AFM image of N-CNT film made by vacuum filtration and transferred onto a silicon substrate.

The chemical components and the N bonding configurations in the N-CNTs were investigated by X-ray photoelectron spectroscopy (XPS). The full XPS spectra of the N-CNTs show peaks at around 285.0, 401.0, and 531.0 eV which we attributed to the C1s, N1s, and O1s signals, respectively. Figure 4.2a-f shows the high resolution N1s XPS spectra of the N-CNT films annealed at 100, 200, 400, 600, and 800 °C under a

N_2/H_2 gas atmosphere. All the N-CNT films studied in this work were initially heated to 100 ^oC to drive off moisture introduced in the N-CNTs during the solution processing of the thin films. Four peaks at binding energies of 407.8, 404.8, 402.0 and 400.3 eV were observed on the high resolution N1s spectra of the films annealed at 100 ^oC (Figure 4.2a). The peak at 407.8 eV is not usually found in N doped carbon materials. The N1s peak at 407.8 eV is the hallmark of nitrate like species [27]. This peak originates from the residual nitro cellulose-containing mixed ester membrane material filter used during the N-CNT film deposition step. We assigned the peak at 404.0 eV to the molecular N species [28] contained inside the containers formed by the bamboo compartments in the N-CNTs [29]. The smaller peak at 402.0 eV shows the presence of pyridinic-N-oxide in the material [30,31]. The pyridinic-N-oxide species is not stable in the carbon material, but considering that the N-CNTs were formed from an O containing precursor material and at a low temperature of 700 ^oC, it appears that some pyridinic-N-oxide species were incorporated in the N-CNT material [32]. The peak at 400.3 eV is assigned to the pyrrolic N species [33]. Pyrrolic nitrogen is nitrogen positioned out of the benzene ring of the graphitic structure; this is usually incorporated in a more amorphous carbon material. The pyrrolic N peak at 400.3 eV is broad with a FWHM of 4 eV, this is evidence of other N species which appear near that binding energy in smaller amounts like quaternary N at 401.0 eV [34], and pyridinic N above 398.1 eV [19].

We further annealed all the films at 200 °C to drive off the remaining nitro cellulose-containing mixed ester membrane residues [35]. After annealing at 200 °C, the nitrate-like N peak at 407.8 eV disappeared (Figure 4.2b). From this, we concluded that the N found at 407.8 eV does not form any C-N bonds with the carbon material in the N-CNT structure. The pyridinic-N-oxide species is not stable in carbon materials and upon annealing at 200 °C under a H_2/N_2 gas atmosphere it disappeared. This was accompanied by the appearance of a small pyridinic N peak at 398.2 eV (Figure 4.2a-b). Pyridinic-N-oxide was reduced to pyridinic N upon annealing at 200 °C. No changes were noticed in the pyrrolic N peak at 400.1 eV.

The intensity of the pyridinic N peak at 398.1 eV increased on the N-CNT film sample which was annealed at 400 ^{o}C (Figure 4.2c). This was accompanied by the sharpening of the pyrrolic N peak at 400.6 eV as shown by a decrease in the FWHM of the pyrrolic N peak from 4 eV to 3 eV. The sharpening of the pyrrolic N peak (400.6 eV) and an accompanying increase in the intensity of the pyridinic N peak shows that, indeed some of the pyrrolic N was converted to pyridinic N. The thermal annealing at 400 ^{o}C under a N_2/H_2 gas environment enables condensation reactions to take place in the N-CNT structure.

At 600 ^{o}C the pyrolic peak at 400.6 eV completely disappears (Figure 4.2d). A new peak appears at 401.0 eV. The peak at 401.0 eV is assigned to a quaternary type N. The pyridinic N concentration decreased after annealing at 600 ^{o}C, *i.e.* some pyridinic N was converted to quaternary N and some was lost as N_2. This is supported by the accompanying decrease in the total N content in the N-CNT material. On annealing at 600 ^{o}C under a N_2/H_2 gas environment, condensation reactions take place in the N-CNT structure forming both pyridinic N and quaternary N structures from the pyrrolic N. Also, condensation reactions of the pyridinic N structures to form quaternary N take place.

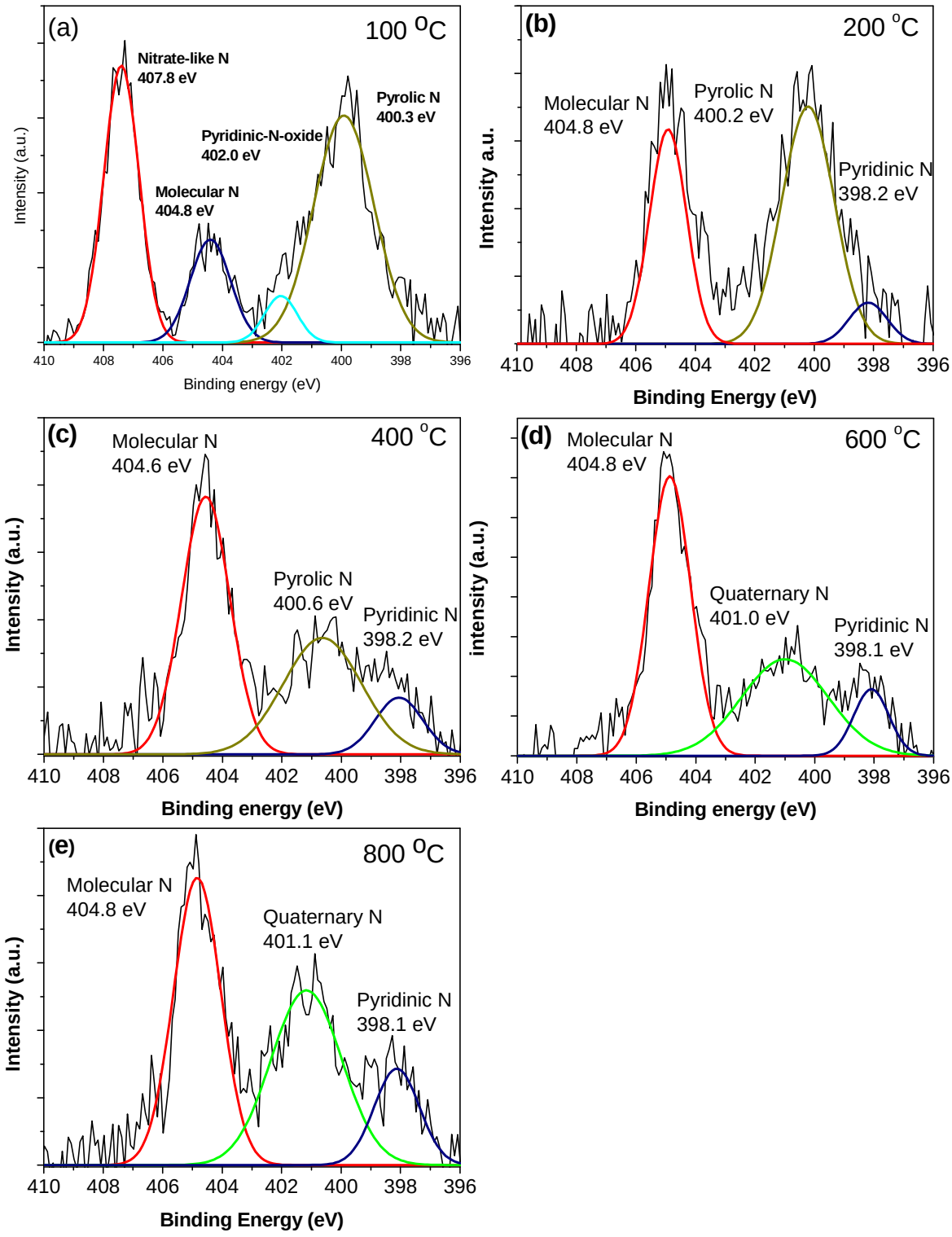

Figure 4.2 XPS N1s spectra of N-CNT films annealed under vacuum and a H_2 gas flow at: (a) 100 °C, (b) 200 °C, (c) 400 °C, (d) 600 °C, (e) 800 °C.

Other than the sharpening of the quaternary N peak and the pyridinic N peak in the N1s spectrum, no further changes in N species were noticed when the material was annealed at 800 ^{o}C (Figure 4.2e). The FWHM of the quaternary N peak at 401.0 eV reduces from 3 eV for material annealed at 600 ^{o}C to 2.0 eV indicating that the remaining pyrrolic N converts totally to pyridinic and quaternary N.

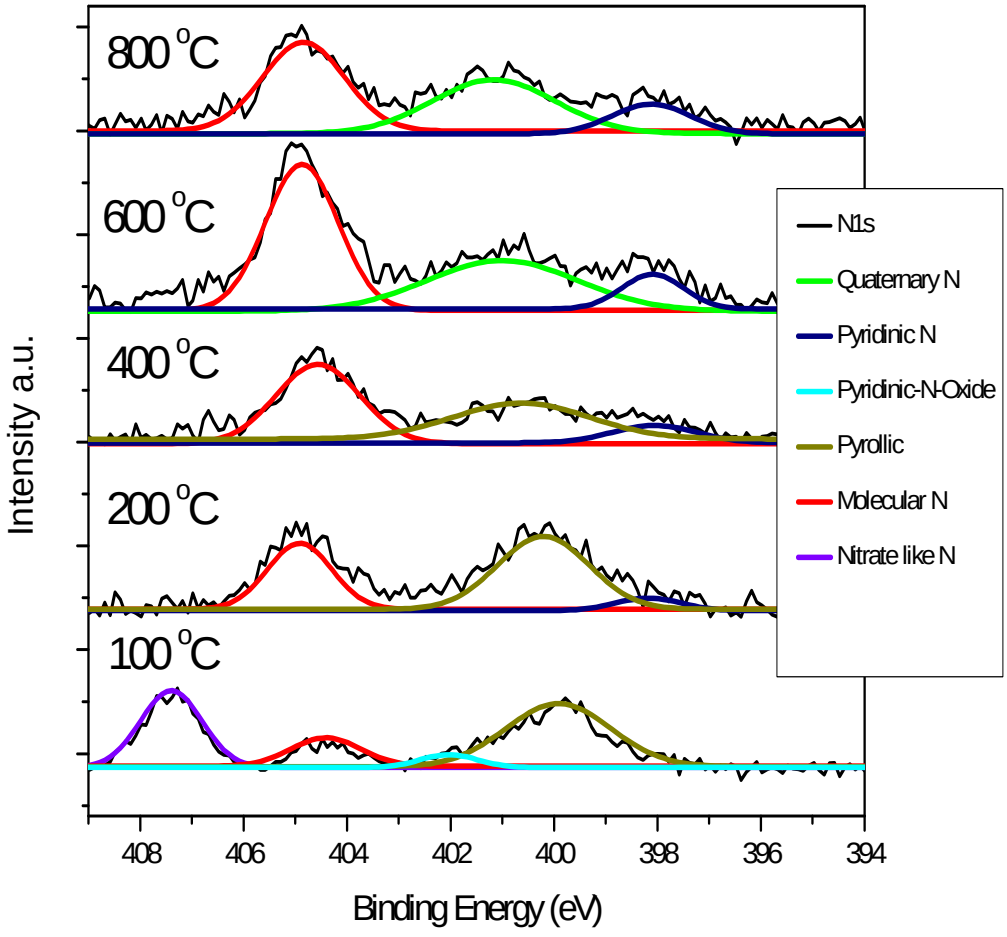

Figure 4.3 XPS N1s spectra of N-CNT films annealed at 100 ^{o}C, 200 ^{o}C and 600 ^{o}C.

Figure 4.3 shows in summary the changes in the peaks and peak position that occur on annealing the N-CNTs at temperatures ranging from 100 ^{o}C to 800 ^{o}C. Figure 4.4 shows the structures of the carbon matrix containing different types of N species and

the changes which take place as the matrix is annealed. The pyrrolic N and the pyridinic N appear on the edges of the graphene matrix or on defect sites within the graphene matrix. The quaternary N appears in the graphene matrix of the N-CNT material. As discussed before the changes in the N structures become apparent after annealing at temperature of 400 ^{o}C and above. The pyrrolic N structures on the edges of the graphene matrix condense to form pyridinic N on annealing. The pyridinic N structures found on the defect sites within the graphene matrix also condense to form the quaternary N species on annealing at 600 ^{o}C. This explains why the amount of pyridinic N show a decrease in the N-CNT material annealed at above 600 ^{o}C. Condensation reactions which incorporate N structures like pyridinic N and quaternary N, on annealing, take place with the help of O containing functional groups which give water and ammonia as leaving groups [19, 36]. In our case these were present since in the N-CNT material was synthesized using heptanol, an O containing precursor which helps in functionalizing the material during synthesis [37].

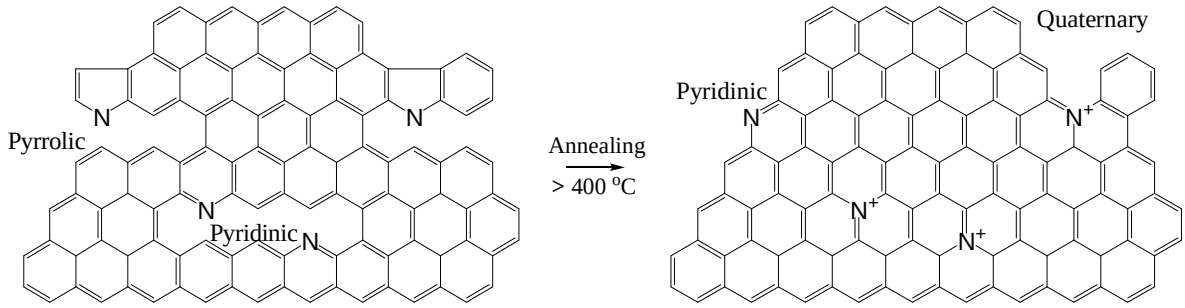

Figure 4.4 Typical condensation reactions involving (a) pyrrolic N forming pyridinic N, (b) pyrrolic N forming quaternary N and (c) pyridinic N forming quaternary N when annealing N-CNTs at temperatures above 400 ^{o}C under inert conditions.

The N concentration calculated from N/ (N+C) at. % was found to decrease with annealing temperatures as shown in Table 4.1. Changes in the concentration of the different N structures are also shown. This result indicates that most of the nitrogen is lost on annealing between 600 ^{o}C and 800 ^{o}C where quaternary N structures are

formed. During the condensation reactions at 600 ^{o}C some of the pyrrolic N and the pyridinic N structures are lost as N_2 and gaseous N oxides.

Table 4.1 - Nitrogen Content and type of the N structures in the N-CNTs after annealing at different temperatures

Annealing Temperature (^{o}C)	Total N (%)	Pyridinic-N-Oxide (%)	Pyrrolic N (%)	Pyridinic N (%)	Quaternary N (%)
100	1.55	0.18	1.37	-	-
200	1.50	-	1.31	0.19	-
400	1.47	-	1.17	0.30	-
600	1.30	-	-	0.29	1.01
800	1.17	-	-	0.20	0.97

Raman spectroscopy was used to study the changes in the graphitic structure of the N-CNTs after annealing. Figure 4.5 shows the Raman spectra of all the N-CNT films studied in this work showing the disorder induced D bands and the G bands which arises from the sp^2 carbon networks of the CNT structure [38]. Analysis of the Raman spectra (Figure 4.6) showed that there is a general decrease in the I_D/I_G ratio from 0.99 in the films annealed at 100 ^{o}C to 0.92 for the films annealed at 800 ^{o}C. The percentage change in the I_D/I_G between the films annealed at 100 ^{o}C and those annealed at 800 ^{o}C is only 7%. The small change in the I_D/I_G signifies some slight improvement in the graphitic structure of the N-CNTs on annealing. However the changes are very small, showing that the graphitic structure of the N-CNTs after treatment remained largely the same. Some N-CNT materials synthesized at different temperatures showing similar changes in N show much larger changes in I_D/I_G [19]. This shows that our method of starting with the pyrrolic N structures in the N-CNT material and inducing changes by annealing at temperatures below 1000 ^{o}C, can

result in the formation of the more attractive and stable N forms whilst leaving the graphitic structure of the material greatly unchanged.

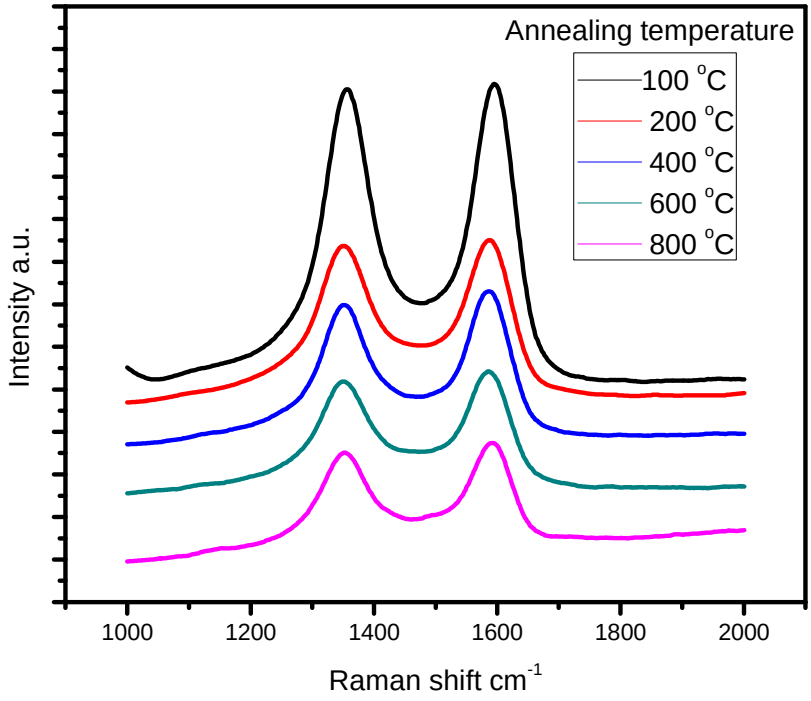

Figure 4.5 Raman spectra of N-CNTs produced from methanol/acetonitrile at different CVD temperatures.

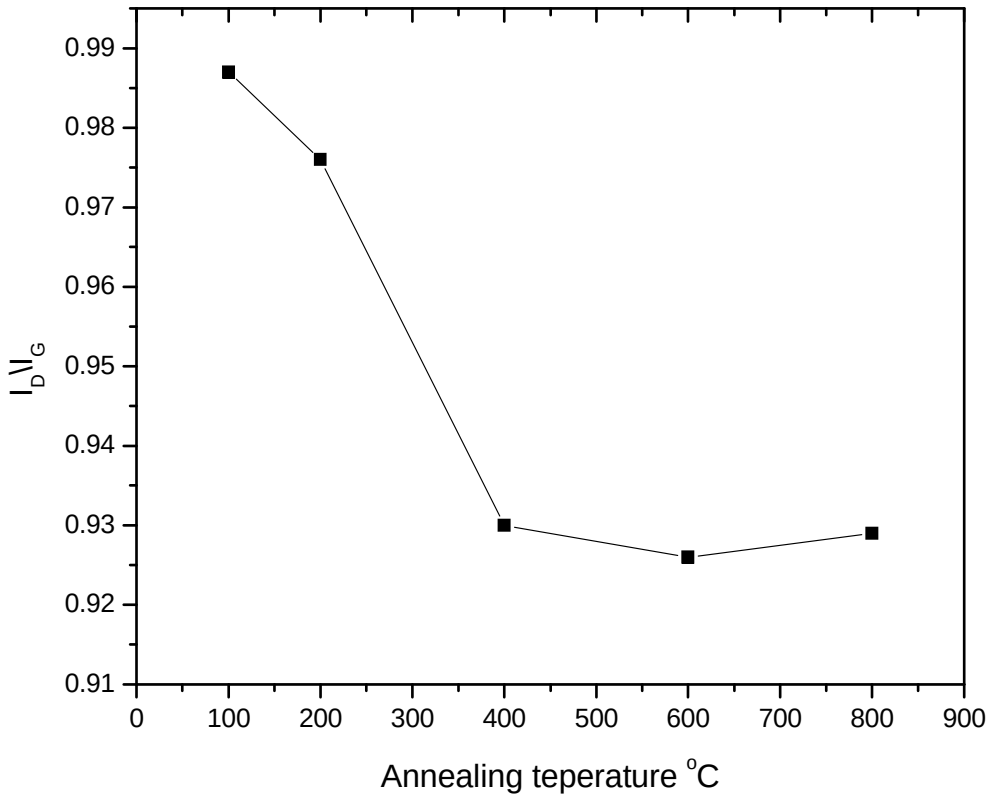

Figure 4.6 Raman spectral intensity ratios of the different N-CNT films annealed at different temperatures under a N_2/H_2 gas flow.

4.4 Conclusion

In this contribution we have shown that it is possible to change the type of N in N-CNT materials by annealing. The pyrrolic N structures are converted to the more stable pyridinic N and quaternary N structures. This research part has evidenced that the N forms in N-CNTs can be changed after the N-CNTs have already been formed. This sustain that the properties of the N-CNTs with the same morphology but different amounts and forms of N can be investigated to evaluate the effect of amount and N forms in N-CNT material.

References

1 Ayala P, Arenal R, Ruemmeli M, Rubio A, Pichler T. The doping of carbon nanotubes with nitrogen and their potential applications. *Carbon* 2010;48(3):575–86.

2 Hassan FM., Chabot V, Li J, Kim BK, Ricardez-Sandovaland L, Yu A. Pyrrolic-structure enriched nitrogen doped graphene for highly efficient next generation supercapacitors. *J. Mater. Chem. A*, 2013, 1, 2904-2919.

3 Sharifi T, Hu G, Jia X, and Wagberg T. Formation of Active Sites for Oxygen Reduction Reactions by Transformation of Nitrogen Functionalities in Nitrogen-Doped Carbon Nanotubes. *Acs. Nano* 2012; 6(10): 8904–8912.

4 Liu H, Zhang Y, Li R, Sun X, Désilets S, Abou-Rachid H, et al. Structural and morphological control of aligned nitrogen-doped carbon nanotubes. *Carbon* 2010; 48(5): 1498-1507.

5 Zinfer R. Ismagilov, Anastasia E. Shalagina, Olga Yu. Podyacheva, et. al. Structure and electrical conductivity of nitrogen-doped carbon nanofibers. *Carbon* 2009; 7: 1922–1929.

6 Wiggins-Camacho JD and Stevenson KJ. Effect of Nitrogen Concentration on Capacitance, Density of States, Electronic Conductivity, and Morphology of N-Doped Carbon Nanotube Electrodes. *J. Phys. Chem. C* 2009;113: 19082–19090.

7 Sharifi T, Hu G, Jia X, and Wagberg T. Formation of Active Sites for Oxygen Reduction Reactions by Transformation of Nitrogen Functionalities in Nitrogen-Doped Carbon Nanotubes. *Acs. Nano* 2012; 6(10): 8904–8912.

8 Niwa H, Horiba K, Harada Y, Oshima M, Ikeda T, Terakura K, et. al. X-ray Absorption Analysis of Nitrogen Contribution to Oxygen Reduction Reaction in Carbon Alloy Cathode Catalysts for Polymer Electrolyte Fuel Cells. J. *Power Sources*. 2009; 187: 93–97.

9 Lai LF, Potts JR, Zhan D, Wang L, Poh CK, Tang C, et.al. Exploration of the Active Center Structure of Nitrogen-Doped Graphene- Based Catalysts for Oxygen Reduction Reaction. *Energy Environ. Sci.* 2012; 5: 7936–7942.

10 Lee JM, Park JS, Lee SH, Kim H, Yoo S and Kim SO. Selective Electron- or Hole-Transport Enhancement in Bulk-Heterojunction Organic Solar Cells with N- or B-Doped Carbon Nanotubes. *Adv. Mater.* 2011; 23: 629–633.

11 Krstic V, Rikken GL, Bernier P, Roth S and Glerup M. Nitrogen doping of metallic single-walled carbon nanotubes: n-type conduction and dipole scattering. Eur Phys Lett 2007; 77(3): 107–10.

12 Robertson J and Davis CA. Nitrogen doping of tetrahedral amorphous carbon. *Diamond Relat Mater*. 1995; 4(4): 441.

13 Eryang X, Jinquan W, Kunlin W, Zhen L, Xuchun G, Yi J, et al. Doped carbon nanotube array with a gradient of nitrogen concentration. *Carbon*. 2010;48(11):3097–102.

14 Ayala P, Gruneis A, Kramberger C, Rummeli MH, Solo´rzano IG, Freire Jr FL, et al. Effects of the reaction atmosphere composition on the synthesis of single and multiwalled nitrogen-doped nanotubes. *Chem. Phys*. 2007; 127(18): 184709.

15 Ewels CP, Glerup M. Nitrogen doping in carbon nanotubes. J. *Nanosci. Nanotechnol*. 2005; 5(9): 1345–63.

16 Bangert U, Bleloch A, Gass MH, Seepujak A, and van den Berg J. Doping of few-layered graphene and carbon nanotubes using ion implantation. *Phys. Rev. B* 2010; 81: 245423

17 Xu F, Minniti M, Barone P, Sindona A, Bonanno A, Oliva A. Nitrogen doping of single walled carbon nanotubes by low energy N_2^+ ion implantation. *Carbon* 2008; 46 :1489–1496

18 Lee JM, Park JS, Lee SH, Kim H, Yoo S and Kim SO. Selective Electron- or Hole-Transport Enhancement in Bulk-Heterojunction Organic Solar Cells with N- or B-Doped Carbon Nanotubes. *Adv. Mater*. 2011; 23: 629–633.

19 Bepete G, Tetana ZN, Lindner S, Rummeli MH, Chiguvare Z, Coville NJ. The use of aliphatic alcohol chain length to control the nitrogen type and content in nitrogen doped carbon nanotubes. Carbon 2013; 52 :316 –325.

20 Van Dommele S, Romero-Izquirdo A, Brydson R, De Jong KP, and Bitter JH. Tuning nitrogen functionalities in catalytically grown nitrogen-containing carbon nanotubes. Carbon 2002; 46: 138-148.

21 Choi HC, Bae SY, Jang WS, and Park J. Release of N2 from the Carbon Nanotubes via High-Temperature Annealing. *J. Phys. Chem. B* 2005; 109: 1683-1688.

22 Liu H, Zhang Y, Li R, Sun X and Abou-Rachid H. Thermal and chemical durability of nitrogen-doped carbon nanotubes. J. Nanopart. Res. 2012; 14: 1016: 1-8.

23 Sharifi T, Hu G, Jia X, and Wagberg T. Formation of Active Sites for Oxygen Reduction Reactions by Transformation of Nitrogen Functionalities in Nitrogen-Doped Carbon Nanotubes. *Acs. Nano* 2012; 6(10): 8904–8912.

24 Li WZ, Wen JG and Ren ZF, Effect of temperature on growth and structure of carbon nanotubes by chemical vapor deposition. Appl. Phys. A ;2002: 74, 397–402.

25 Wu Z, Chen Z, Du X, Logan JM, Sippel J, Nikolou M, et. al. Transparent, conductive carbon nanotube films. *Science* 2004, *305*(5688), 1273-1276.

26 Lee CJ, Lyu SC, Kim HW, Lee JH, and Cho KI. Synthesis of bamboo-shaped carbon–nitrogen nanotubes using C_2H_2–NH_3–$Fe(CO)_5$ system. *Chem. Phys. Lett.* 2002; 359: 115–120.

27 Baltrusaitis J, Jayaweera PM and Grassian VH. XPS study of nitrogen dioxide adsorption on metal oxide particle surfaces under different environmental conditions. Phys. Chem. Chem. Phys. 2009; 11: 8295–8305.

28 Liu H, Zhang Y, Li R, Sun X, Desilets S, Abou-Rachid H, et al. Structural and morphological control of aligned nitrogen doped carbon nanotubes. Carbon 2010;48(5):1498–507.

29 Reyes-Reyes M, Grobert, Kamalakaran R, Seeger T, Golberg D, Ruhle M, et.al. Efficient encapsulation of gaseous nitrogen inside carbon nanotubes with bamboo-like structure using aerosol thermolysis. *Chem. Phys. Lett.* 2004; 396: 167–173.

30 Liu G, Li X, Lee JW, Popov BN. A review of the development of nitrogen-modified carbon-based catalysts for oxygen reduction at USC. Catal Sci Technol 2011;1(2):207–17.

31 Ayala P, Gruneis A, Gemming T, Buchner B, Rummeli MH, Grimm D, et al. Influence of the catalyst hydrogen pretreatment on the growth of vertically aligned nitrogendoped carbon nanotubes. Chem Mater 2007;19:6131–7

32 Xiao B, Boudou JP, and Thomas KM. Reactions of Nitrogen and Oxygen Surface Groups in Nanoporous Carbons under Inert and Reducing Atmospheres. *Langmuir* 2005; 21: 3400-3409.

33 Pels JR, Kapteijn F, Moulijn JA, Zhu Q, Thomas KM. Evolution of nitrogen functionalities in carbonaceous materials during pyrolysis. Carbon 1995;33(11):1641–53.

34 Rao CV, Cabrera CR, Ishikawa Y. In search of the active site in nitrogen-doped carbon nanotube electrodes for the oxygen reduction reaction. J Phys Chem Lett 2010;1(18):2622–7.

35 Lee K, Wu Z, Chen Z, Ren F, Pearton SJ, and Rinzler AJ. Single Wall Carbon Nanotubes for p-Type Ohmic Contacts to GaN Light-Emitting Diodes. Nano Lett. 2004, 4(5) 911-914.

36 Seredych M, Hulicova-Jurcakova D, Lu GQ and Bandosz TJ. Surface functional groups of carbons and the effects of their chemical character, density and accessibility to ions on electrochemical performance. *Carbon*, 2004, *46*(11), 1475-1488.

37 Segura-Cardenas E, Reyes-Reyes M, López-Sandoval R. Effects of varying the content of alcohol in the reaction mixture on the graphitization of MWCNTs and their surface functionalization. *J. Phys. Chem. C* 2012; 116(17): 9783-9792.

38 Pimenta MA, Dresselhaus G, Dresselhaus MS, Cancado LG, Jorioa A and Saito R. Studying disorder in graphite-based systems by Raman spectroscopy. *Phys. Chem. Chem. Phys.*, 2007, 9, 1276–1291.

Chapter 5

LPCVD growth of multilayer graphene on copper using low methane flow rates: Growth from below

5.1 Introduction

Graphene is an atomically thick material made of carbon atoms bonded together in a hexagonal lattice, with extraordinary properties. These include large Young's modulus (1,100 GPa)[1], high charge carrier mobility (≈ 200,000 cm^2V/s)[2], high thermal conductivity (5,000 W/mK)[3], a large specific surface area (2,630 m^2/g)[4] and an ultimate strength of 130 GPa.[1] Since its discovery in 2004, graphene application in proof-of-concept devices such as solar cells, transistors, sensors, ultracapacitors and touch screens has been demonstrated[5,6,7,8,9]. Low pressure chemical vapor deposition (LPCVD) of graphene on copper using methane and hydrogen is one of the most prominent methods in use for producing uniform, high quality and large area graphene in a reproducible way [10].

The mechanism of graphene growth on copper has been widely studied and there appears to be an agreement that the synthesis of graphene by LPCVD on copper using methane and hydrogen is a self limiting process which results in the formation of monolayer graphene [11]. Graphene formation on copper follows a self-limiting chemical vapor deposition growth because of the low carbon solubility in copper (< 0.0001 atomic %) [10]. The nucleation and growth of graphene is determined by supersaturation of active carbon species on the copper surface. Active carbon species originate from the decomposition of methane on the copper surface and/or in the gas phase depending on the growth temperature and methane concentration in the system. At a critical supersaturation point, nucleation of graphene is triggered, followed by aggregation of the active carbon species resulting in the growth of graphene into big graphene domains [12] The graphene growth only stops after the growing domains merge with other graphene domains growing from other nucleation sites [13]. After

complete copper catalyst coverage, interaction between methane and copper ceases because the monolayer graphene covers the entire copper surface. However, this mechanism only explains the growth of graphene on copper using carefully optimized methane concentrations. Graphene growth using a high methane concentration or atmospheric pressure chemical vapor deposition (APCVD) is not a self limiting process and multilayer graphene is often produced [14]. When copper is exposed to a large concentration of methane and/ or when the reaction takes place at atmospheric pressure, it is possible that another critical supersatuaration point is exceeded resulting in nucleation and growth of a bilayer or multilayer graphene domain [13]. The number of layers in the multilayer graphene will thus depend on the concentration of methane used in the graphene growth process.

To the best of our knowledge the above two mechanisms are the only ones which are used to explain the formation of single layer and multilayer graphene on copper. Here we report on the LPCVD growth of multilayer graphene using methane flow rates less than that required for monolayer or bilayer graphene growth. It is expected that low flow rates of methane will yield non-continuous patches of monolayer graphene even when there is a continuous supply of methane, as reported before [15]

In this work we investigated the effect of time and methane concentration on the formation of graphene layers on copper. We propose a mechanism which explains how multilayer graphene can form using low flow methane systems. We explain this result using the kinetic processes occurring during the nucleation stage and subsequent graphene growth under low flow regimes and long methane exposure times. Three flow regimes were investigated; low methane flow (5 sccm and 10 sccm), medium methane flow (15 – 30 sccm) and high methane flow (40 and 80 sccm). We made sure that the total amount of methane we passed over a Cu catalyst remained constant in each reaction in all the different flow regimes studied. This means that we kept $Qt = k$ where Q is flow rate in sccm, t is time in minutes and k is a constant. We used optical imaging and Raman spectroscopy to evaluate the nature of the graphene produced under different flow regimes.

5.2 Experimental

5.2.1 Synthesis and transfer

Graphene was synthesized by a chemical vapor deposition (CVD) method. Copper foil (25 µm thick, Alpha Aesar) was used as the catalyst in this study. A 1 cm × 2 cm copper foil was inserted into the centre of a cylindrical quartz tube reactor (22 cm × 100 cm). The reactor was evacuated to 30 torr. A 7 % H_2 in N_2 (H_2/N_2) gas mixture (Air Gas, batch analyzed grade) was introduced into the reactor at 80 sccm whilst the vacuum was kept at 30 torr for a further 15 minutes. The reactor was then heated to 995 °C at 10 °C per minute under vacuum. The reactor was held at 995 °C for a further 30 minutes after which methane gas (Air product, Ultrahigh purity) was also introduced at a flow rate Q and the reaction was allowed to continue for time t. Q and t were varied in such a way that Qt remained a constant. The methane flow was stopped and the reactor was cooled under the H_2/N_2 gas at 80 sccm.

The graphene was transferred from the Cu foil onto a silicon substrate with a 300 nm silicon oxide layer (SiO_2/Si). In summary, 5 mm × 5 mm copper foil squares were cut from the 1 cm × 2 cm copper foil catalyst used and poly(methyl methacrylate) (PMMA) (Mico Chem) was spin coated onto the surface of the copper square on a spin coater (3000 rpm). The copper was then etched away from the doped graphene/PMMA layers (3 hours) in a 1M solution of $FeCl_3$ contained in a petri dish. After all the copper had been etched away, the graphene/PMMA was left floating in the $FeCl_3$ solution and was then washed several times in a 1M solution of HCl, followed by washing in water. Lastly the graphene/PMMA was attached to a cleaned SiO_2/Si substrate and was left to dry for 2 hours in air at ambient temperature. The PMMA was removed from the graphene by dissolving the PMMA in acetone. This was achieved by placing the PMMA/graphene on the SiO_2/Si in a petri dish containing acetone which was left standing for 15 minutes. The acetone was decanted and replaced by fresh acetone, and the process was repeated 3 times. Lastly the graphene was washed in methanol (to ensure complete removal of PMMA/acetone residues) and left to dry in air at ambient conditions.

5.2.2 Characterization

The doped and undoped graphene samples were characterized on SiO_2/Si substrates unless otherwise stated. Optical images of the graphenes were recorded using an optical microscope. Raman spectra were measured on an InVia Raman microscope (Reinshaw) at an excitation wavelength of 514 nm.

5.3 Results and discussion

Optical microscopy and Raman spectroscopy techniques were used to characterize the graphene materials synthesized under the different synthesis conditions. Important morphological features of the graphene materials grown under different conditions were revealed by optical images of the different graphene films transferred on to the SiO_2/Si (Figure 5.1). Optical images of the graphene transferred on to SiO_2/Si indicate

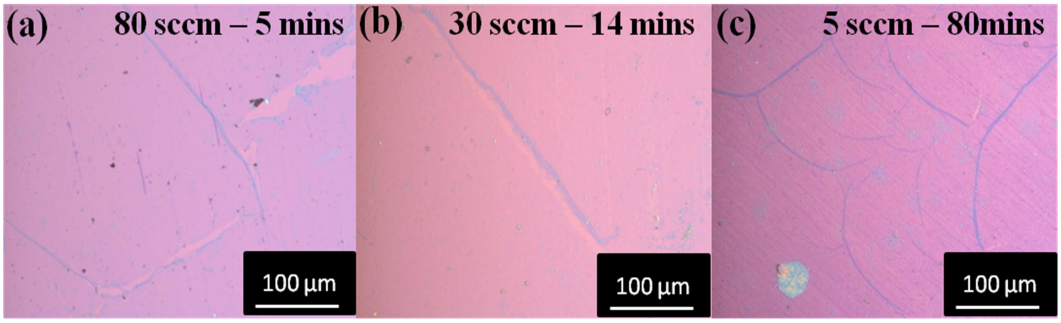

Figure 5.1 Optical micrographs of graphene grown under different flow-time systems showing different colors suggesting different layers of the produced graphene.

variation in film thickness. This was achieved by the change of colour contrast in the optical images, due to the light interference on the SiO_2 layer modulated by the number of layers of the graphene [16]. The darker the colour of the Si/SiO_2 substrate, the thicker the graphene is. The thickness of the graphene films ranges from monolayer graphene to multilayer graphene. Complete graphene coverage was realized in each of the reactions in all the graphene growth reactions studied in this work. Raman analysis was used to ascertain the defect density, quality and variation in the thickness of graphene. A low intensity of the disorder-induced D band (~1350

cm^{-1}) was observed in all the graphene products indicating that all the products were of high quality and contained little sp^3 carbon [17].

5.3.1 High flow rate and short exposure time

Figure 5.1a shows the optical image of graphene grown under an 80 sccm methane flow rate for 5 minutes. A uniform and continuous graphene film was produced, indicating that at the given flow rate and growth time, the conditions were suitable to complete the graphene coverage on the copper catalyst. The dark pink colour suggests a bilayer graphene film [16]. Raman spectroscopy of graphene grown using the fast flow regime suggested that high quality graphene was grown as indicated by the small intensity of the D band. Analysis of the Raman spectra obtained for the graphene gave an I_G/I_{2D} ratio between 0.63 and 0.86 which suggest that at least a double layer graphene was formed [18].

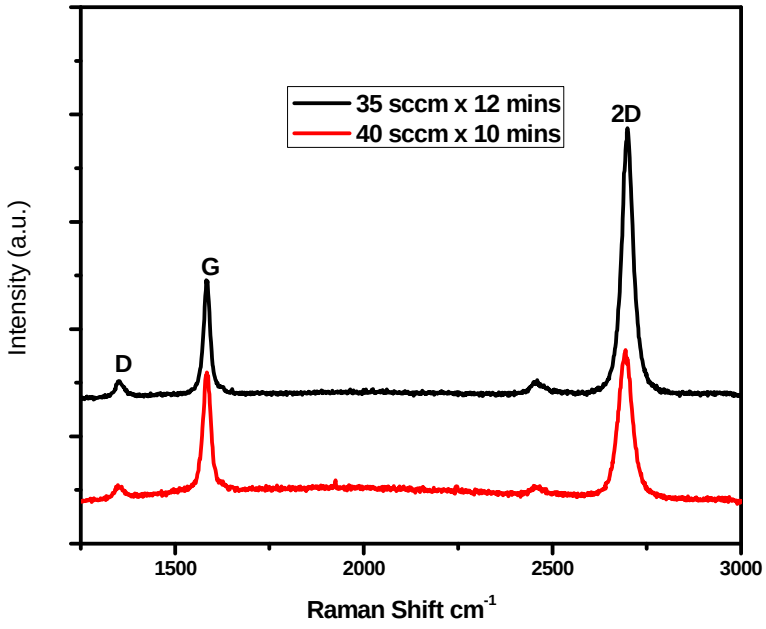

Figure 5.2 Raman spectra of graphene films grown under the high flow rates and short growth times measured with a 514.5 nm excitation.

5.3.2 Medium flow rate and medium exposure time

Figure 5.1b show the optical microscopy image of the graphene films synthesized under a methane flow rate of 30 sccm for 14 minutes. The film shows a uniform and continuous monolayer graphene film. The small D band in the Raman spectra of the graphene synthesized using methane flow rates between 20 sccm to 30 sccm suggest that high quality graphene was formed in all the different flow rates used in this regime. Analysis of the Raman spectra gave an I_G/I_{2D} ratio of between 0.43 and 0.36 which suggest that monolayer graphene was produced [18]. This means that in our setup the methane flow rate in this flow-time regime gave good monolayer graphene formation.

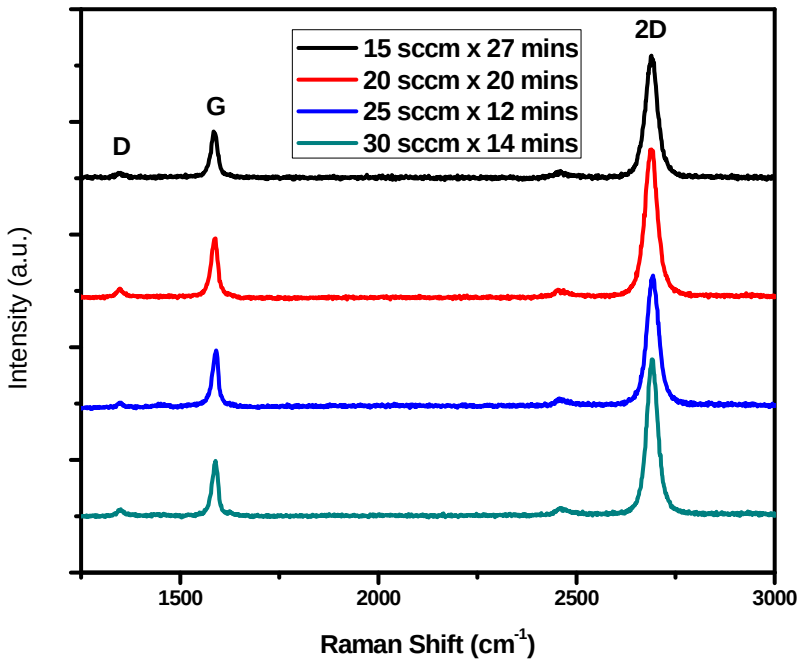

Figure 5.3 Raman spectra of graphene films grown under the medium flow rate and medium growth times measured with a 514.5 nm excitation.

5.3.3 Low flow rate and long exposure times

Full coverage of continuous graphene was obtained on copper under the low flow regime as shown in the optical image of the graphene transferred on to SiO_2/Si substrates (Figure 5.1c). Interestingly, the graphene films are dark pink, suggesting

that multilayer graphene was produced in this case. Analysis of the Raman spectra gave an I_G/I_{2D} intensity ratio > 1 which confirms that indeed, multilayer graphene was produced [18]. This is unusual because we would expect monolayer graphene to grow since even lower methane flow rates were used here as compared the other two flow regimes discussed earlier in which monolayer and bilayer graphene was formed. Of interest here is also the fact that the I_G/I_{2D} of the graphene produced at 10 sccm for 40 minutes was 1.24 whilst that of graphene produces at 5 sccm for 80 minutes was 1.70. This suggest that the graphene synthesized using a 5 sccm flow rate had more

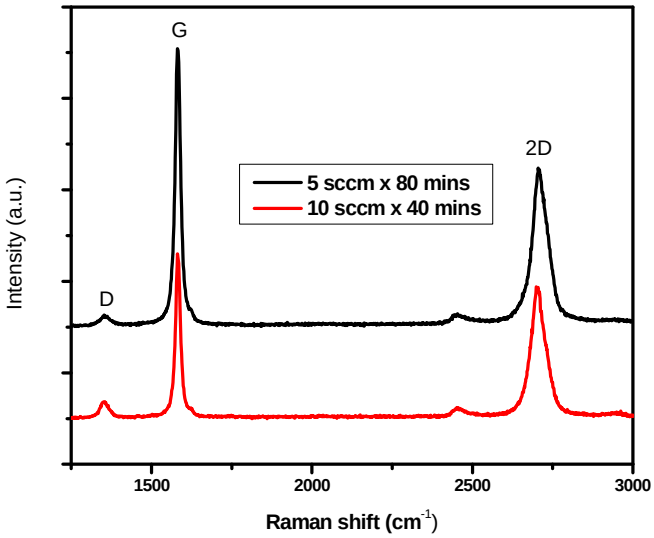

Figure 5.4 Raman spectra of graphene films grown under the low flow rates and long growth times measured with a 514.5 nm excitation.

layers compared to the one synthesized at 10 sccm. The formation of multilayer graphene could be related to the extended times used in this flow regime.

In the two studies before (section 5.3.1. and 5.3.2.) maximum exposure time for each flow regime were 12 and 27 minutes respectively. To check if extended growth times could form graphene of different thicknesses we ran three reactions one from each regime described above. Here, flow rates of 80 sccm, 30 sccm and 5 sccm were used for an extended time of 180 minutes. From the Raman data analysis (Figure 5.5) we found that, a double layer graphene in the reaction using 80 sccm, monolayer

graphene in the reaction using 30 sccm as expected and multilayer graphene in the reaction using 5 sccm methane flow rate were formed. The I_G/I_{2D} ratio of the graphene material synthesized using a 5 sccm flow rate was 2.3. This suggests that an even thicker film was formed compared to the one grown using the same flow rate for 80 minutes. These results indicate a self limiting reaction mechanism for the fast flow and the medium flow systems but a different mechanism in which graphene continuously grow with time for the slow flow regime.

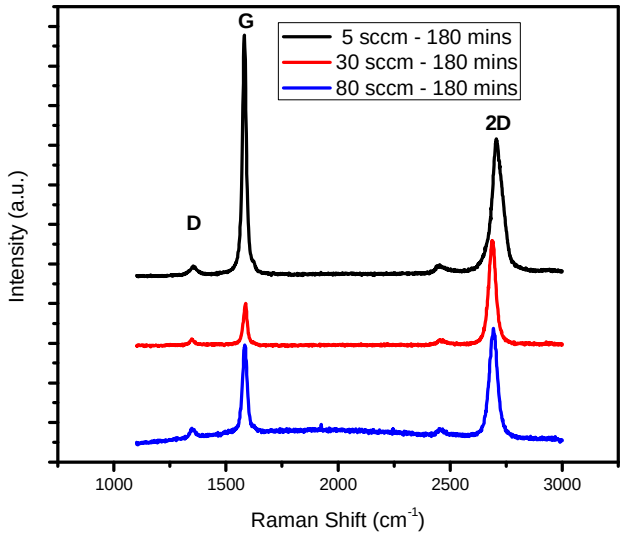

Figure 5.5 Raman spectra of graphene films grown under different regimes of flow rates and growth times measured with a 514.5 nm excitation.

The reactions involving very low methane flow rates appear to follow a mechanism from a mechanism involving nucleation at a critical supersatuaration point followed by aggregation. A different mechanism is required to explain the formation of multilayer graphene at very low flow rates and a prolonged time. The rate of growth of graphene is limited because the rate of addition of carbon species to the nucleated graphene is slow [19]. Slow coverage of graphene on Cu results in the continuous addition of carbon on the exposed parts of the copper foil. In this slow CH_4 regime it is difficult to reach the critical supersatuaration point so few nucleation sites are produced. Graphene growth is also limited because there is a low concentration of

active carbon species on the copper. Graphene coverage is thus slow leaving the copper surface exposed. This allows active carbon to diffuse on the copper surface to the areas covered by graphene. In this case graphene nucleation can occur under the graphene surface followed by aggregation to form bilayer and multilayer graphene.

5.4 Conclusion

We have shown that it is possible using LPCVD and copper catalyst to form graphene of different thickness and quality by varying the carbon supply rate and time of exposure. The differences in thickness arises from the difference in the kinetic processes during the nucleation stage and growth stages under different flow regimes. We have also shown, for the first time that it is possible to grow multilayer graphene using LPCVD on copper by reducing the carbon supply rate and performing the reaction over extended periods of time. The findings from this work are important because the formation of multilayer graphene obtained by LPCVD can be represented by a simple model. Also, a method to tune graphene to required thickness during growth in LPCVD is presented.

References

1 Lee C, Wei X, Kysar JW and Hone J. Measurement of the elastic properties and intrinsic strength of monolayer graphene. *Science* 2008; 321(5887): 385–388.

2 Bolotin KI, Sikes KJ, Jiang Z, Klima M, Fudenberg G, Hone J, et al. Ultrahigh electron mobility in suspended graphene. *Solid State Commun*. 2008; 146(9–10): 351–355.

3 Balandin AA, Ghosh S, Bao W, Calizo I, Teweldebrhan D, Miao F, et al. Superior thermal conductivity of single-layer graphene. *Nano Lett*. 2008; 8(3): 902–7.

4 Stoller MD, Park S, Zhu Y, An J. and Ruoff RS. Graphene-based ultracapacitors. *Nano Lett*. 2008; 8(10): 3498–3502.

5 Li SS, Tu KH, Lin CC, Chen CW and Chhowalla M. Solution-processable graphene oxide as an efficient hole transport layer in polymer solar cells. *ACS nano* 2010; *4*(6); 3169-3174.

6 Novoselov KS, Geim AK, Morozov SV, Jiang D, Zhang Y, Dubonos SV. and Firsov AA. Electric field effect in atomically thin carbon films. *Science* 2004; 306(5696): 666-669.

7 Schedin F, Geim AK, Morozov SV, Hill EW, Blake P, Katsnelson MI and Novoselov KS Detection of individual gas molecules adsorbed on graphene. *Nat. Mater.* 2007; 6(9): 652-655.

8 Vivekchand SRC, Rout CS, Subrahmanyam KS, Govindaraj A and Rao CNR. Graphene-based electrochemical supercapacitors. *J. Chem. Sci.* 2008; 120(1): 9-13.

9 Bae S, Kim H, Lee Y, Xu X, Park JS, Zheng Y and Iijima S. Roll-to-roll production of 30-inch graphene films for transparent electrodes. *Nat. Nanotechnol.* 2010; 5(8): 574-578.

10 Li X, Cai W, An J, Kim S, Nah J, Yang D and Ruoff R S. Large-area synthesis of high-quality and uniform graphene films on copper foils. *Science* 2009; 324(5932): 1312-1314.

11 Mattevi C, Kim H and Chhowalla M. A review of chemical vapor deposition of graphene on copper. *J. Mater. Chem.* 2011; 21(10): 3324-3334.

12 Li X, Magnuson CW, Venugopal A, An J, Suk JW, Han B, Borysiak M, et al. Graphene films with large domain size by a two-step chemical vapor deposition process. *Nano lett.* 2010; 10(11): 4328-4334.

13 Liu L, Zhou H, Cheng R, Chen Y, Lin YC, Qu Y, Bai J et. al. A systematic study of atmospheric pressure chemical vapor deposition growth of large-area monolayer graphene. *J. Mater. Chem.* 2012; 22(4): 1498-1503.

14 Bhaviripudi S, Jia X, Dresselhaus MS and Kong J. Role of kinetic factors in chemical vapor deposition synthesis of uniform large area graphene using copper catalyst. *Nano lett.*2010; 10(10): 4128-4133.

15 Kim H, Mattevi C, Calvo MR, Oberg JC, Artiglia L, Agnoli S, et al. Activation energy paths for graphene nucleation and growth on Cu. *ACS nano* 2012; 6(4): 3614-3623.

16 Blake P, Hill EW, Neto AC, Novoselov K S, Jiang D and Yang R. Making graphene visible. *App. Phy. Lett.* 2007; 91: 063124.

17 Ferrari AC, Meyer JC, Scardaci V, Casiraghi C, Lazzeri M, Mauri F, et al. Raman spectrum of graphene and graphene layers. *Phys. Rev. Lett* 2006; 97(18): 187401.

18 Reina A, Jia X, Ho J, Nezich D, Son H, Bulovic V, et al. Large area, few-layer graphene films on arbitrary substrates by chemical vapor deposition. *Nano lett.* 2008; 9(1): 30-35.

19 Wu B, Geng D, Guo Y, Huang L, Xue Y, Zheng J, et al. Equiangular Hexagon-Shape-Controlled Synthesis of Graphene on Copper Surface. *Adv. Mater.* 2011; 23(31); 3522-3525.

Chapter 6

Incorporation of small BN domains in graphene during CVD using methane, boric acid and nitrogen gas

6.1 Introduction

Since the discovery of atomically thick graphene in 2004 [1], it has been considered as one of the most promising candidate for future electronic devices due to its excellent electronic properties [2,3], and versatile application possibilities in transparent electronics [4 - 7] The absence of a band gap in graphene however limits its properties for application in electronic devices and reproducible practical procedures that open a band gap in graphene would widen its applicability. One way of achieving this is by doping [8]. Different methods to make doped graphene can introduce these modifications and tune the properties of graphene, to render graphene as a highly customizable material as has been achieved with carbon nanotubes [9]. Making graphene a hole conductor involves use of electron withdrawing dopants, whilst electron donating dopants are used to make it an electron conductor. Two types of graphene doping have been widely investigated, namely surface transfer doping [10] and chemical doping [11]. Doping has been achieved by the use of chemical species or an electric field [12]. The surface transfer doping methods have been used successfully to modify charge carriers in graphene but the shortcoming of the approach is that the doping is temporary and the doped graphene is difficult to integrate into functional devices. Permanent doping has been achieved in graphene by chemical doping using B for p-type graphene and N for n-type graphene [13]. A wide range of precursor materials have been reported to incorporate nitrogen or boron into graphene [14 - 17].

Several theoretical studies have shown that simultaneous incorporation of B and N in graphene is thermodynamically possible yielding small planar hexagonal boron nitride (*h*-BN) domains in graphene and most importantly that this process achieves

band gap modulation in graphene [18,19]. The band gap opening in graphene, due to doping with small BN domains, has been attributed to the breaking of localized symmetry [20]. The tunable electronic properties of graphene material containing BN makes this material likely to be useful in electronic devices, composites, energy conversion and storage [21]. Indeed, a CVD method has recently been used to grow BN doped graphene on a copper foil using Ar/H_2, methane and ammonia borane gases [22]. This method produced graphene domains alloyed with discrete large BN domains.

Here we demonstrate a facile, safe process for the chemical vapor deposition synthesis of BN doped graphene on copper using methane, boric acid powder and nitrogen gas. We show that that the B and the N are incorporated and that the N is bonded with the carbon within the graphene structure to make a continuous BN graphene material. Small units of BN in graphene, *i.e.* one B surrounded by three N and singly occurring hexagonal BN rings containing three B atoms and six N atoms are formed. Three of the N atoms in the hexagonal rings are also bonded to the carbon of the graphene. We provide a simple reproducible experimental method to synthesize large area graphene doped with small BN domains which can be used to make high quality BN doped graphene for possible applications in nanoelectronic devices.

6.2 Experimental Section

6.2.1 Materials

BN doped graphene was synthesized by a chemical vapor deposition (CVD) method. Copper foil (25 µm thick, Alpha Aesar) was used as the catalyst in this study [23]. A 1 cm × 2 cm copper foil was inserted into the centre of a cylindrical quartz tube reactor (22 cm × 100 cm). A copper envelope containing 300 mg boric acid powder was inserted into the quartz tube reactor 4 cm behind the copper foil as shown in Figure 6.1. The reactor was evacuated to 30 torr. A 7 % H_2 in N_2 (H_2/N_2) gas mixture (Air Gas, batch analyzed grade) was introduced into the reactor at 80 sccm whilst the vacuum was kept at 30 torr for a further 15 minutes. The reactor was then heated to 995 ^oC under vacuum. The reactor was held at 995 ^oC for a further 30 minutes after which methane gas (Air product, Ultrahigh purity) was also introduced at 20 sccm.

The methane flow was stopped after 20 minutes and the reactor was cooled under the H_2/N_2 gas at 80 sccm. Numerous experiments were conducted to optimize the separation between the boric acid container and the copper foil catalyst.

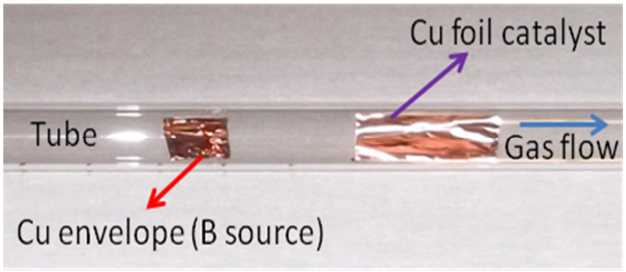

Figure 6.1 Cylindrical quartz tube reactor showing the inserted copper envelope containing boric acid (boron source) placed 4 cm before the flat copper foil catalyst used for graphene growth.

The 4 cm separation distance was found to be the optimal distance for quality graphene growth to take place in the presence of a boric acid source. Methane (20 sccm) and H_2/N_2 gas (80 sccm) without boric acid was also used to produce undoped graphene using the same procedure. The graphene was transfered onto a silicon substrate with a 300 nm silicon oxide layer (SiO_2/Si) as reported in ref [23]. In summary, 5 mm × 5 mm copper foil squares were cut from the 1 cm × 2 cm copper foil catalyst used and poly(methyl methacrylate) (PMMA) (Mico Chem) was spin coated onto the surface of the copper square on a spin coater (3000 rpm). The copper was then etched away from the doped graphene/PMMA layers (3 hours) in a 1M solution of $FeCl_3$ contained in a petri dish. After all the copper had been etched away, the graphene/PMMA was left floating in the $FeCl_3$ solution and was then washed several times in a 1M solution of HCl, followed by washing in water. Lastly the graphene/PMMA was attached to a cleaned SiO_2/Si substrate and was left to dry for 2 hours in air at ambient temperature. The PMMA was removed from the graphene by dissolving the PMMA in acetone. This was achieved by placing the PMMA/graphene on the SiO_2/Si in a petri dish containing acetone which was left standing for 15 minutes. The acetone was decanted and replaced by fresh acetone, and the process was repeated 3 times. Lastly the graphene was washed in methanol (to ensure complete removal of PMMA/acetone residues) and left to dry in air.

6.2.2 Characterization

The doped and undoped graphene samples were characterized on SiO_2/Si substrates unless otherwise stated. Optical images of the graphenes were recorded using an optical microscope. Surface morphology and graphene thickness characterization studies were conducted by tapping-mode atomic force microscopy (AFM) using a (DI) Dimension 3100 from Veeco. Morphological characterization of the BN doped graphene was carried out on graphene transferred onto plain copper grids using a Technai G^2 spirit TEM at 120 kV. Raman spectra were measured on an InVia Raman microscope (Reinshaw) at an excitation wavelength of 514 nm. X-ray photoelectron spectroscopy (XPS) measurements were perfomed with a Thermo Scientific K-Alpha spectrometer. All spectra were taken using an Al Kα microfocussed monochromatized source (1486.6 eV) with a resolution of 0.6 eV. The spot size was 400 μm and the operating pressure was 5×10^{-9} Pa.

6.3 Results and discussion

Figure 6.2a shows the optical image of the pristine graphene and Fig. 6.2b the optical image of BN doped graphene that was transferred onto SiO_2/Si substrates. The images of both the undoped and the BN doped graphene reveals a large area, uniform and continuous material. The pristine graphene in Fig. 6.2a has a light pink colour while the BN doped graphene (Figure 6.2b) is dark pink in colour. The colour contrast suggests that the BN doped graphene could be a single or double layer graphene. Figure 6.2c and d show TEM images of a continuous BN doped graphene material on a plain Cu grid. The small dark spots observed are due to residual Cu particles; the holes are due to imperfections in the graphene layer which develop during the transfer process. AFM imaging data revealed a continuous film of BN doped graphene with wrinkles (Figure 6.2e) which resulted from the transfer process of the graphene onto the SiO_2/Si substrate. The section analysis of the BN doped graphene shown in Figure 6.2e revealed a uniform material with a thickness of between 1.0-1.4 nm indicating that material was at most a double layer graphene [24]. In summary, both AFM and TEM analysis indicate that the BN doped graphene is uniform and large area (Figure 6. 2c-e).

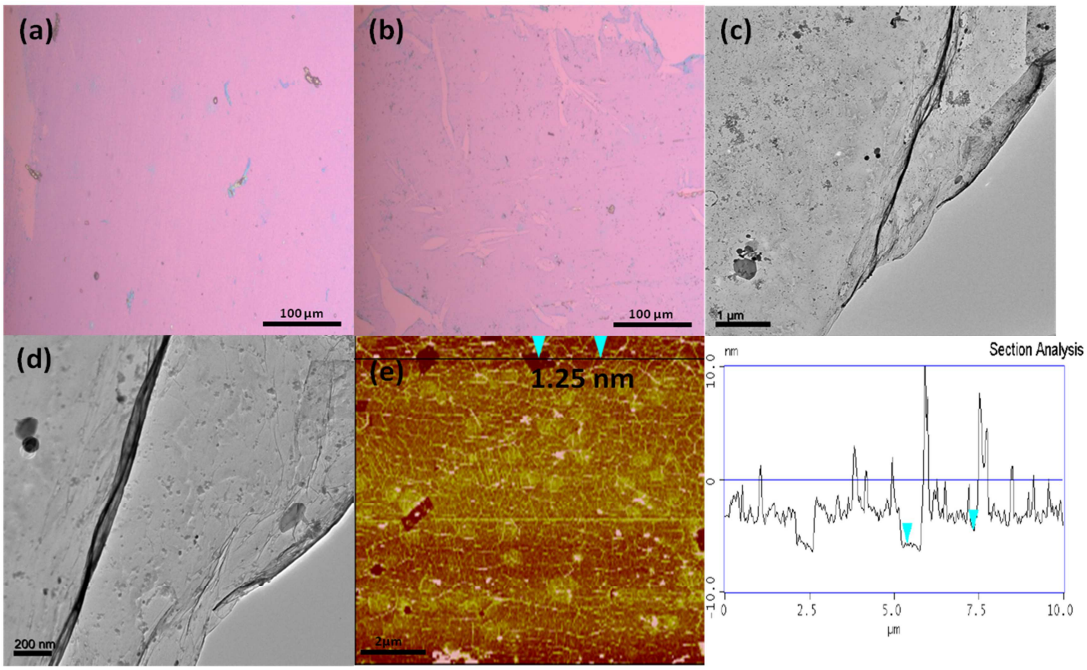

Figure 6.2 Graphene and BN doped graphene films grown on Cu using boric acid and nitrogen gas. (a) Optical images of pristine graphene transferred onto SiO_2/Si substrate. (b) Optical image of BN doped graphene transferred onto a SiO_2/Si substrate. (c) Low-magnification TEM image of BN doped graphene on a plain Cu TEM grid showing a continuous graphene film. (d) High-magnification TEM image of BN doped graphene on a plain Cu grid showing small particles of Cu and Fe remaining after the etching process. (e) AFM image of BN doped graphene showing wrinkled graphene, and (f) AFM section analysis of BN graphene showing an average film thickness of 1.25 nm.

Raman spectra of pristine and BN doped graphene were taken from five different regions of both the doped and undoped graphene samples. Fig. 6.3 compares the Raman spectra of one measurement from both the pristine and BN doped graphene. The Raman spectrum of pristine CVD graphene shows three peaks (1347, 1585 and at 2686 cm^{-1}) representing the D, G and the 2D bands, respectively (Table 6.1) [25]. Compared to the G and the 2D bands the D band has a very small intensity showing that the graphene is of high quality [25]. The ratio between the intensity of the G to the 2D band (I_G/I_{2D}) is ca. 0.3 which suggests that the graphene has properties similar to that of a single layer graphene [24]. The Raman spectrum of the BN doped graphene also showed three peaks (1341, 1589 and 2690 cm^{-1}) again representing the D, G and the 2D bands respectively (Table 6.1).

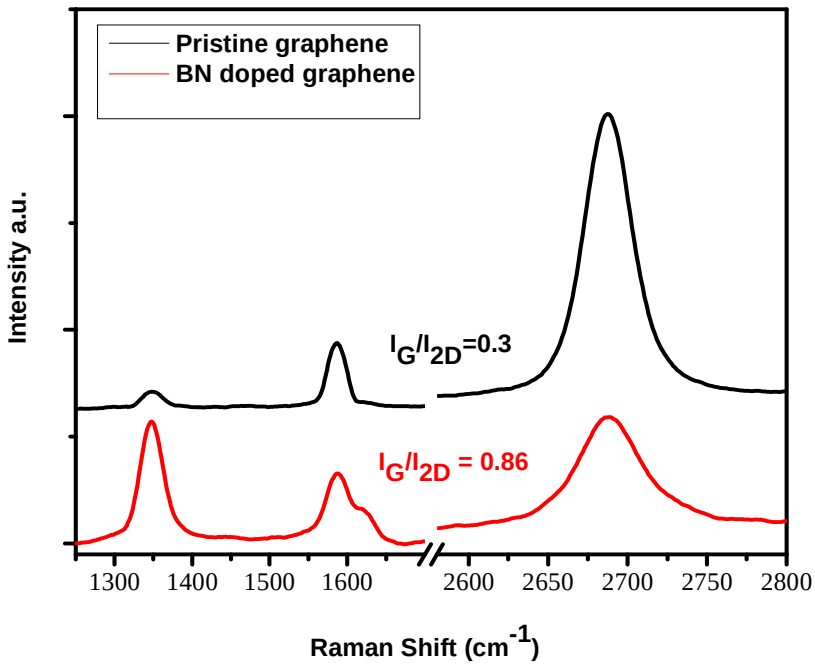

Figure 6.3 Raman spectra of pristine graphene and BN doped graphene synthesized using the CVD method on copper.

The slight upshift of the G and 2D peaks of the doped graphene is associated with chemical doping into the graphene structure [26]. The D band of the doped graphene showed a slight downshift. The doping is further corroborated by a shoulder on the G peak, also known as the D^* peak, observed at 1623 cm^{-1}. This split in the G peak of graphene has been reported previously by several authors and has been attributed to localized symmetry breaking in graphene [27 - 29], as found in BN doped graphene [22]. The I_G/I_{2D} ratio of the BN doped graphene is 0.86, and the intensity of the 2D band is diminished in the BN doped graphene.

Table 6.1 Raman peak positions of pristine graphene and BN doped graphene synthesized the CVD method on copper.

Raman Shift	D (cm^{-1})	G (cm^{-1})	D^* (cm^{-1})	2D (cm^{-1})
Pristine Graphene	1347	1585	-	2686
BN Graphene	1341	1589	1623	2690

XPS data were recorded on the pristine and BN doped graphene. All spectra were taken using an Al Kα microfocussed monochromatized source (1486.6 eV) with a resolution of 0.6 eV. The spot size was 400 μm and the operating pressure was 5 x 10^{-9} Pa. XPS data for pristine graphene revealed the presence of C and a small amount of O (not shown). The doped graphene by contrast showed peaks in the 400, 190 and 284 eV regions that correspond to N, B and C atoms, respectively (Fig.6.4). The atomic percentage of C, N and B in the sample was 98.0 %, 1.38 % and 0.62 % respectively. The atomic percentage of the N and B dopants could be increased, but this was accompanied by an increase in the oxygen content and poor quality of the BN doped graphene that was produced.

Fig. 6.4a shows the N1s spectrum of BN doped graphene and reveals only a single peak at 399.8 eV. Since pure hexagonal boron nitride (*h*-BN) [30], and BN doped graphene with discrete domains of BN alloyed with graphene [22] give peaks at 398.1 eV, these types of structures can be ruled out in this new material. The peak at 399.8 eV is close to, but different from, the reported XPS peak energy of ~ 401 eV for graphitic/quaternary N in graphene [31]. The N1s peak position lies more to the high binding energy of a C-N bond. This suggests that there are more C-N bonds around a single N compared to B-N bonds. This is possible in a case where N is bonded to one B atom and two C atoms. This data suggest that the BN is not in the form of discrete domains (Fig. 6.6c) but is part of the extended graphene structure in the form of small BN domains shown in Fig. 6.6a and b [20].

The B1s profile shown in Fig. 6.4b suggests that several B species are present and incorporated within the doped graphene product. The three peaks at ca. 191.0, 188.7 and 186.7 eV having different intensities indicate three B containing species with different concentrations. The large B1s peak at 191.0 eV can be associated with a boron atom linked to a nitrogen atom (BN structure) [32,33]. This is consistent with BN incorporation into graphene. The two boron species in lower concentrations, compared to the B in the BN, could correspond to BC_3 at 188.7 eV [34,35] and to B_4C at 186.7 eV [36] suggesting that C-B bonds are also present in the new material. However B-C bonds are very few meaning that, under the reaction conditions we

have in this case, (methane, boric acid and nitrogen gas) B-N formation is more favourable than B-C formation.

The C1s spectrum of the BN doped graphene (Fig. 6.4c) shows five peaks after deconvolution. The peak at 284.0 eV corresponds to sp^2 hybridized carbon (graphitic carbon) from the undoped region of the graphene material [37]. The peak at 285.1eV can be associated with sp^2 hybridized carbon bonded to nitrogen [38] and to carbon with defects [39]. The two peaks associated with sp^2 hybridized carbon bonded to nitrogen and to carbon with defects overlap at 285.1 eV to form one peak. The peak at 285.1 eV likely arises from graphene domain edges and defects. The smaller peak at lower binding energy (282.5 eV) can be associated with B-C bond formation. The higher binding energy peaks at ca 286.6 and 289.1 eV are attributed to the formation of C-O bonds [40].

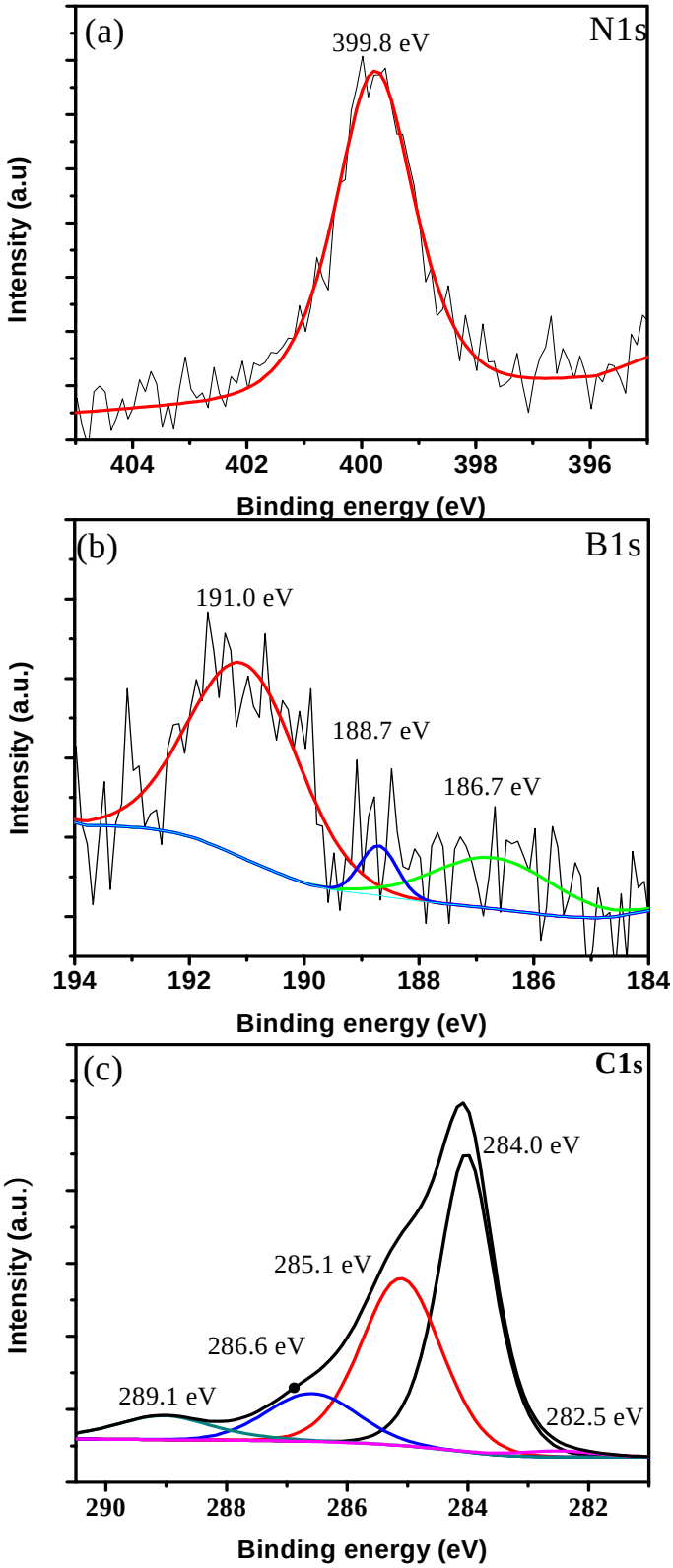

Figure 6.4 XPS spectra showing the (a) N1s, (b) B1s, and (c) C1s core levels obtained from BN doped graphene.

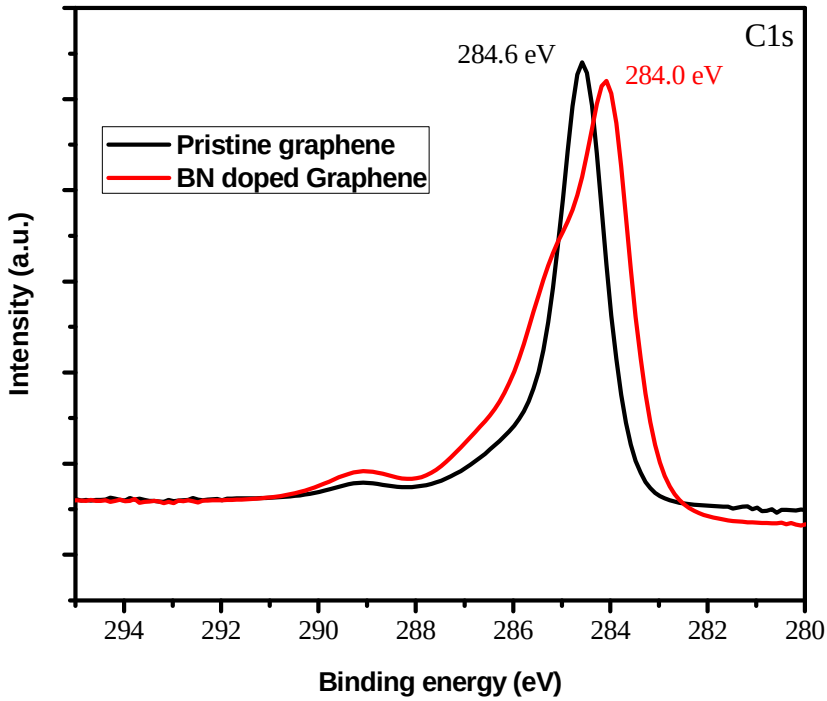

Figure 6.5 C1s core level spectra of pristine graphene and BN doped graphene.

Fig. 6.5 compares the C1s spectra of the pristine graphene with that of BN doped graphene. The C1s spectrum of pristine graphene has a more symmetrical shape and is very sharp when compared to the C1s spectra of the doped graphene. XPS analysis showed a downshift of 0.6 eV and broadening of the C1s peak after doping with BN. The downshift in the C1s peak in the doped material suggests that the material is a p-type semiconductor as was observed in doped p-type semiconducting carbon nanotubes [41]. Experimental studies have shown that carbon films doped with both B and N exhibit p-type semiconducting behavior [42]. Ambipolar semiconducting behavior was reported in an *h*-BNC material which contained discrete domains of graphene and *h*-BN [21]. Analysis of the atomic composition of B and N atoms in our BN doped graphene showed that the B/N ratio was between 0.5-0.3, i.e., N was in excess in the graphene. This is possible because the N source in this reaction was nitrogen gas and this was in excess compared to the B from boric acid.

Fig. 6.6 shows three possible types of BN structures in the graphene matrix. Fig. 6.6a shows a BN species with a B/N ratio of 0.33 with Fig. 6.6b showing an *h*-BN structure with B/N ratio of 0.5. The B/N ratio expected for Fig. 6.6c, which shows larger BN domains is close to 1. The data hence suggest that small BN domains have been incorporated within the graphene matrix but not in large discrete BN domains.

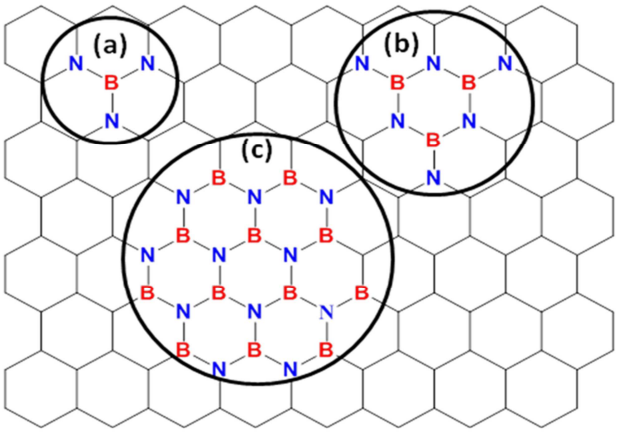

Figure 6.6 Atomic model of the possible BN species incorporated in BN doped graphene (a) BN with N bonded to 2 carbon atoms, (b) *h*-BN with the N bonded to one or two carbon atoms and (c) *h*-BN domains in graphene matrix.

We propose a mechanism for the formation of small BN domains within the extended graphene structure. Upon heating, H_3BO_3 in the copper container melts (171 ^oC) and volatilizes above 300 ^oC. The N_2 carrier gas carries the H_3BO_3 to the copper foil (catalyst). Here the H_3BO_3 decomposes to form B_2O_3. Addition of CH_4 at 995 ^oC results in the formation of reactive carbon species (equation 1) [43] Reaction of C with B_2O_3 on the copper catalyst surface generates B-C species. However in the presence of N_2, the B-C species are stabilized and form BN species in the graphene matrix (equation 2). The two reactions shown in equations (*1*) and (*2*) take place on the copper surface. Reaction (*2*) is initiated by reaction (*1*). A similar mechanism has been used to explain the synthesis of BN doped single walled carbon nanotubes [44]. Formation of BN in a graphene oxide material using graphene oxide material and B_2O_3 required a temperature of 1500 ^oC [33]. In our case the reaction took place at 995 ^oC using the inert N source, N_2 gas. The reaction can also be performed at low

temperatures < 1000 ^{o}C if the more reactive NH_3 replaces the inert N_2 [43,45].

$$CH_4(g) + H_2(g) \rightarrow C(s) + H_2(g) \qquad (1)$$

$$B_2O_3(s) + 3C(s) + N_2(g) \rightarrow BN(s) + 3CO(g) \qquad (2)$$

6.4 Conclusions

In summary, we have synthesized large area graphene incorporating small BN species by a facile and safe process avoiding the use of boranes and ammonia. Raman analysis reveals formation of monolayer or (few layer) BN doped graphene. XPS revealed that several B bonding species were incorporated into graphene with the main product being the small BN domains. The N of the BN is bonded to carbon forming B-N-C systems, showing that we managed to grow continuous BN containing graphene in which BN species were incorporated in the graphene structure. This remarkable finding has led us to synthesize large area graphene incorporating small BN domains. The method is a simple one. Raman data revealed an additional D* band in the BN doped graphene that confirmed possible band gap opening by graphene symmetry breaking. The results presented here are highly relevant to the application of graphene in nano-optoelectronic devices.

References

1 Novoselov KS, Geim AK, Morozov SV, Jiang D, Zhang Y, Dubonos SV, Grigorieva AA. Electric field effect in atomically thin carbon films. *Science*, 2004, **306**, 666–669.

2 Castro Neto AH, Guinea F, Peres NMR, Novoselov KS and Geim AK. The electronic properties of graphene. *Rev. Mod. Phys.*, 2009, **81**, 109-162.

3 Stamfer C, Fringes S, Guttinger J, Molitor F, Volk C, Terres B, Dauber J, Engels S, Schnez S, Jacobsen A, Droscher S, Ihn T and Ensslin K. Transport in graphene nanostructures. *Front. Phys.*, 2011, **6**, 271-293.

4 Ghosh S, Calizo I, Teweldebrhan D, Pokatilov EP, Nika DL, Balandin AA, Bao W, Miao F and Lau CN. Extremely high thermal conductivity of graphene: Prospects for thermal management applications in nanoelectronic circuits. *Appl. Phys. Lett.*, 2008, **92**, 151911.

5 Zhu Y, Murali S, Cai W, Li X, Suk JW, Potts JR and Ruoff RS. Graphene and Graphene Oxide: Synthesis, Properties, and Applications. *Adv. Mater.*, 2010, **22**, 3906–3924.

6 Li SS, Tu KH, Lin CC, Chen CW and Chhowalla M. Solution-Processable Graphene Oxide as an Efficient Hole Transport Layer in Polymer Solar Cells. *ACS Nano*, 2010, **4**, 3169–3174.

7 Wang X, Zhi L and Müellen K. Transparent, Conductive Graphene Electrodes for Dye-Sensitized Solar Cells. *Nano Lett*., 2008, **8**, 323-327.

8 Liu H, Liu Y and Zhu DJ. Chemical doping of graphene. *Mater. Chem*.,2011, **21**, 3335-3345.

9 Schnorr JM and Swager TM. Emerging Applications of Carbon Nanotubes. *Chem. Mater*. 2011, **23**, 646–657.

10 Chen W, Chen S, Qi DC, Gao XY and Wee ATS. Surface Transfer p-Type Doping of Epitaxial Graphene. *J. Am. Chem. Soc.*, 2007, **129**, 10418-10422.

11 Miao H, Tongay, MK Petterson, Berke K, Rinzler AG, Appleton BR and Hebard AF. High Efficiency Graphene Solar Cells by Chemical Doping. *Nano Lett*, 2012, **12**, 2745−2750.

12 Mak KF, Lui CH, Shan J and Heinz TF. Observation of an Electric-Field-Induced Band Gap in Bilayer Graphene by Infrared Spectroscopy. *Phys. Rev. Lett.*, 2009, **102**, 256405.

13 Panchakarla LS, Subrahmanyam KS, Saha SK, Govindaraj A, Krishnamurthy HR, Waghmare UV and Rao CNR. Synthesis, Structure, and Properties of Boron and Nitrogen-Doped Graphene. *Adv. Mater*., 2009, **21**, 4726–4730.

14 Zhang C, Fu L, Liu N, Liu M, Wang Y and Liu Z. Synthesis of Nitrogen-Doped Graphene Using Embedded Carbon and Nitrogen Sources. *Adv. Mater.*, 2011, **23**, 1020–1024.

15 Wang Y, Shao Y, Matson DW, Li J and Lin Y. Nitrogen-Doped Graphene and Its Application in Electrochemical Biosensing. *ACS Nano*, 2010, **4**, 1790-1798.

16 Sheng ZH, Gao HL, Bao WJ, Wang FB and Xia WH. Synthesis of boron doped graphene for oxygen reduction reaction in fuel cells. *J. Mater. Chem.*, 2012, **22**, 390-395.

17 Suzuki S and Hibino H. Chemical vapor deposition of boron- and nitrogen-containing graphene thin films. *Mat. Sci. Eng. B.*, 2012, **177**, 233-238.

18 Shinde PP and Kumar V. Direct band gap opening in graphene by BN doping: *Ab initio* calculations. *Phys. Rev. B.*, 2011, **84**, 125401.

19 Xu B, Lu YH, Feng YP and Lin JY. Density functional theory study of BN-doped graphene superlattice: Role of geometrical shape and size. *J. Appl. Phys.* 2010, **108,** 073711-073717.

20 Fan X, Shen Z, Liu QA and Kuo J. Band gap opening of graphene by doping small boron nitride domains. *Nanoscale,* 2012**, 4**, 2157-2165.

21 Lin Y and Connell JW. Advances in 2D boron nitride nanostructures: nanosheets, nanoribbons, nanomeshes, and hybrids with graphene. *Nanoscale,* 2012, **4**, 6908-6939.

22 Ci L, Song L, Jin C, Jariwala D, Wu D, Li Y, Srivastava A, Wang ZF, Storr K, Balicas K, Liu F and Ajayan PM. Atomic layers of hybridized boron nitride and graphene domains. *Nature Mater.* 2010, **9**. 430-435.

23 Li X, Cai W, An J, Kim S, Nah J, Yang D, Piner R, Velamakanni A, Jung I, Tutuc E, Banerjee SK, Colombo L and Ruoff RS. Large-Area Synthesis of High-Quality and Uniform Graphene Films on Copper Foils. *Science,* 2009, **324,** 1312-1314.

24 Mattevi C, Kim H and Chhowalla M. A review of chemical vapour deposition of graphene on copper. *J. Mater. Chem*., 2011, **21**, 3324–3334.

25 Ferrari AC, Meyer JC, Scardaci V, Casiraghi C, Lazzeri M, Mauri F, Piscanec S, Jiang D, Novoselov KS, Roth S and Geim AK. Raman Spectrum of Graphene and Graphene Layers. *Phys. Rev. Lett.,* 2006, **97**, 187401.

26 Casiraghi C, Pisana S, Novoselov KS, Geim AK and Ferrari AC. Raman fingerprint of charged impurities in graphene. *App. Phys. Lett.*, 2007, **91**, 233108.

27 Dong X, Shi Y, Zhao Y, Chen D, Ye J, Yao Y, Gao F, Ni Z, Yu T, Shen Z, Huang Y, Chen P and Li L. Symmetry Breaking of Graphene Monolayers by Molecular Decoration. *Phys. Rev. Lett.,* 2009, **102**, 135501.

28 Yang R, Huang QS, Chen X, Zhang GY and Gao HJ. Substrate doping effects on Raman spectrum of epitaxial graphene on SiC. *J. App. Phys.,* 2010, **107**, 034305.

29 Lee J, Novoselov KS and Shin HS. Interaction between Metal and Graphene: Dependence on the Layer Number of Graphene. *ACS Nano*, 2011, **5**, 608–612.

30 Guimon C, Gonbeau D, Pfister-Guillouzo G, Dugne O, Guette A, Naslain R and Lahaye M. XPS Study of BN Thin Films Deposited by CVD on SiC Plane Substrates. *Surf. Interface Anal.*, 1990, **16**, 440-445.

31 Hwang JO, Park JS, Choi DS, Kim JY, Lee SH, Lee KE, Kim YH, Song M, Yoo S and Kim SO. Workfunction-Tunable, N-Doped Reduced Graphene Transparent Electrodes for High-Performance Polymer Light-Emitting Diodes. *ACS Nano,* 2012, **6**, 159-167.

32 Park KS, Lee DY, Kim KJ and Moon DW. Observation of a hexagonal BN surface layer on the cubic BN film grown by dual ion beam sputter deposition. *Appl. Phys. Lett.*, 1997, **70**, 315-.

33 Lin TW, Su CV, Zhang XQ, Zhang W, Lee YH, Chu CW, Lin HY, Chang MT, Chen FR, and Li LJ. Converting graphene oxide monolayers into boron carbonitride nanosheets by substitutional doping. *Small,* 2011, **8,** 1384–1391.

34 Cermignani W, Paulson TE, Onneby C, and Pantano CG. Synthesis and characterization of boron-doped carbons. *Carbon,* 1995, **33**, 367–374.

35 Jacobsohn LG, Schulze RK, Maia da Costa MEH and Nastasi M. X-ray photoelectron spectroscopy investigation of boron carbide films deposited by sputtering. *Surf. Sci.*, 2004, **572**, 418-424.

36 Il'inchik EA, Volkov VV and Mazalov LN. X-Ray photoelectron spectroscopy of boron compounds. *J. Struct. Chem.* (Transl. Zh. Strukt. Khim.) 2005, **46**, 523–534.

37 Moreau E, Ferrer FJ, Vignaud D, Godey S and Wallart S. Graphene growth by molecular beam epitaxy using a solid carbon source. *Phys. Status Solidi A.*, 2010, **207**, 300-303.

38 Shao Y, Zhang S, Engelhard MH, Li G, Shao G, Wang Y, Liu J, Aksayc IA and Lin Y. Nitrogen-doped graphene and its electrochemical applications. *J. Mater. Chem*., 2010, **20**, 7491–7496.

39 Luo Z, Shang JZ, Lim SH, Li DH, Xiong QH, Shen ZX, Lin JY and Yu. H. Modulating the electronic structures of graphene by controllable hydrogenation. *Appl. Phys. Lett.*, 2010, **97**, 233111.

40 Morant C, Prieto PJ, Bareño J, Sanz JM and Elizalde E. Hard BCxNy thin films grown by dual ion beam sputtering. *Thin Solid Films*, 2006, **515**, 207-211.

41 Geng HZ, Kim KK, Song C, Xuyen NT, Kim SM, Park KA, et al. Doping and de-doping of carbon nanotube transparent conducting films by dispersant and chemical treatment. *J. Mater. Chem.*, 2008, **18**, 1261-1266.

42 Watanabe MO, Itoh S, Mizushima K and Sasaki T. Electrical properties of BC_2N thin films prepared by chemical vapor deposition. *J. Appl. Phys.*, 1995, **78**, 2880.

43 Ammendola P, Chirone R, Lisi L, Ruoppolo G and Russo G. Copper catalysts for H_2 production via CH4 decomposition. *J Mol. Catal. A-Chem*., 2007, **266**, 31-39.

44 Wanga W, Bia JQ, Suna WX, Zhua HL, Xua JJ, Zhaoa MT, Bai YJ. Facile synthesis of boron nitride coating on carbon nanotubes. *Mater. Chem. Phys.*, 2010, **122**, 129-132.

45 Thomas J, Weston NE and O'Connor TE. Turbostratic Boron Nitride, Thermal Transformation to Ordered-layer-lattice Boron Nitride. *J. AM. Chem. Soc.*, 1962, **84**, 4619-4622.

Chapter 7

Enhanced current collection using an N-CNT modified ITO electrode in a P3HT:PCBM solar cell

7.1 Introduction

Polymer based photovoltaic devices can be made using a coating process such as spin coating or inkjet printing, hence they are an attractive option for the inexpensive covering of large areas of flexible plastic surfaces. Poly (3-hexylthiophene) (P3HT) and 6,6-phenyl-C61 butyric acid methyl ester (PCBM) are the most commonly studied materials used in organic photovoltaic systems (OPVs) [1]. The incident photon-to-current efficiency (IPCE) in OPVs decreases with increase in light and this effect amplifies with area and sheet resistance of the indium doped tin oxide (ITO) electrode [2]. OPVs are more efficient when operating at low light intensities than at high light intensities. This means that most light is wasted at high light intensities. The resistive ITO contact causes a non-negligible voltage drop across the cell area, which in turn limits the photocurrent and gives a considerable decrease in the cell short circuit current density and fill factor (FF) [3]. The losses in IPCE increase with device area, and are a hindrance to up scaling. Substitution of ITO with a grid like metal electrode has been used to efficiently collect current and minimize the IPCE losses with increasing light intensity [4]. The use of carbon nanotubes (CNTs), a one dimensional material made from carbon, also holds promise to achieve this same end. This is because they are ballistic conductors [5], flexible and optically transparent [6]. CNTs can be made into thin film electrodes to replace the ITO electrode and this could make OPV fabrication completely solution prossesable offering a low cost alternative to the use of ITO [7]. The morphology of CNT films makes it an interpenetrating nanostructured electrode which is useful for efficient carrier injection/extraction at the active layer-electrode junction. CNTs could act as

acceptors and improve charge transport in the poly(3-hexyl)thiophene active layer. Many studies on incorporating carbon nanotubes in OPVs have been reported; however, in these studies the performance of carbon nanotube devices generally remains lower than that of their fullerene counterparts [8]. Although carbon nanotubes are only a few nanometers in diameter, they can be up to millimeters in length [9]. This is much larger than the thickness of an optimum active layer thickness in OPVs which should be restricted to a thickness less than 100 nm thick for optimum performance [10].

An OPV device constructed with MWCNTs deposited on top of ITO produced a device with an enhanced short circuit current density compared to a device fabricated on plain ITO [11]. The enhanced short circuit current is attributed to efficient charge collection by the MWCNT network. We studied OPVs with the same structure and we observed the same trend and further analysis also showed that IPCE losses with increase in light intensity were minimized. To the best of our knowledge this is the first time carbon nanotubes have been used to minimize the IPCE losses that are known to occur with increasing light intensities in OPVs. Here we report on our results showing that by placing an additional thin film of N-CNTs on top of ITO we have managed to minimize the IPCE losses of OPVs at high light intensities.

7.2 Experimental

7.2.1 Film Preparation

The N-CNT films transferred onto ITO substrates were prepared using the vacuum filtration and stamping methods discussed in chapter 4. N-CNT films of different thicknesses were fabricated by varying the amount of filtered material deposited on a nitro cellulose mixed ester membrane. In summary 5 mL, 10 mL, 15 mL, 20 mL of the suspension was vacuum filtered through a 220 nm pore size, mixed cellulose ester membrane (Millipore), followed by washing of the membrane with copious quantities of deionized water to remove the surfactant. The films were transferred onto silicon substrates (Si) and on glass substrates for characterization. For characterization 5 mm x 5 mm films were used. The 5 mm x 5 mm film was cut out from the circular

membrane. To transfer the N-CNT film onto a Si substrate, a wet 5 mm x 5mm membrane was placed on to the Si substrate, with N-CNT side facing down. The assembly containing the filtered material was subsequently covered with clean porous paper and loaded with a 2 kg mass and allowed to dry for 3 hours at 80 ^{o}C on a hotplate. The N-CNT film (with the filtration membrane still attached) adhered to the different Si substrates. The mixed cellulose ester membrane was removed by dissolving polymer in 3 successive acetone baths followed by a final methanol bath and lastly in deionized water. The N-CNT films on Si were left to dry in air. The N-CNT films were heated at 400 ^{o}C for two hours under a 7% H_2 in N_2 gas mixture (N_2/H_2) atmosphere. The same transfer method was used to transfer films with different thicknesses on to glass and ITO coated glass substrates. The N-CNT films were characterized by scanning electron microscopy FE-SEM, JEOL, JSM-600F, 10 kV and by UV-Vis spectroscopy PerkinElmer Lambda 25 UV-vis spectrometer.

7.2.2 Device fabrication

Photovoltaic devices were fabricated on clean patterned ITO coated glass substrates. N-CNT films were transferred on to patterned ITO glass using the method described above. Four types of OPV devices were made in this work. In the different devices PEDOT:PSS was spincoated on; (1) ITO, (2) 5 mL N-CNT film on ITO, (3) 10 mL N-CNT film on ITO, (4) 15 mL N-CNT film on ITO and (5) 20 mL N-CNT film on ITO. A 20 mg/mL active layer solution was prepared by dissolving P3HT and PCBM in chloroform followed by stirring for 3 hours on a magnetic stirrer (500 rpm). The solution was spincoated on the 5 prepared hole collecting electrodes using a spincoater (2000 rpm). The devices were annealed on a hotplate at 110 ^{o}C for 10 minutes. The Al top electrodes were deposited by thermal evaporation in vacuum. The devices made in this work were of the structure shown in Figure 7.1. I-V characteristics were obtained under solar simulated AM 1.5 spectrum white light of different intensities at room temperature using an HP 4141 source measure unit.

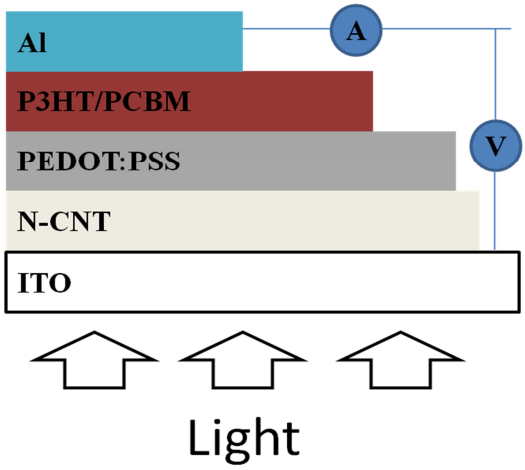

Figure 7.1 The schematics of the OPV device containing an interpenetrating nanostructured electrode made with an N-CNT layer on an ITO electrode.

7.3 Results and discussion

Figure 7.2a shows an optical image of a 20 mL N-CNT film deposited on to a PET substrate. The image shows that the N-CNT films are large area and transparent. The films can be made as large as needed. Large area uniform films can thus be produced using this technique. Figure 7.2(b-d) shows SEM images of three different samples (a), (b) and (c) that were prepared by filtering a volume of 5 mL, 10 mL and 15 mL of N-CNT dispersion, respectively, through a nitro cellulose mixed ester membrane. Several features are to be noted in these images. First, in these networks, each long thin object is a single N-CNT on the substrate surface and not bundles of single walled carbon nanotubes.[12] Also from the images, thickness and coverage of the films can be varied by using different filtration volumes. Thin films can be obtained from small volumes and thicker films from larger volumes. We measured the transmittance of the thin films at λ = 550 nm. The transmittance decreased as the filtration volume increases (Figure 7.3). This filtration method has several advantages; (1) the homogeneity of the films is regulated by the process itself. Thus, if a certain area becomes too thick during filtration, permeation is reduced in that area and this allows the thin areas to grow in thickness. (2) The film thickness can be precisely regulated by the nanotube concentration and volume of the filtered suspension.

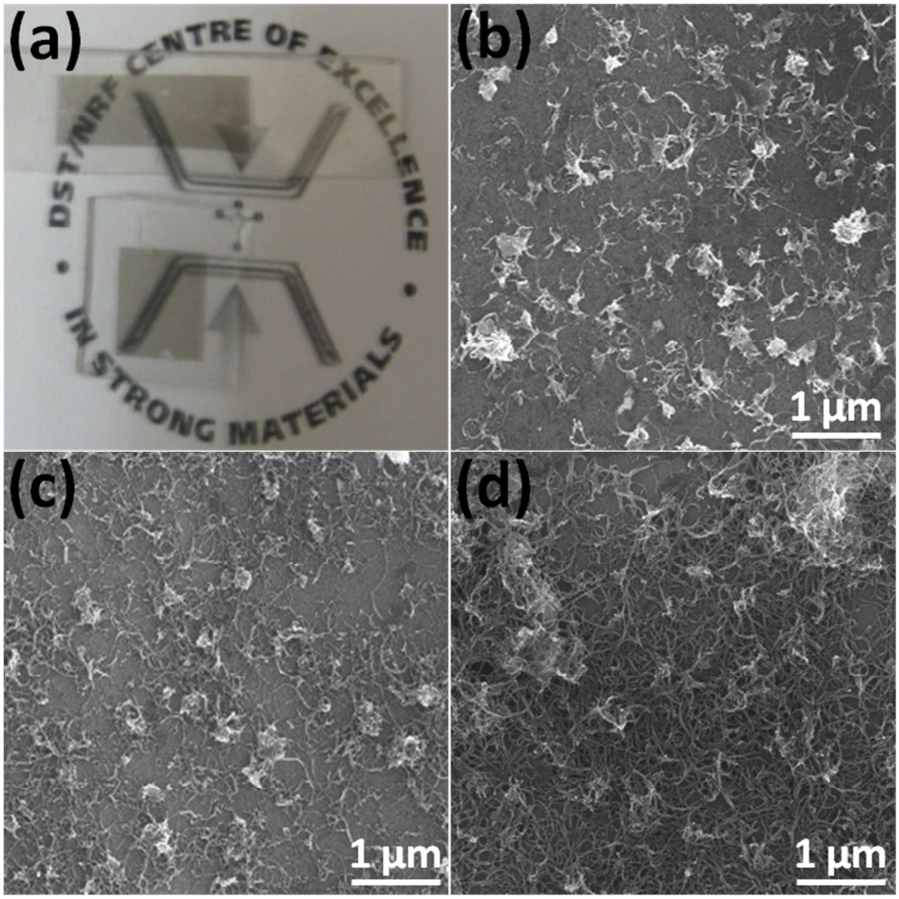

Figure 7.2 Transparent N-CNT films; (a) transparent film on a PET substrate and SEM images made from filtering (b) 5 mL, (c) 10 mL and (d) 15 mL of dispersion.

From the transmittance measurements we see that the film made using a 20 ml volume is only 50 % transparent making it unsuitable for use in a transparent electrode materials in OPVs. We decided to use films made from 15 mL, 10 mL and 5 mL with transmittances of 64, 71 and 85%, respectively, relative to the ITO coated glass substrate.

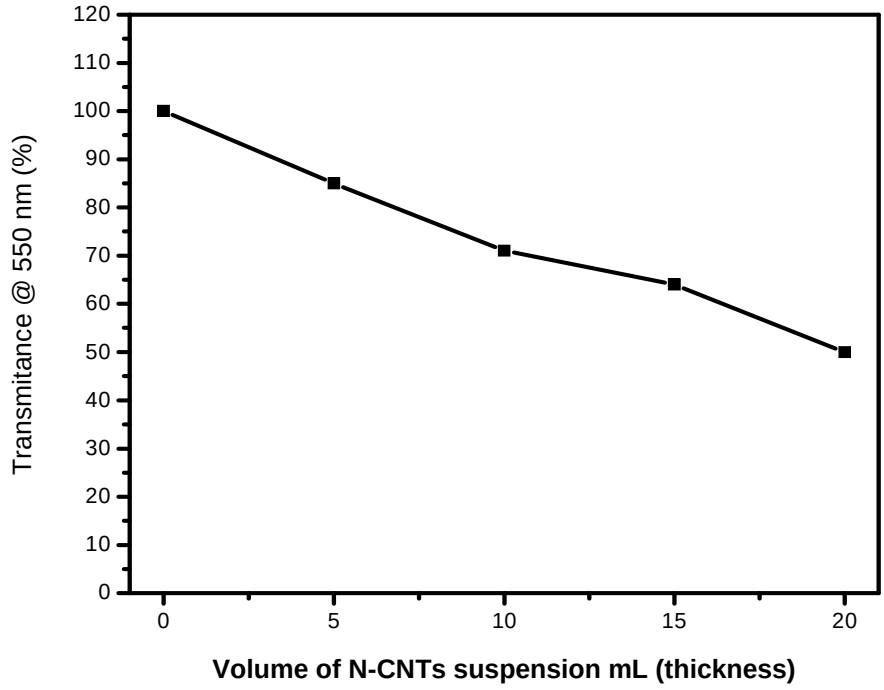

Figure 7.3 Transmittance at 550 nm of different films made from filtering different volumes of dispersion on the mixed ester cellulose membrane.

Figure 7.4 and Table 7.1 show the J-V characteristics of the devices made in this work. The OPV fabricated directly on ITO only gave a V_{oc} of 0.51 V and a J_{sc} of 3.89 mA/cm^2 under illumination with a 100 mW/cm^2 light. The ITO modified with an N-CNT film made by filtering a 5 mL dispersion showed a dramatic J_{sc} enhancement (4.87 mA/cm^2) but the V_{oc} (0.50) remained unchanged. A further increase in the thickness of the N-CNT film on ITO had a detrimental effect on the J_{sc} of the devices as indicated by J_{sc} values of 2.90 and 2.51 mA/cm^2, for the 10 mL and 15 mL films respectively. The open circuit voltage was not affected significantly by the use of N-CNT films on the ITO electrode. The N-CNT films have low transmittances which contribute to the low device yields. Shorting in the devices containing the thicker films made from the (10 mL and 15 mLN-CNT films) occurs since the films are more than 100 nm thick.[13]

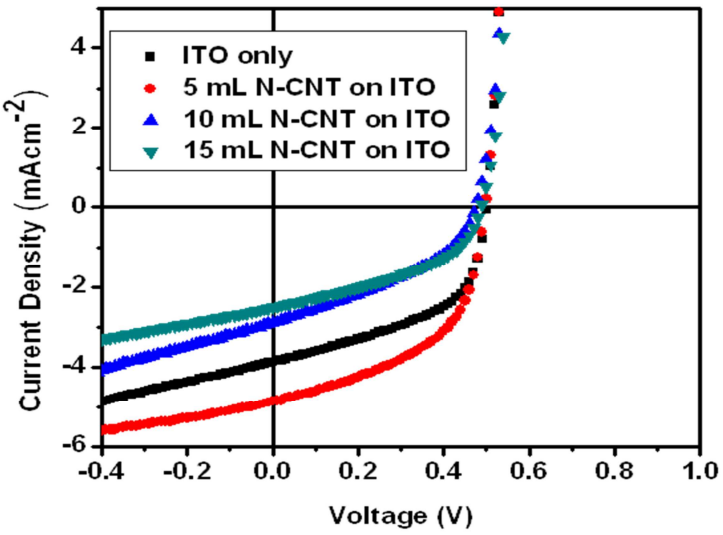

Figure 7.4 Comparison of the I–V curves for OPVs with ITO only, 5mL N-CNT on ITO, 10 mL N-CNT on ITO and 15 mL N-CNT on ITO illuminated under a 100 mW/cm^2 light.

The improvement in J_{sc} can be related to efficient harvesting of the generated excitons. The 5 mL N-CNT film showed a transmittance of 80 %, this means that if the current density is normalized this device would show an even better J_{sc} when compared to the bare ITO device.

Figure 7.5 compares the J_{sc}, V_{oc}, FF and IPCE measured under light of different intensities on the 4 different devices made in this work. Light dependence measurements can establish if the resulting current enhancement in a device is a result of efficient current collection at the electrodes or from some other effect. The open circuit voltage of all the devices increased with illumination (Figure 7.5a). J_{sc} of all the devices increased with illumination (Figure 7.5b). The increase in J_{sc} with illumination is almost linear in the device with N-CNT films deposited on the ITO electrode. This suggests efficient current collection on the N-CNT modified ITO electrodes.[14] The fill factor of the devices generally increased with illumination. The FF peak maxima occurred at 50 mW/cm^2 illumination for the ITO only device and the 5 mL N-CNT modified ITO device. The FF increased continuously in the devices with thicker N-CNT films (10 mL and 15 mL), the maximum FF occurs at maximum

illumination (100 mW/cm^2). This is related to the shading effect of the N-CNT films on the OPVs.

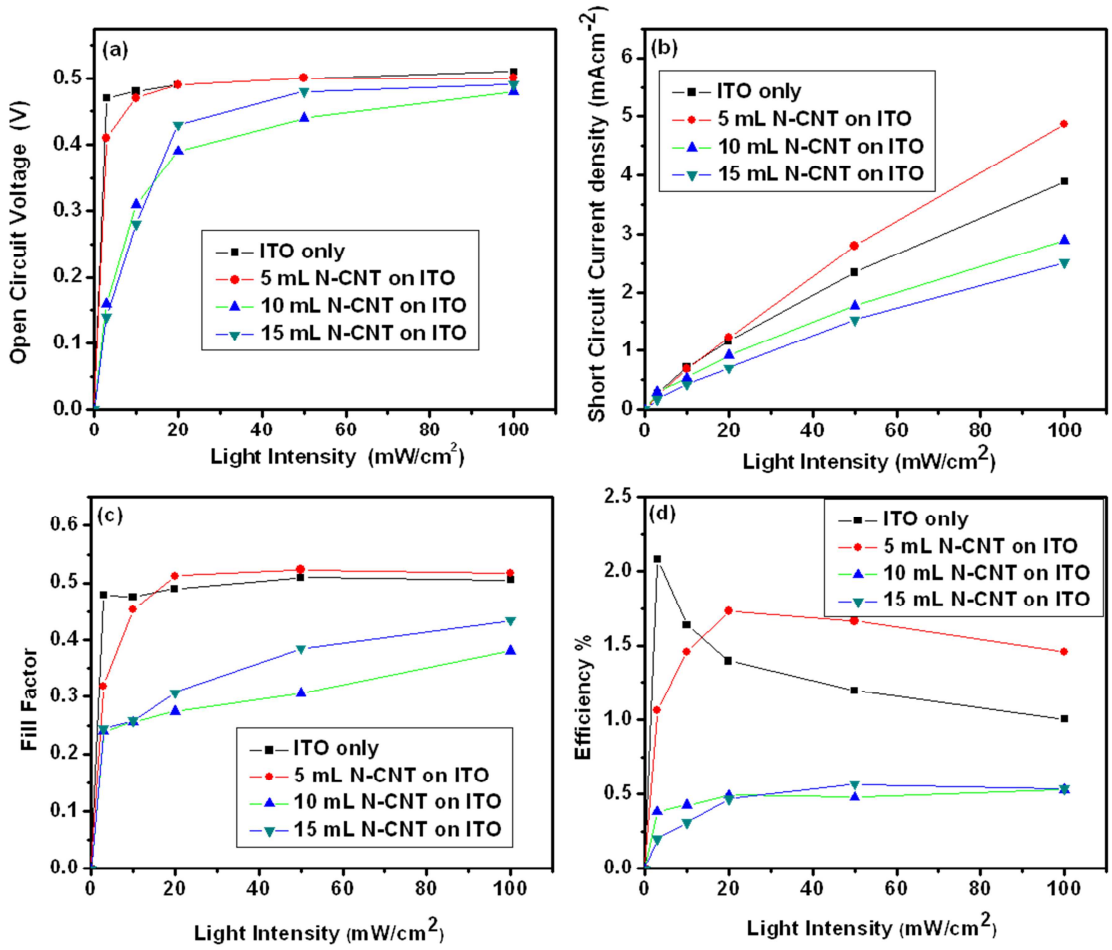

Figure 7.5 Comparisons between PV performances for the four different devices (a) V_{oc} (b) J_{sc}, (c) FF, and (d) IPCE.

The most important result obtained in this work is the finding that an increase in efficiency of the solar cells with an N-CNT films modified ITO electrode with increased illumination is produced. The IPCE of the bare ITO device shows a maximum (2.1 %) at 3 mW/cm^2 light intensity, which decreased rapidly until a minimum of 1.0 % at maximum light intensity (100 mW/cm^2). A different trend was observed with the N-CNT film modified ITO. The OPV device with a 5 mL N- CNT film on ITO showed an increase in efficiency with light intensity up to a maximum of

1.8 % at a light intensity of 20 mW/cm^2. With an increase in light intensity the IPCE decreased slightly to 1.5 % at the maximum light intensity (100 mW/cm^2). The 10 mL and 15 mL N-CNT films on ITO gave similar trends but the efficiencies were less than for the ITO only device.

Table 7.1 Summary of the device characteristics under 100 mW/cm^2 illumination for various PV devices fabricated in this work.

Device	Voc (V)	Jsc (mA/cm^2)	FF	η(%)
Bare ITO	0.51	3.89	0.51	1.00
5 mL N-CNT on ITO	0.50	4.87	0.52	1.26
10 mL N-CNT on ITO	0.48	2.90	0.38	0.53
15 mL N-CNT on ITO	0.49	2.51	0.43	0.54

7.3. Conclusions

We have observed that ITO electrodes modified with interpenetrating N-CNT films of the appropriate thickness can be used to reduce the efficiency losses that occur in organic solar cells with increase in light intensity. The N-CNTs improve charge collection on the ITO electrode and reduces the voltage drop on the ITO. Metallic N-CNTs were used in this study. P-type B-CNTs could give an even better improvement in J_{sc} and further reduce IPCE losses at high light intensity. These results point to a need to further optimize the N-CNT film thickness and also try other doped carbon nanotubes.

References

1 Hoppe H. and Sariciftci NS. Organic solar cells: An overview. *J. Mater. Res.* 2004; 19(07): 1924-1945.

2 Galagan Y, Manor A, Andriessen R and Katz EA. Analysis of light intensity dependence of organic photovoltaics: Towards efficient large-area solar cells. In *Photovoltaic Specialists Conference (PVSC), 2012 38th IEEE* (pp. 002750-002752). IEEE.

3 Manor A, Katz EA, Tromholt T, Hirsch B and Krebs FC. Origin of size effect on efficiency of organic photovoltaics. *J. App. Phys* 2011;109(7): 074508-074508.

4 Galagan Y, Rubingh JEJM, Andriessen R, Fan CC, Blom PWM, Veenstra SC and Kroon JM. ITO-free flexible organic solar cells with printed current collecting grids. *Sol. Energ. Mater. and Sol. C.* 2011; 95:1339-1343.

5 Berger C, Yi Y, Wang ZL and De Heer, WA. Multiwalled carbon nanotubes are ballistic conductors at room temperature. *App. Phys. A* 2002; 74(3): 363-365.

6 Zhang D, Ryu K, Liu X, Polikarpov E, Ly J, Tompson M E and Zhou C. Transparent, conductive, and flexible carbon nanotube films and their application in organic light-emitting diodes. *Nano Lett* 2006; 6(9): 1880-1886.

7 Rowell MW, Topinka MA, McGehee MD, Prall HJ, Dennler G, Sariciftci NS, et al. Organic solar cells with carbon nanotube network electrodes. *App. Phys. Lett.* 2006; 88(23): 233506-233506.

8 Chaudhary S, Lu H, Müller AM, Bardeen CJ and Ozkan M. Hierarchical placement and associated optoelectronic impact of carbon nanotubes in polymer-fullerene solar cells. *Nano lett.* 2007; 7(7): 1973-1979.

9 Zheng LX, O'connell MJ, Doorn SK, Liao XZ, Zhao YH, Akhadov EA, et al. Ultralong single-wall carbon nanotubes. *Nat. Mater.* 2004; 3(10): 673-676.

10 Li G, Shrotriya V, Yao Y, and Yang Y. Investigation of annealing effects and film thickness dependence of polymer solar cells based on poly (3-hexylthiophene). *J. of App. Phys.* 2005; 98(4): 043704-043704.

11Ulbricht R, Lee SB, Jiang X, Inoue K, Zhang M, Fang S, et al. Transparent carbon nanotube sheets as 3-D charge collectors in organic solar cells. *Sol. Ener. Mater. Sol. C.* 2007; 91(5): 416-419.

12 Wu Z, Chen Z, Du X, Logan JM, Sippel J, Nikolou M. et al. Transparent, conductive carbon nanotube films. *Science* 2004; 305(5688): 1273-1276.

13 Ulbricht R, Lee SB, Jiang X, Inoue K, Zhang M, Fang S, et al. Transparent carbon nanotube sheets as 3-D charge collectors in organic solar cells. *Sol. Ener. Mater. Sol. C.;2007, 91*(5): 416-419.

14 Manor A, Katz EA, Andriessen R and Galagan Y. Study of organic photovoltaics by localized concentrated sunlight: Towards optimization of charge collection in large-area solar cells. *App. Phys. Lett.* 2011; 99(17): 173305-173305.

Chapter 8

N-CNT incorporation in bulk heterojunction P3HT:PCBM Organic Photovoltaics - placement effects

8.1 Introduction

The role of CNTs in organic photovoltaic devices (OPVs) is not yet fully understood. For instance it is thought that they can enhance the charge carrier collection, in a bulk heterojunction solar cell containing a polymer – fullerene active layer, e.g., P3HT: PCBM [1]. However, the efficiencies obtained to date for such types of solar cells remain below that of polymer-fullerene solar cells that have just entered commercial manufacturing [1]. The reasons for the reduction in efficiency when CNTs are incorporated include shorting between electrodes, lack of clarity on the nature of the synthesized CNTs, i.e., whether they are metallic or semiconducting, and whether they are *n*- or *p*- type.

Whilst the diameters of carbon nanotubes range from 1 nm to 100 nm, the length of carbon nanotubes is usually > 200 nm, which is longer than the active layer of the OPVs. It is possible for CNTs to be in contact with both the aluminium electrode and the ITO electrode which leads to short circuits [2,3,4]. A method that can be used to avoid shorting is by incorporating only small amounts of CNTs in the bulk heterojunction active layer. However, the amount of CNTs that can be used might not be sufficient to effect any significant improvement in OPVs [5]. For optimum performance it has been suggested that between 1 and 2% CNT (wt/wt) should be incorporated in the polymer matrix [6]. This is already large enough amount to cause shorting in the solar cell but the effect will be dependent on the length of the CNTs. Shorting could also be avoided by incorporating CNTs at strategic places in the organic solar cell. Figure 8.1 shows the different parts of an OPV device in which CNTs can be placed. Incorporating CNTs on top of the ITO and on top of the

PEDOT:PSS layers has an enhancement effect on the incident photon-to-current efficiency (IPCE) of an OPV device (Figure 8.1, device 2 and 3) [1]. This is because the CNT nanostructures on the electrodes behaves as a 3D electrode and enhances hole collection at the anode. On the other hand addition of a CNT layer on top of the active layer but below the aluminium electrode results in low device IPCE because the work function of the metallic CNT matches that of PEDOT:PSS resulting in a negligible electric field effect (Figure 8.1, device 5). Strong electric field effect is required to drive flow of charged to the different electrodes [7].

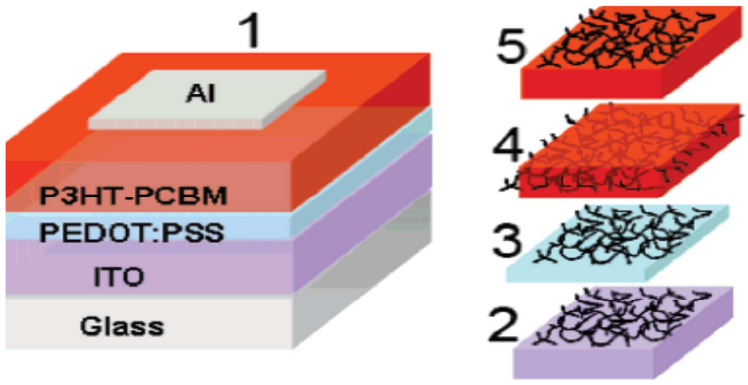

Figure 8.1 OPV showing different layers in which CNT layers could be incorporated.[1]

The incorporation of CNTs in the bulk heterojunction active layer blend (Figure 8.1, device 4) in most cases results in low IPCE in the OPVs [1] Shorting caused by the long CNTs as well as the metallic behavior of CNTs contribute to this. A solution to the shorting problem could be to modify the CNTs from the metallic behavior to become semiconducting. Nitrogen doped carbon nanotubes (N-CNTs) can be made n-type if quaternary type N is incorporated [8]. The use of n-type N-CNTs in the P3HT:PCBM to enhance charge carrier transport to electrodes is likely to produce OPVs with better IPCE. Indeed, N-CNTs have been used as selective transport media in OPVs to transport electrons from the active layer to the aluminium cathode resulting in an enhanced J_{sc} and IPCE [3,6]. However shorting is still possible in these devices since N-CNTs can protrude through the bulk heterojunction active layer to both the aluminium and ITO electrodes. A device fabrication procedure to make

OPVs with configurations which minimize the possibilities of shorting in the P3HT:PCBM:N-CNT bulk heterojunction active layer is required. Herein we report on a procedure involving the spin-coating of two active layers; (P3HT:PCBM spincoated on top of a graphene oxide (GO) hole transport layer followed by a P3HT:PCBM:N-CNT layer) to produce novel solar cell devices. This was done to try and ensure that N-CNTs were only in contact with the Al electrode thus minimizing shorting.

8.2 Experimental

Photovoltaic devices were fabricated on clean patterned ITO coated glass substrates. GO was supplied by GraphenEx. The GO from graphenEx was obtained from purified natural graphite powder (SP-1, Bay Carbon) using the modified Hummers method) [9] Spin-coating was used to deposit the Graphene oxide hole transport layer (GO HTL) on the patterned ITO substrates (2000 rpm for 60 second). Four OPV devices with the following configuration were made in this work (1) ITO/GO/P3HT:PCBM/N-CNT/Al, (2) ITO/GO/P3HT:PCBM:N-CNT/Al, (3) ITO/GO/P3HT:PCBM/P3HT:PCBM:N-CNT/Al and (4) ITO/GO/P3HT:PCBM/Al**.** Three active layer solutions were prepared by stirring the respective mixtures on a magnetic stirrer (500 rpm) for 3 hours; (1) 20 mg/ml of 50:50 (wt:wt) of P3HT and PCBM, (2) 20 mg/mL of 49.5:49.5:1 of P3HT, PCBM and N-CNTs, respectively, and (3) 10 mg/mL of 33:66:1 P3HT, PCBM and N-CNT, respectively. The ITO/GO/P3HT:PCBM/N-CNT/Al device was made by spincoating solution 1 on top of the GO layer at 2000 rpm for 1 minute followed by spin-coating on top of this layer an N-CNT solution. The ITO/GO/P3HT:PCBM:N-CNT/Al device was made by spin-coating solution 2 on top of the GO layer. The ITO/GO/P3HT:PCBM/P3HT:PCBM:N-CNT/Al device was made by spin-coating solution 1 on top of the GO layer followed by spin-coating solution 3. The control ITO/GO/P3HT:PCBM/Al device was made by spin-coating solution 1 on the GO layer. Lastly the Al top electrodes were deposited by thermal evaporation in vacuum. The current – voltage (I-V) characteristics of the devices were obtained under solar simulated AM 1.5 spectrum white light (100 mW/cm^2) at room temperature using an

HP 4141 source measure unit. A Chemat Technology Spin-coater KW-4A spin-coater and a Newport Solar simulator were used. All chemicals were obtained from Sigma Aldrich.

8.3 Results and discussion

Figure 8.2 shows the current density - voltage (J–V) plots of the three devices incorporating N-CNTs in different configurations in the bulk heterojunction OPV and a control device that did not contain N-CNTs.

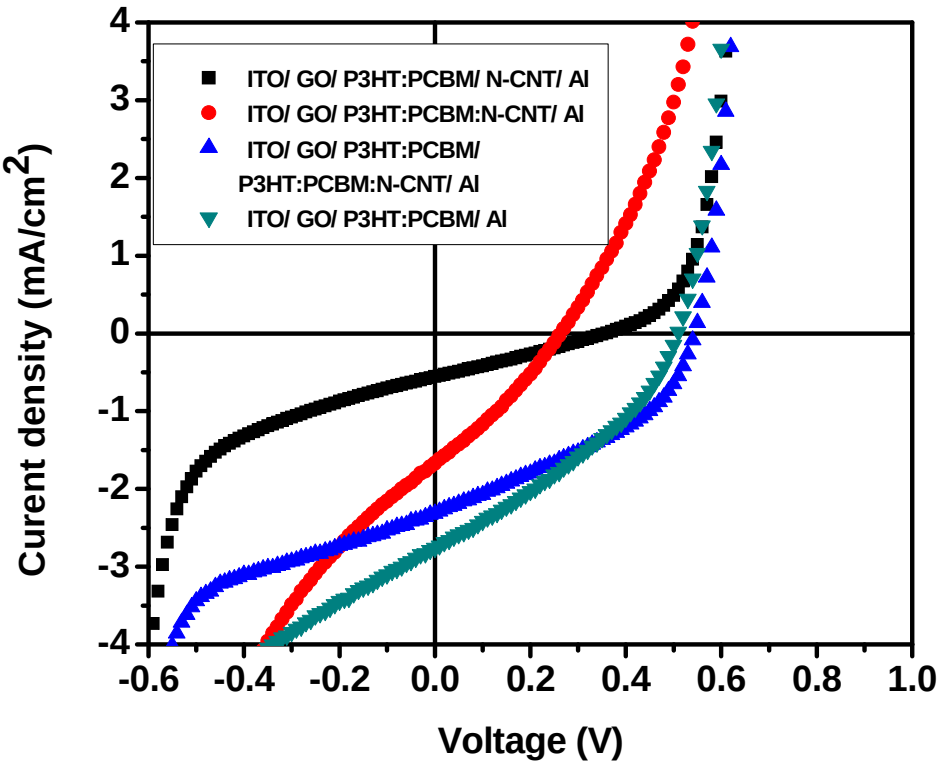

Figure 8.2 Current voltage characteristics of photovoltaic devices with different hole transport layer.

The J – V characteristics do not show the diode behavior that was shown by devices in the previous chapter as expected for such devices. The S shape in the J – V characteristics is related to energy barriers causing a redistribution of the electric field and charge carrier density gradients. The average short circuit current density (J_{sc}),

open-circuit voltage (V_{oc}), fill factor (FF),and PCE values for each device are summarized in Table 8.1. The ITO/ GO/ P3HT:PCBM/ N-CNT/ Al device shows a low V_{oc} of 0.36 V and a J_{sc} of 0.55 mA/cm^2. The N-CNT layer disrupts the electric field effect which is created by the difference in the work function of GO and the work function of Al. As a result the device has a negligible electric field effect which leads to a similar current in forward and reverse bias and a small V_{oc} [10].

Table 8.1 Summary of the photovoltaic parameters of different OPV devices incorporating N-CNT materials in different parts of the active layers.

Device	V_{oc} (V)	J_{sc} mA/cm^2	FF (%)	η (%)
ITO/ GO/ P3HT:PCBM/ N-CNT/ Al	0.36	0.55	26.7	0.05
ITO/ GO/ P3HT:PCBM:N-CNT/ Al	0.27	1.67	29.1	0.13
ITO/ GO/ P3HT:PCBM/ P3HT:PCBM:N-CNT/ Al	0.55	2.31	38.1	0.39
ITO/ GO/ P3HT:PCBM/ Al	0.51	2.76	34.1	0.48

A similar current in the forward and reverse bias results in a small J_{sc}. The device incorporating N-CNTs in the normal bulk heterojunction (ITO/GO/P3HT:PCBM:N-CNT/Al) has poor J-V parameters because the N-CNTs in the active layer leads to short circuiting. The N-CNTs used in this work are long (> 500 nm), it is possible that they can protrude from the active layer and touch both electrodes causing shorts in the device. On the other hand, the device with an active layer containing N-CNTs in the bulk heterojunction close to the Al has the best performance when compared to all the devices containing N-CNTs. However the J_{SC}, FF and IPCE of this device is still lower than the performance of the P3HT:PCBM only device. Only the V_{oc} of the ITO/ GO/ P3HT:PCBM/P3HT:PCBM:N-CNT/Al device was higher than the V_{oc} of the P3HT:PCBM only device. An enhanced V_{oc} in OPV devices incorporating CNTs is attributed to reduced recombination losses [11]. The 1D nature and semiconducting nature of N-CNTs is expected to reduce the recombination pathways for electrons. The ITO/GO/P3HT:PCBM/P3HT:PCBM:N-CNT/Al device demonstrated the

existence of a photocurrent at above the bias of 0.55 V, whereas the control device (ITO/ GO/ P3HT:PCBM/ Al) does not (Figure 8.2). Incorporation of N-CNTs using this procedure is promising and requires further optimization.

In this work we used a procedure to strategically incorporate N-CNTs in a P3HT:PCBM bulk heterojunction in a device configuration which minimizes the possibility of shorting. The active layer was spin-coated twice in the following order; (1) P3HT:PCBM layer deposited from a 20 mg/mL solution of a 50:50 P3HT and PCBM mixture in chloroform and (2) P3HT:PCBM:N-CNT layer deposited from 10 mg/mL solution of a 33:66:1 P3HT, PCBM and N-CNT mixture in chloroform. The concentration differences enabled the final composite film to have a concentration gradient. The concentration of P3HT increased towards the GO layer whilst the PCBM and N-CNT concentration increased towards the Al electrode (Figure 8.3). This configuration if well optimized it should enhance the electric field generated by the opposite GO and Al. This configuration will enhance the J_{sc} in an optimized device leading to better IPCE.

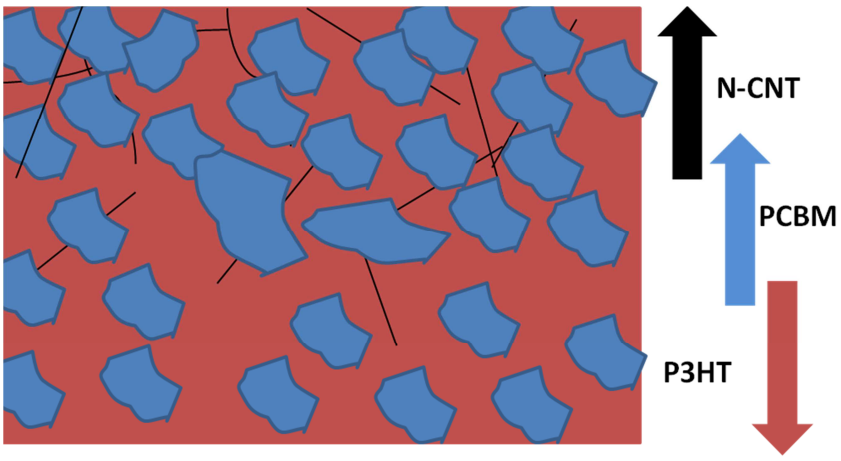

Figure 8.3 Schematic diagram of the bulk heterojunction active layer of the OPV device containing N-CNTs arrows signifying increasing concentration.

8.4 Conclusion

In conclusion, we employed a novel fabrication technique to incorporate N-CNTs into the bulk heterojunction active layer of a P3HT:PCBM OPV device. This technique

results in a configuration with a concentration gradient of P3HT and PCBM:N-CNT from the ITO and Al electrodes respectively. The resulting effect on the J – V parameters is promising and requires further optimization. There is still room for improvement of solar cells incorporating N-CNTs from a materials synthesis as well as from device design and optimization approaches.

References

1 Chen W, Xu T, He F, Wang W, Wang C, Strzalka J, et al. Hierarchical nanomorphologies promote exciton dissociation in polymer/fullerene bulk heterojunction solar cells. *Nano lett.* 2011; 11(9): 3707-3713.

2 Li C, Chen Y, Wang Y, Iqbal Z, Chhowalla M, and Mitra S. A fullerene–single wall carbon nanotube complex for polymer bulk heterojunction photovoltaic cells. *J. Mater. Chem.* 2007; 17(23): 2406-2411.

3 Lu L, Xu T, Chen W, Lee JM, Luo Z, Jung IH, et al. The Role of N-Doped Multiwall Carbon Nanotubes in Achieving Highly Efficient Polymer Bulk Heterojunction Solar Cells. *Nano lett.* 2013; 13(6): 2365-2369.

4 Romero DB, Carrard M, De Heer W and Zuppiroli L. A carbon nanotube/organic semiconducting polymer heterojunction. *Adv. Mater* 1996; 8(11): 899-902.

5 Hatton RA, Miller AJ and Silva SRP. Carbon nanotubes: a multi-functional material for organic optoelectronics. *J. Mater. Chem.* 2008;,18(11): 1183-1192.

6 Lee JM, Park JS, Lee SH, Kim H, Yoo S, and Kim SO. Selective Electron-or Hole-Transport Enhancement in Bulk-Heterojunction Organic Solar Cells with N-or B-Doped Carbon Nanotubes. *Adv. Mater.* 2011;23(5): 629-633.

7 Hoppe H and Sariciftci NS. Organic solar cells: An overview. *J. Mater. Res.* 2004; 19(07): 1924-1945.

8 Krstić V, Rikken GLJA, Bernier P, Roth S and Glerup M. Nitrogen doping of metallic single-walled carbon nanotubes: n-type conduction and dipole scattering. *EPL.* 2007; 77(3): 37001.

9 Hirata M, Gotou T, Horiuchi S, Fujiwara M, and Ohba M. Thin-film particles of graphite oxide 1:: High-yield synthesis and flexibility of the particles. *Carbon* 2004; *42*(14): 2929-2937.

10 Chaudhary S, Lu H, Müller AM, Bardeen CJ and Ozkan M. Hierarchical placement and associated optoelectronic impact of carbon nanotubes in polymer-fullerene solar cells. *Nano lett. 2007; 7*(7): 1973-1979.

11 Wienk MM, Kroon JM, Verhees WJ, Knol J, Hummelen JC, van Hal PA and Janssen RA. Efficient methano [70] fullerene/MDMO-PPV bulk heterojunction photovoltaic cells. *Angew Chemie*, 2003, 115(29), 3493-3497.

Chapter 9

BN doped graphene as a hole transport layer in P3HT:PCBM bulk-heterojunction organic photovoltaic devices

9.1 Introduction

One problem affecting the poor performance of bulk-heterojunction (BHJ) organic photovoltaic devices (OPVs) is recombination of charge carriers before they reach the electrodes for collection. In a BHJ OPV, both the donor and acceptor are in contact with both the anode and the cathode and this increases the recombination rate. To reduce the detrimental effect of this, electron blocking layers are usually deposited on top of the transparent ITO electrode to block electrons from reaching this electrode. Thus p-type, wide band gap, inorganic materials such as V_2O_5 and MoO_3 are vacuum deposited on the ITO electrode to act as electron blocking layers [1]. In order to reduce the cost of OPVs, low cost coating deposition methods are needed. As such, PEDOT:PSS is a popular hole transport material mostly used in OPVs [2]. This is because the material is water based and can easily be deposited on an electrode by spin-coating. One disadvantage of using PEDOT:PSS is that it is deposited from an acidic solution which leads to etching of the ITO electrode [3]. Etching of the ITO electrode makes it very resistive which affects current collection. Further, the etched indium can diffuse into the OPV active layer which has a degrading effect on the solar cell [4]. Solution processable graphene oxide (GO) has recently been used as a hole transport layer in OPVs and it has been shown to give comparable results to PEDOT:PSS [5]. However, device performance is very sensitive to thickness and uniformity of the graphene oxide films. Graphene oxide is obtained in a solution form. The GO concentration can be varied and is dependent on how it is made. This variable concentration affects the thickness of the deposited layers which is deposited

using either the vacuum filtration or spin-coating method. On the other hand, chemical vapor deposition produced graphene can be made with a large area and a controllable thickness (number of layers) [6]. However graphene is a purely metallic material so it is not useful as a hole transport layer [7]. Doping of graphene with heteroatoms like B and N is known to making the graphene p-type or n-type respectively [8]. Incorporation of BN in graphene is another way of opening a band gap in graphene and making it a p-type semiconductor [9]. Recently we made a BN doped graphene with 98% carbon and 2% BN (at. %). Since BN induces p-type behavior in graphene, we have used this material as a HTL in OPVs. An initial study investigated the incorporation of BN in large area CVD grown graphene and determined its applicability as a HTL in OPVs.

In the second part of this work we studied the use of BN doped graphene in an inverted OPV. In an inverted OPV the ITO collects electrons and the metal contact collects holes [10]. This is different from a normal OPV where the ITO collects holes and the metal collects electrons. In most cases a high band gap material such as ZnO is deposited on the ITO electrode for efficient electron collection [11]. Advantages of this orientation of an OPV are that it allows the use of air stable metals like copper and gold with high work functions to be used [10]. Also, non vacuum coating techniques for the metal top electrodes are made possible, this is important because it reduces the cost of device fabrication [12]. Oxygen and moisture attack on the polymer can be minimized if a graphene based material is made the HTL in an inverted device because graphene if impermeable to air and moisture [13,14]. The BN doped graphene will then act as a HTL and simultaneously as a gas barrier material. The use of the BN doped graphene as a HTL will also avoid the use of PEDOT:PSS and minimizes corrosion of the ITO electrode.

9.2 Experimental

9.2.1 Graphene synthesis

Graphene and BN doped graphene were synthesized using the CVD method described earlier in chapter 5 and chapter 6. Graphene Oxide (GO) was supplied by

GraphenEx. The GO from GraphenEx was obtained from purified natural graphite powder (SP-1, Bay Carbon) using the modified Hummers method) [15].

9.2.2 Device fabrication

Photovoltaic devices were fabricated on clean patterned ITO coated glass substrates. Graphene was transferred to a patterned ITO glass using the method described earlier (chapter 5 and 6). Spin-coating was used to deposit GO on the patterned ITO substrates. Six OPV devices with the following configuration were made in this work (1) ITO/P3HT:PCBM/Al, (2) ITO/PEDOT:PSS/P3HT:PCBM/Al, (3) ITO/GO/P3HT:PCBM/Al, (4) ITO/Graphene/P3HT:PCBM/Al, (5) ITO/BN graphene/P3HT:PCBM/Al and (6) ITO/P3HT:PCBM/BN graphene/Al. A 20 mg/ml active layer solution was prepared by dissolving P3HT and PCBM in chloroform followed by stirring for 3 hours. The solution was spincoated on the five prepared HTL electrodes at 2000 rpm for 1 minute. The Al top electrodes were deposited by thermal evaporation in vacuum. I-V characteristics were obtained under solar simulated AM 1.5 spectrum white light (100 mW/cm^2) at room temperature using an HP 4141 source measure unit. A Chemat Technology Spin-coater KW-4A spin-coater and a Newport Solar simulator were used. All chemicals were obtained from Sigma Aldrich.

9.3 Results and discussion

Figure 9.1a shows the current voltage plots of the devices containing different hole transport layers. The average short circuit current density (J_{sc}), open-circuit voltage (V_{oc}), fill factor (FF), and power conversion efficiency values for each device are summarized in Table 1. The ITO only device exhibits a poor performance shown by an IPCE of 0.04%. The addition of a graphene film between ITO and the active layer resulted in a substantial increase in J_{sc}, V_{oc} and FF leading to an increase in the PCE to 0.11 % from (0.04 %). At ambient conditions due to the presence of oxygen, graphene is p-type doped which explains why it works as an HTL in the OPV devices [7].

The use of BN doped graphene further improves the Jsc, Voc and FF which also results in a substantial increase of PCE to 0.37 %. This is a threefold increase in PCE when BN doped graphene in used instead of pristine graphene. BN doped graphene is a hybrid material containing sp^2 carbons and small sp^2 domains of hexagonal BN. Hexagonal boron nitride (h-BN) is an insulating material made from hexagonal rings of B and N as in graphene, with a work function of approximately 6 eV and a band gap close to 4.8 eV [16]. On the other hand graphene is a semi metal without a zero band gap and a work function of approximately 4.6 eV [17]. A mixture of the two materials has semiconducting properties and a useful band gap of around 3 eV can be obtained.

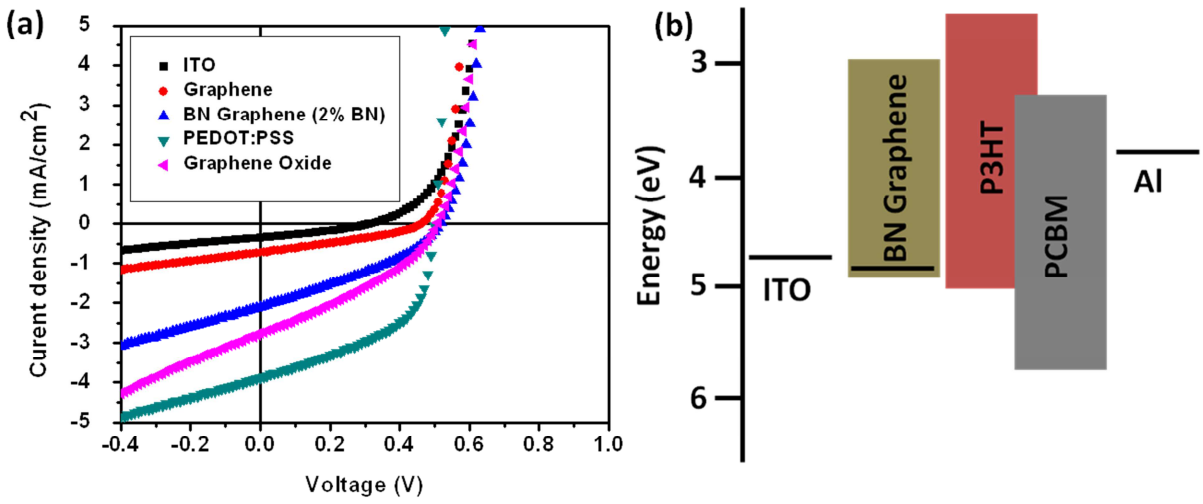

Figure 9.1 (a) Current_voltage characteristics of photovoltaic devices with different hole transport layer (b) Energy level diagrams of the bottom electrode ITO, interlayer material (BN doped graphene), P3HT (donor), and PCBM (acceptor), and the top electrode Al.

The resulting band gap is sensitive to the amount of the carbon and BN species in the hybrid material [18]. The graphene material used in this work contains approximately 4% BN. From our earlier work in chapter 6 we saw that incorporating more than 2% BN resulted in an increase in the O content of the graphene [19]. Incorporation of O is ideal for a graphene material for use as an HTL because it further dopes the graphene p-type and increase the band gap as in the case of GO. Raman and XPS

evidence reported in chapter 6 showed that the graphene material changed from a semi metal to a p-type semiconducting material after doping. Doping of graphene with BN is likely to increase the work function of the graphene to approximately 4.8 eV, which matches well the LUMO of P3HT and the workfunction of ITO to work as an HTL. The PCE of the BN doped graphene HTL device still falls below that of the devices with a GO HTL (0.48 %). Our BN doped graphene contains a small amount of BN (4%). This means that only a small band gap was opened and the material is only slightly p-type modified. For an effective HTL based on this material, a BN doped graphene material containing up to 50 % BN could be ideal. Increasing the amount of BN in graphene will result in non-conductive BN domains together with conducting graphene domains, resulting in a larger band gap. Indeed the synthesis of atomic layers of hybridized boron nitride and graphene domains has been reported elsewhere [20]. Use of BN doped graphene with a high BN content is expected to match or be better than that of a graphene oxide hole transport layer.

Table 9.1 Summary of Typical Photovoltaic Parameters of the different OPVs containing different HTL materials.

Device	V_{oc} (V)	J_{sc} mA/cm^2	FF (%)	η (%)
ITO	0.32	0.35	31.7	0.04
PEDOT:PSS	0.51	3.89	50.6	1.00
Graphene oxide	0.51	2.76	34.1	0.48
Graphene	0.47	0.73	31.9	0.11
BN Graphene	0.51	2.1	33.9	0.37

The performance of a solar cell is sensitive to the thickness of graphene oxide HTL films [5]. The use of graphene oxide requires careful optimization to be consistently deposited as a continuous monolayer graphene film on a substrate. On the other hand graphene obtained from a CVD technique is usually generates a uniform monolayer and large area material [6]. The use of a graphene as an HTL will remove the need to use PEDOT:PSS. The resulting devices will be more stable in ambient conditions because graphene is neutral and does not corrode the ITO electrode as in the case when the acidic PEDOT:PSS is used.

Figure 9.2a shows the structure of an inverted OPV with ITO/P3HT:PCBM/BN graphene/Al configuration. The band energy diagram of such an inverted device is shown in Figure 9.2b. An electron collecting layer is required in this device to allow only electrons to be collected at the ITO because since both electrons and holes can be collected at the ITO. An electron collecting layer was not used in this work because it should be noted that the purpose of these experiments was not to compare efficiency between normal OPVs and inverted OPVs but to show that inverted OPVs are more air stable when compared to the normal OPV devices. The graphene HTL in an inverted OPV should act as a protective layer which stops oxygen and moisture from attacking the P3HT material.

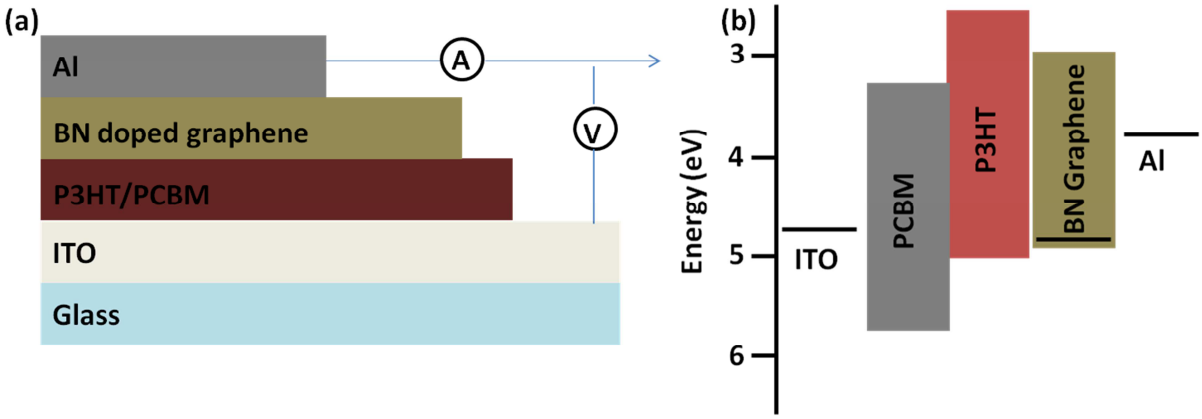

Figure 9.2 (a) Schematic of the inverted photovoltaic device structure consisting of the following: ITO/ P3HT:PCBM/ BN doped graphene/ Al. (b) Energy level diagram of the bottom electrode ITO, PCBM (acceptor) and P3HT (donor), BN doped graphene (HTL) and the top electrode Al.

Figure 9.3a shows the current voltage plots of the normal OPV device with a BN doped graphene HTL and an inverted OPV with a BN doped graphene HTL. The average short circuit current density (J_{sc}) and open-circuit voltage (V_{oc}) of each set of device on day one and after 14 days are summarized in Table 9.2. The normal OPV device performs three times better than the inverted OPV device (Figure 9.2a and table 9.2) on day 1. The poor performance of the inverted device relates to the absence of a required electron transport layer. The devices were left in air for 14 days

and J-V measurements were recorded for the same devices. After 14 days the normal device gave a J_{sc} of 0.015 mA/cm^2 whilst the inverted device gave a J_{sc} of 0.169 mA/cm^2. The inverted device was now giving a better output as compared to the normal device. This means the inverted device is more stable in air compared to the normal devices. Graphene is a completely impermeable material; even helium cannot permeate through graphene [13]. This means that the inverted device is protected from oxygen and moisture which are the main causes of degradation.

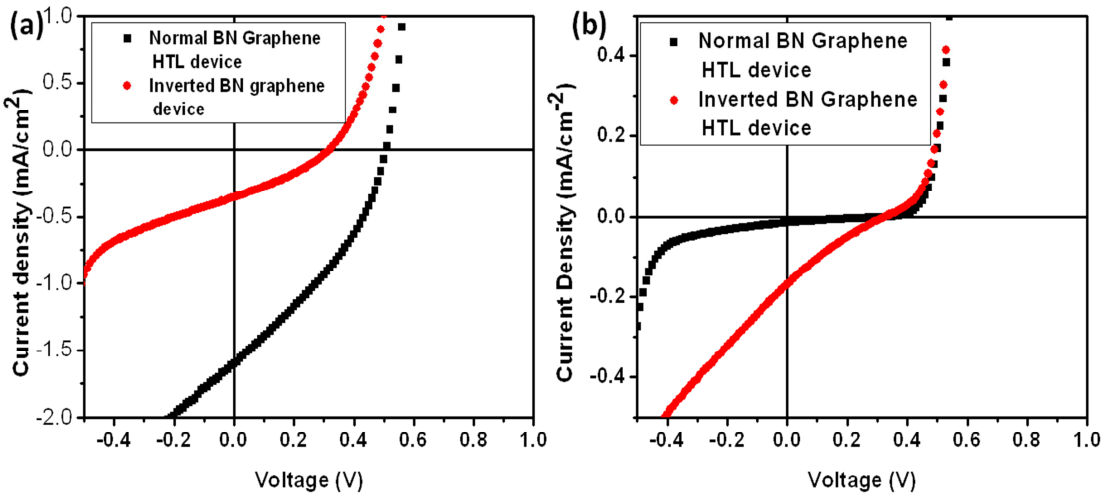

Figure 9.3 (a) Current voltage characteristics of photovoltaic devices of the normal and inverted devices measured after fabrication at day 1, and (b) Current voltage characteristics of photovoltaic devices of the normal and inverted devices measured after 14 days in air.

Also it protects the active layer against the aluminium top electrode which is known to diffuse into the active layer and degrade the solar cell [4]. The graphene layer avoids any diffusion of aluminium in the active layer thus making it stable for a longer time. Graphene based HTL in inverted OPVs offers a great potential for a completely non vacuum OPV device fabrication which are air stable devices without the need for encapsulation.

Table 9.2 Summary of Typical Photovoltaic Parameters of the normal and inverted OPV containing a BN doped graphene HTL measured on different days.

Device	Day 1		After 14 days	
	V_{oc} (V)	J_{sc} (mA/cm^2)	V_{oc} (V)	J_{sc} (mA/cm^2)
Normal	**0.51**	**1.6**	**0.35**	**0.0015**
Inverted	**0.30**	**0.35**	**0.31**	**0.169**

9.4 Conclusion

In summary large area BN doped graphene has been used as a hole transport layer in OPVs. An attempt to use BN doped graphene as a HTL and encapsulating material for package free OPVs in inverted OPVs showed that inverted devices are less efficient but more air stable when compared to the normal devices. There is room for optimizing the devices by increasing doping levels and interface engineering on the ITO electrode in the inverted device to match it with the HOMO of the PCBM.

References

1 Shrotriya V, Li G, Yao Y, Chu CW and Yang Y. Transition metal oxides as the buffer layer for polymer photovoltaic cells. *App. Phys. Lett. 2006*; *88*(7): 073508-073508.

2 Gunes S, Neugebauer H and Sariciftci NS. Conjugated polymer-based organic solar cells. *Chem. Rev.* 2007; 107(4): 1324-1338.

3 Kim YH, Lee SH, Noh J and Han SH. Performance and stability of electroluminescent device with self-assembled layers of poly (3, 4-ethylenedioxythiophene)–poly (styrenesulfonate) and polyelectrolytes. *Thin Solid Films* 2006; 510(1): 305-310.

4 Jørgensen M, Norrman K and Krebs FC. Stability/degradation of polymer solar cells. *Sol. Energ. Mater. Sol. C.* 2008; 92(7): 686-714.

5 Li SS, Tu KH, Lin CC, Chen CW and Chhowalla M. Solution-processable graphene oxide as an efficient hole transport layer in polymer solar cells. *ACS nano* 2010; 4(6): 3169-3174.

6 Mattevi C, Kim H and Chhowalla M. A review of chemical vapor deposition of graphene on copper. *J. Mater. Chem.* 2011; 21(10): 3324-3334.

7 Ryu S, Liu L, Berciaud S, Yu YJ, Liu H, Kim P. et al. Atmospheric oxygen binding and hole doping in deformed graphene on a SiO2 substrate. *Nano lett.* 2010; 10(12): 4944-4951.

8 Panchakarla LS, Subrahmanyam KS, Saha SK, Govindaraj A, Krishnamurthy HR, Waghmare UVand Rao CNR. Synthesis, structure, and properties of boron-and nitrogen-doped graphene. *Adv. Mater* 2009; 21(46): 4726-4730.

9 Shinde PP and Kumar V. Direct band gap opening in graphene by BN doping: Ab initio calculations. *Phys Rev. B* 2011; 84(12): 125401.

10 Khatri I, Bao J, Kishi N and Soga T. Similar Device Architectures for Inverted Organic Solar Cell and Laminated Solid-State Dye-Sensitized Solar Cells. *ISRN Electronics, 2012*.

11 White MS, Olson DC, Shaheen SE, Kopidakis N and Ginley DS. Inverted bulk-heterojunction organic photovoltaic device using a solution-derived ZnO underlayer. *App. Phys. Lett.* 2006, 89(14), 143517-143517.

12 Krebs FC. Air stable polymer photovoltaics based on a process free from vacuum steps and fullerenes. *Sol. Energ. Mater. Sol. C.* 2008; 92(7): 715-726.

13 Novoselov KS, Fal VI, Colombo L, Gellert PR, Schwab MG and Kim KA. Roadmap for graphene. *Nature* 2012; 490(7419): 192-200.

14 Chen S, Brown L, Levendorf M, Cai W, Ju SY, Edgeworth J, et al. Oxidation resistance of graphene-coated Cu and Cu/Ni alloy. *Acs Nano* 2011; 5(2): 1321-1327.

15 Hirata M, Gotou T, Horiuchi S, Fujiwara M and Ohba M. Thin-film particles of graphite oxide 1: High-yield synthesis and flexibility of the particles. *Carbon* 2004; *42*(14): 2929-2937.

16 Czerw R, Webster S, Carroll DL, Vieira SMC, Birkett PR, Rego CA and Roth S. Tunneling microscopy and spectroscopy of multiwalled boron nitride nanotubes. *App. phys lett* 2003; 83(8): 1617-1619.

17 Yu YJ, Zhao Y, Ryu S, Brus LE, Kim KS and Kim P. Tuning the graphene work function by electric field effect. *Nano lett.* 2007; 9(10): 3430-3434.

18 Wei X, Wang MS, BandoY and Golberg D. Electron-beam-induced substitutional carbon doping of boron nitride nanosheets, nanoribbons, and nanotubes. *ACS nano* 2011; 5(4): 2916-2922.

19 Bepete G, Voiry DA, Chhowalla M, Chiguvare Z and Coville N J. Incorporation of small BN domains in graphene during CVD using methane, boric acid and nitrogen gas. *Nanoscale* 2013; 5: 6552-6557.

20 Ci L, Song L, Jin C, Jariwala D, Wu D, LiY, et al. Atomic layers of hybridized boron nitride and graphene domains. *Nat. Mater* 2010; 9(5): 430-435.

Chapter 10

Conclusions and Recommendations

10.1 Conclusions

10.1.1 Synthesis of carbon nanomaterials

- 1D carbon nanomaterials and 2D carbon nanomaterials can be synthesized using the chemical vapor deposition method. The nature of the catalyst used determines the dimensions of the nanomaterials produced. In this study supported iron nanoparticles were used to grow N-CNTs whilst a copper foil was used to grow graphene. The ID carbon nanotubes can also be made into a 2D film using the vacuum filtration and stamping method.

10.1.1.1 Nitrogen doped carbon nanotubes

- CVD synthesis temperature and precursor materials containing different concentration of O can be used to control the amount and type of N which can be incorporated in an N-CNT material. However, changes in the morphology and graphitic structure of the N-CNT materials were noted.
- Heat treatment of already synthesized N-CNTs at temperatures above 400 ^{o}C but below 1000 ^{o}C changed the amount and type of N that is incorporated in the N-CNT material. This method of changing the amount and type of N in N-CNTs does not affect the morphology of the material.

10.1.1.2 Graphene

- LPCVD synthesis of graphene on a copper catalyst is indeed a self limiting process using carefully controlled methane concentrations/flow rates but at very low methane concentrations/flow rates multilayer graphene can be formed if extended growth times are used.

- Small BN domains can be incorporated in graphene during CVD using boric acid, methane and nitrogen gas. The N of the BN is bonded to carbon forming B-N-C systems, showing that continuous BN containing graphene in which BN species were incorporated in the graphene structure was grown.

10.1.2 Organic photovoltaic devices

10.1.2.1 N-CNT modified electrode

- We have shown that ITO electrodes modified with interpenetrating N-CNT films of the appropriate thickness can be used to reduce the efficiency loses that occur in organic solar cells with increase in light intensity. This remarkable finding is a result of improved charge collection in the OPV at the ITO electrode.

10.1.2.2 N-CNT in bulk heterojunction layer

- Incorporating N-CNTs in the bulk heterojunction layer results in poor J_{sc} and V_{oc} because of short circuiting. A method to minimize shorting by spin-coating a second active layer containing N-CNTs produced an OPV device giving a better Jsc. However, the J_{SC} was still lower than that of the device which did not contain carbon nanotubes. The V_{OC} of this device was higher than the one which did not contain carbon nanotubes. This is a promising result and if carefully optimized this type of device configuration can give a better power conversion performance.

10.1.2.3 BN doped graphene hole transport layer

- BN doped graphene showed potential for use as a hole transport layer. However the performance of the device containing BN doped graphene as an HTL was poor when compared to the device with PEDOT:PSS or GO hole transport layers. When used in an inverted solar cell, very poor output was achieved but the device remains stable in air for longer times than the normal device.

10.2 Recommendations

10.2.1 Nitrogen doped carbon nanotubes

- The use of other O containing precursors with different structures like ketones, aldehydes, amides could be used in CVD synthesis to make N-CNTs to establish whether they have the same effect on the amount and type of nitrogen incorporated in N-CNTs. A way of changing the type and amount of N during synthesis without changing the morphology of the resulting N-CNTs is an important study. This could be achieved by introducing O from non carbon containing sources in the form of O_2 or H_2O during the CVD synthesis.

10.2.2 N-CNT modified electrode

- Carbon nanotube doped p-type materials could be used to modify the ITO electrode. This could lead to an even better charge collection by the modified electrode. The thickness of the carbon nanotube film of the ITO should be optimized.

10.2.3 BN doped graphene

- Electrical characterization can be used to study the transfer characteristics of the BN doped graphene to evaluate how much of the band gap is opened. The BN doping level in graphene can be varied and corresponding increase in the band gap could be studied using electrical characterization techniques. This information could be used to select the best BN doped graphene material to be used as a hole transport layer in OPVs.